

DISSERTATION

**TROPICAL CYCLONE EVOLUTION VIA INTERNAL
ASYMMETRIC DYNAMICS**

Submitted by

Eric A. Hendricks

Department of Atmospheric Science

In partial fulfillment of the requirements

for the Degree of Doctor of Philosophy

Colorado State University

Fort Collins, Colorado

Summer 2008

UMI Number: 3332704

INFORMATION TO USERS

The quality of this reproduction is dependent upon the quality of the copy submitted. Broken or indistinct print, colored or poor quality illustrations and photographs, print bleed-through, substandard margins, and improper alignment can adversely affect reproduction.

In the unlikely event that the author did not send a complete manuscript and there are missing pages, these will be noted. Also, if unauthorized copyright material had to be removed, a note will indicate the deletion.

UMI[®]

UMI Microform 3332704

Copyright 2008 by ProQuest LLC.

All rights reserved. This microform edition is protected against unauthorized copying under Title 17, United States Code.

ProQuest LLC
789 E. Eisenhower Parkway
PO Box 1346
Ann Arbor, MI 48106-1346

COLORADO STATE UNIVERSITY

July 9, 2008

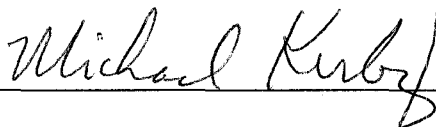
WE HEREBY RECOMMEND THAT THE DISSERTATION PREPARED UNDER OUR SUPERVISION BY ERIC A. HENDRICKS ENTITLED TROPICAL CYCLONE EVOLUTION VIA INTERNAL ASYMMETRIC DYNAMICS BE ACCEPTED AS FULFILLING IN PART REQUIREMENTS FOR THE DEGREE OF DOCTOR OF PHILOSOPHY.

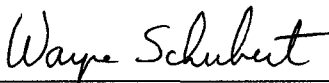
Committee on Graduate Work











Advisor



Department Head

ABSTRACT OF DISSERTATION

TROPICAL CYCLONE EVOLUTION VIA INTERNAL ASYMMETRIC DYNAMICS

This dissertation advances our understanding by which tropical cyclones (TCs) evolve solely due to internal dynamics, in the absence of large-scale environmental factors and surface fluxes, using a hierarchy of numerical model simulations, diagnostics and observations. In the first part, the role of inner-core (eye and eyewall) transport and mixing processes in TC structure and evolution is examined, and in the second part, some asymmetric dynamics of tropical cyclone evolution are studied: spontaneous inertia-gravity wave radiation from active TC cores and an observational case study of the role of vortical hot towers in tropical transition. Overall, internal dynamics are found to be significant for short term intensity change in hurricanes.

The role of two-dimensional transport and mixing in TC structure and intensity change is quantified. First, the mixing properties of idealized hurricane-like vortices are assessed using the effective diffusivity diagnostic. Both monotonic and dynamically unstable vortices are considered. For generic deformations to monotonic vortices, axisymmetrization induces potential vorticity (PV) wave breaking outside the radius of maximum wind, forming a finite radial length surf zone characterized by chaotic mixing. Although on a much smaller scale, this surf zone is analogous to the surf zone outside the wintertime stratospheric polar vortex. For unstable rings, during barotropic instability both the inner and outer breaking PV waves create horizontal mixing regions. For thin ring breakdowns, the entire inner-core becomes a strong mixing region and passive tracers can be transported quickly over large horizontal distances. For thick ring breakdowns, an asymmetric partial barrier region may remain intact at the hurricane tangential jet, with mixing regions on

each side where the waves break. The inner, breaking PV wave is quite effective at mixing passive tracers between the eye and eyewall; with a monotonic low-level equivalent potential temperature radial profile, these results support the hurricane super-intensity mechanism. Next, a systematic study of inner-core PV mixing resulting from unstable vortex breakdowns is conducted. After verifying linear theory, the instabilities are followed into their nonlinear regime and the resultant end states are assessed for 170 different PV rings, covering a wide spectrum of real hurricanes. It is found that during all PV mixing events, both the maximum mean tangential velocity and minimum central pressure simultaneously decrease, thus empirical pressure-wind relationships are likely not valid during these events. Based on these results, the use of a maximum sustained tangential velocity metric in defining hurricane intensity is discouraged. Rather, minimum central pressure or integrated kinetic energy is recommended.

In order to examine transport and mixing in three dimensions, two idealized hydrostatic primitive equation models were developed from a preexisting limited area, periodic spectral shallow water model. The first model uses an isentropic vertical coordinate and the second model uses a sigma (terrain following) vertical coordinate. The models were extended on a Charney-Phillips grid. They include both horizontal momentum and vorticity-divergence prognostic formulations, and a nonlinear balance initialization option. A simulation of a dynamically unstable hurricane-like PV hollow tower in the isentropic model yielded a “PV bridge” across the eye, which has been previously simulated in moist full-physics models. Since a portion of PV is static stability, it is possible that the hurricane eye inversion is dynamically controlled. In addition, an initially vertically erect PV hollow tower became tilted, suggesting one mechanism for creating eyewall tilt is adiabatic PV mixing.

Finally, some asymmetric dynamics of tropical cyclone evolution are examined. First, a shallow water simulation of a non-axisymmetrizing active TC core is analyzed. The

initially balanced flow rapidly evolves into an unbalanced state, and packets of spiral inertia-gravity waves (IGWs) are emitted to the environment. The conditions that favor radiation of IGWs are assessed. Since low wavenumber vorticity structures are often observed in TC cores, it is possible that hurricanes often enter into spontaneously radiative states (notwithstanding the IGWs created by latent heat release from moist convection), affecting their own intensity and disrupting the local environment. Secondly, an observational case study of vortical hot towers (VHTs) in tropical cyclone Gustav (2002) is presented. Multiple mesovortices were observed as low level cloud swirls after being decoupled from the VHTs due to vertical shear. The observed evolution of these mesovortices is consistent with recent full-physics numerical model simulations linking VHTs as fundamental coherent structures of TC genesis and intensification.

Eric A. Hendricks
Department of Atmospheric Science
Colorado State University
Fort Collins, Colorado 80523-1371
Summer 2008

ACKNOWLEDGEMENTS

First and foremost, I am grateful to my advisor, Dr. Wayne Schubert for his advice, support, and unique ability to explain the dynamics of complex atmospheric processes in simple terms. I would like to thank my committee members, Dr. Richard Johnson, Dr. Roger Pielke, Sr., Dr. Christopher Davis, and Dr. Michael Kirby, for serving and for their helpful comments during this research. Additionally, I would like to thank Dr. Michael Montgomery for his advisement and support in a portion of this dissertation.

Numerous people have provided comments and assistance in this research. I thank the Schubert research group staff for their comments and assistance: Mr. Brian McNoldy, Mr. Paul Cielsielski, Mr. Richard Taft, and Mrs. Gail Cordova. I am particularly grateful to Mr. Richard Taft for providing computer and programming assistance over the course of this research. I also thank the Schubert research group graduate students, in particular, Mr. Jonathan Vigh, Mrs. Kate Musgrave and Mr. Kevin Mallen for numerous invigorating discussions on hurricane dynamics. I am grateful to Dr. Scott Fulton for providing a beautiful spectral shallow water model which was used extensively in chapters 4 and 5.

I would like to thank the following people for their helpful comments leading to improvements in papers in this dissertation: Dr. Christopher Rozoff, Dr. Wesley Terwey, Dr. Matthew Eastin, Dr. Emily Shuckburgh, Mr. Blake Rutherford, Dr. Gerhard Dangelmayer, Mr. Arthur Jamshidi, Dr. John Persing, Dr. Celal Konor, Dr. John Knaff, Dr. James Kossin, and Dr. Huiqun Wang. I also acknowledge Drs. Mark DeMaria and Ray Zehr for providing rapid-scan visible satellite imagery of Tropical Storm Gustav (2002), used in the

analysis in chapter 6.

Finally, I would like to thank my family and friends for their support. This research was supported by NSF CMG Grant ATM-0530884, NASA/TCSP Grant 04-0007-0031, and Colorado State University.

DEDICATION

In memory of the victims of Hurricane Mitch (1998) and Cyclone Nargis (2008).

CONTENTS

1 Introduction	1
2 Barotropic Aspects of Transport and Mixing in Hurricanes	3
2.1 Abstract	3
2.2 Introduction	4
2.3 Dynamical model and passive tracer equation	8
2.4 Area coordinate transformation and effective diffusivity	9
2.5 Pseudospectral model experiments and results	13
2.5.1 Elliptical vorticity field	14
2.5.2 Binary vortex interaction	16
2.5.3 Rankine vortex in a turbulent vorticity field	20
2.5.4 Unstable vorticity rings	21
2.6 Sensitivity tests	28
2.6.1 Tracer diffusion coefficient	28
2.6.2 Initial tracer distribution	30
2.6.3 Number of area points	31
2.7 Conclusions	32
3 Lifecycles of Hurricane-like Potential Vorticity Rings	36
3.1 Abstract	36
3.2 Introduction	37
3.3 Review of linear stability analysis	40
3.4 Pseudospectral model experiments	43
3.5 Comparison of numerical model results to linear theory	47
3.6 End states after nonlinear mixing	51
3.7 PV mixing and hurricane intensity change	56
3.8 Summary	61
4 Idealized Mesoscale Models for Studying Tropical Cyclone Dynamics	64
4.1 Introduction	64
4.2 Governing Equations	66
4.2.1 Isentropic vertical coordinate	66
4.2.2 Sigma vertical coordinate	67
4.3 Horizontal Discretization	68
4.4 Temporal discretization	69

4.5	Vertical Discretization	70
4.5.1	Isentropic vertical coordinate	70
4.5.2	Sigma vertical coordinate	73
4.6	Additional Features of the Models	76
4.6.1	Mass restoration	76
4.6.2	Damping	76
4.6.3	Surface friction	77
4.7	Initialization	77
4.7.1	Isentropic vertical coordinate model	77
4.7.2	Sigma vertical voordinate model	79
4.8	Evaluation Tests: Isentropic Vertical Coordinate Model	80
4.8.1	Initialization: comparison to analytic solution	80
4.8.2	Gradient adjustment of an axisymmetric vortex	82
4.8.3	Unstable baroclinic vortex evolution	83
4.8.4	Integral quantities conservation	90
4.9	Conclusions	92
5	Shallow Water Simulation of a Spontaneously Radiating Hurricane-Like Vortex	95
5.1	Introduction	95
5.2	Linearized Shallow Water Equations	97
5.3	Numerical Simulation	99
5.4	Discussion of results	105
5.5	Conclusions	114
6	Rapid-scan Views of Convectively Generated Mesovortices in Sheared Tropical Cyclone Gustav (2002)	116
6.1	Abstract	116
6.2	Introduction	117
6.3	Synoptic History: September 8-12, 2002	118
6.4	Data and analysis procedures	119
6.5	Synoptic-scale analysis	120
6.5.1	Thickness, vertical wind shear and moisture advection	120
6.5.2	Sea surface temperature	120
6.5.3	Near-surface winds and vorticity derived from QuikSCAT	123
6.5.4	Discussion	125
6.6	Mesoscale analysis	126
6.6.1	Observed convection	126
6.6.2	Structure and evolution of mesovortices	126
6.6.3	Partial evidence of system-scale axisymmetrization	129
6.7	Summary	130
7	Conclusions	134

FIGURES

2.1	Visible satellite image of Hurricane Isabel at 1315 UTC on 12 September 2003 (from Kossin and Schubert 2004).	5
2.2	Diagram of the area coordinate. Two hypothetical contours C of the tracer field $c(x, y, t)$ are shown with corresponding area above the contours $A(C, t)$. The other parameters used in the derivation are illustrated as well.	10
2.3	The relative vorticity and effective diffusivity κ_{eff} for the evolution of the elliptical vorticity field at $t = 1.5$ h.	15
2.4	Hovmöller plots of the equivalent length $L_e(r_e, t)$ (left panel) and dimensionless equivalent length $\Lambda_e(r_e, t)$ (right panel) for the evolution of the elliptical vorticity field. Two consistent regions are evident throughout the simulation: the <i>main vortex</i> partial barrier and the <i>surf zone</i> chaotic mixing region. . .	16
2.5	The initial vorticity field (top panel) and side-by-side panels (at 4 h and 24 h) of relative vorticity and effective diffusivity for the binary vortex interaction. The model domain is 600 km by 600 km, but only the inner 200 km by 200 km is shown.	18
2.6	Hovmöller plots of $\kappa_{\text{eff}}(r_e, t)$ (left panel) and $\Lambda_e(r_e, t)$ (right panel) for the binary vortex interaction.	19
2.7	Hovmöller plots of the numerical solution (left) and the analytic solution (equation (19); right) of the tracer concentration $C(r_e, t)$ for the binary vortex interaction. The analytic solution is obtained with $\kappa_{\text{eff}} = \kappa = 2500 \text{ m}^2 \text{ s}^{-1}$	20
2.8	The initial vorticity field (top panel) and side-by-side panels (at 9.5 h and 40 h) of relative vorticity and effective diffusivity for the Rankine-like vortex in a turbulent vorticity field. The model domain is 600 km by 600 km, but only the inner 200 km by 200 km is shown.	22
2.9	The initial vorticity field (top panel) and side-by-side panels (at 13 h and 41 h) of relative vorticity and effective diffusivity κ_{eff} for a prototypical thick, filled unstable vorticity ring (Experiment A of Table 1).	25
2.10	The initial vorticity field (top panel) and side-by-side panels (at 6 h and 20 h) of relative vorticity and effective diffusivity κ_{eff} for a prototypical thin, hollow unstable vorticity ring (Experiment D of Table 1).	26
2.11	Hovmöller plots depicting the temporal evolution of $\kappa_{\text{eff}}(r_e, t)$ for the A ring (left) and the D ring (right).	27
2.12	Time-averaged (0-48 h) effective diffusivity for all unstable rings versus equivalent radius. The radius of maximum wind varies during the evolution but generally lies in the region between 30–40 km.	29

2.13	Effective diffusivity versus equivalent radius for varying values of the tracer diffusivity κ (units of $\text{m}^2 \text{s}^{-1}$) for the C unstable ring experiment at $t = 6.3$ h.	30
2.14	Normalized effective diffusivity $\Lambda_e(r_e, t) = \kappa_{\text{eff}}(r_e, t)/\kappa$ versus equivalent radius for varying values of the tracer diffusivity κ (units of $\text{m}^2 \text{s}^{-1}$) for the C unstable ring experiment at $t = 6.3$ h.	31
2.15	Sensitivity of effective diffusivity to the initial tracer field. Three curves are shown: Gaussian profile with maximum value of 1000 and linearly decreasing profiles with maximum values of 1000 and 5000.	32
2.16	Sensitivity of effective diffusivity to the number of area points: 50, 200, and 1000. The case shown is the C unstable ring at $t = 6.3$ h.	33
3.1	Vortical swirls observed in the eye of Super Typhoon Yuri (1991). (Credit: Image Science and Analysis Laboratory, NASA-Johnson Space Center)	38
3.2	Isolines of the maximum dimensionless growth rate ν_i/ζ_{av} for azimuthal wavenumbers $m = 3, 4, \dots, 12$. Contours range from 0.1 to 2.7 (lower right), with an interval of 0.1. The shaded regions indicate the wavenumber of the maximum growth rate at each δ (abscissa) and γ (ordinate) point.	43
3.3	Basic state initial condition of various rings. Azimuthal mean relative vorticity, tangential velocity, and pressure are shown for $\gamma = 0.0$ and $\delta = 0.00, 0.05, \dots, 0.85$ (left panels) and for $\gamma = 0.0, 0.1, \dots, 0.9$ and $\delta = 0.75$ (right panels). In the left panels thicker lines indicate increasing δ (rings become thinner) and in the right panels thicker lines indicate increasing γ (rings become more filled).	47
3.4	Fastest growing wavenumber m (Wm) instability at the discrete δ (abscissa) and γ (ordinate) points using the linear stability analysis of S99 (top), and the observed values from the pseudospectral model (bottom). In the top panel, the 'S' denotes that the vortex was stable to exponentially growing perturbations of all azimuthal wavenumbers. The 'U' in the bottom panel signifies that the initial wavenumber of the instability was undetermined.	49
3.5	End states observed in the pseudospectral model after nonlinear vorticity mixing at $t = 48$ h at the discrete δ (abscissa) and γ (ordinate) points	53
3.6	The evolution of the $(\delta, \gamma) = (0.75, 0.20)$ ring (left) and the $(\delta, \gamma) = (0.50, 0.20)$ ring (right). The end states are MP and SP respectively.	54
3.7	The evolution of the $(\delta, \gamma) = (0.55, 0.80)$ ring (left) and the $(\delta, \gamma) = (0.50, 0.50)$ ring (right). The end states are EE and PE respectively.	55
3.8	The evolution of the $(\delta, \gamma) = (0.85, 0.10)$ ring (left) and the $(\delta, \gamma) = (0.25, 0.70)$ ring (right). The end states are MV and TO respectively.	56
3.9	Evolution of the enstrophy $\mathcal{Z}(t)/\mathcal{Z}(0)$ for the rings in Figs. 3.6–3.8. An additional MV curve is plotted for the $(\delta, \gamma) = (0.85, 0.00)$ ring.	57
3.10	The initial ($t = 0$ h; solid curve) and final ($t = 48$ h; dashed curve) azimuthal mean relative vorticity, tangential velocity, and pressure for the $(\delta, \gamma) = (0.70, 0.70)$ ring (left) and the $(\delta, \gamma) = (0.85, 0.00)$ ring (right). The pressure is expressed as a deviation from the environment. The end states of the two rings are SP and MP, respectively.	59

3.11	(top panel) Central pressure change (hPa) from $t = 0$ h to $t = 48$ h for each ring. Negative values (pressure drop) are shaded with $-5 \leq \Delta p_{\min} \leq 0$ in light gray and $\Delta p_{\min} \leq -5$ in dark gray. (bottom panel) Maximum tangential velocity change (m s^{-1}) from $t = 0$ h to $t = 48$ h for each ring: $-7 \leq \Delta \bar{v}_{\max} \leq -3$ (light gray shading) and $\Delta \bar{v}_{\max} \leq -7$ (dark gray shading).	60
4.1	The staggering of variables on the Charney-Phillips grid for the isentropic vertical coordinate model.	71
4.2	The staggering of variables on the Charney-Phillips grid for the sigma vertical coordinate model.	74
4.3	[top panels] The initial wind field $v(r, \theta)$ for the analytic Rankine vortex (left) and the initial condition of the model (right). [bottom panels] Comparison of the analytic $M'(r, \theta)$ (left) to the nonlinear balance initialization of the model (right)	81
4.4	[left panels] The evolution of the azimuthal mean wind field $\bar{v}(r, \theta)$ and [right panels] the evolution of the azimuthal mean montgomery potential deviation $M'(r, \theta)$ for the gradient adjustment simulation.	84
4.5	The azimuthal mean PV (PVU) [top left panel], the azimuthal mean tangential velocity (m s^{-1}) [top right panel], PV (PVU) on the $\theta = 304$ K surface [bottom left panel], and PV (PVU) on the $\theta = 341$ K surface [bottom right panel]. All fields are shown at $t = 0.25$ h.	86
4.6	The azimuthal mean PV (PVU) [top left panel], the azimuthal mean tangential velocity (m s^{-1}) [top right panel], PV (PVU) on the $\theta = 304$ K surface [bottom left panel], and PV (PVU) on the $\theta = 341$ K surface [bottom right panel]. All fields are shown at $t = 12$ h.	87
4.7	The azimuthal mean PV (PVU) [top left panel], the azimuthal mean tangential velocity (m s^{-1}) [top right panel], PV (PVU) on the $\theta = 304$ K surface [bottom left panel], and PV (PVU) on the $\theta = 341$ K surface [bottom right panel]. All fields are shown at $t = 24$ h.	88
4.8	The azimuthal mean PV (PVU) [top left panel], the azimuthal mean tangential velocity (m s^{-1}) [top right panel], PV (PVU) on the $\theta = 304$ K surface [bottom left panel], and PV (PVU) on the $\theta = 341$ K surface [bottom right panel]. All fields are shown at $t = 48$ h.	89
4.9	The azimuthal mean PV (PVU) in our ideal model [left panel] and in the (Yau et al. 2004) full-physics nonhydrostatic model simulation [right panel]. In the right panel, the ordinate is height above sea level in km.	90
4.10	Schematic of the secondary flow in the hurricane eye and eyewall (taken from Willoughby (1998)).	91
4.11	Temporal evolution of the domain integral quantities for the unstable baroclinic vortex simulation. In each panel the values are normalized by the initial value which is shown in the bottom right portion of the plot.	92

5.1	Linear solution to the shallow water equations in cylindrical polar space for varying azimuthal wavenumber: $m = 1$ (top left), $m = 2$ (top right), $m = 3$ (bottom left), $m = 4$ (bottom right). The radial wavenumber $k = 0.04 \text{ km}^{-1}$ is held fixed. The contour intervals for h', ζ' and δ' are 20 m, $2 \times 10^{-7} \text{ s}^{-1}$, and $5 \times 10^{-5} \text{ s}^{-1}$, respectively. The perturbation height h' is set to a maximum amplitude of 100 m, and all other variables are determined from this value.	100
5.2	Linear solution to the shallow water equations in cylindrical polar space for varying radial wavenumber: $k = 0.01$ (top left), $k = 0.025$ (top right), $k = 0.05$ (bottom left), $k = 0.10$ (bottom right) km^{-1} . The azimuthal wavenumber $m = 2$ is held fixed. The contour intervals for h', ζ' and δ' are 20 m, $2 \times 10^{-7} \text{ s}^{-1}$, and $5 \times 10^{-5} \text{ s}^{-1}$, respectively. The perturbation height h' is set to a maximum amplitude of 100 m, and all other variables are determined from this value.	101
5.3	The potential vorticity P for $m = 2$, $k = 0.01 \text{ km}^{-1}$, $f = 0.000037 \text{ s}^{-1}$, and $\bar{h} = 4285 \text{ m}$. The contour plot was made with 100 contour levels of P to illustrate that P is invariant as IGWs propagate.	102
5.4	The relative vorticity ζ (left panel) and pressure p (right panel) at $t = 0 \text{ h}$. The divergence δ (not shown) is initially zero.	103
5.5	Composite radar reflectivity (dBz) of Hurricane Ivan from NOAA P-3 aircraft. [credit: NCDC/NOAA/AOML/Hurricane Research Division].	104
5.6	Early evolution of relative vorticity (left panels) and divergence (right panels) in the shallow water simulation.	106
5.7	Later evolution of relative vorticity (left panels) and divergence (right panels) in the shallow water simulation.	107
5.8	Hovmöller plots of relative vorticity (top panel) and divergence (bottom panel) in the shallow water simulation from $t = 24\text{--}25 \text{ h}$. Plots were made by holding the y -coordinate of the vortex center (largest vorticity) fixed at each output time level. In the top panel, a and b denote the semi-major and semi-minor axes of the central ellipse, L_e denotes the oscillation period of the central ellipse, and L_o is the oscillation period of the outer low vorticity regions. In the bottom panel, c is the pure gravity wave phase speed, L_{IG} is the IGW period and L_R is the radial wavelength.	108
5.9	IGW frequency versus radial wavenumber for $c = 205 \text{ m s}^{-1}$ and $f = 0.000037 \text{ s}^{-1}$	111
5.10	Conceptual diagram of the Kirchhoff vorticity ellipse and associated streamfunction that would be obtained by solving Poisson's equation (i.e., $\nabla^2\psi = \zeta$) for a nondivergent flow. The ellipse rotates cyclonically (for positive ζ) because the streamfunction is slightly less elliptical than the vorticity patch. This occurs because solving the Poisson equation is a smoothing operation.	112
5.11	Comparison of the outward propagating IGWs in the numerical model simulation (left panels) and according to the linear wave theory (right panels). The linear solution was obtained with $k_R = 0.034 \text{ km}^{-1}$, as determined by frequency matching by ν_e , and azimuthal wavenumber $m = 2$. Moving down, each plot is 3 minutes apart.	113

5.12	The change in the vortex azimuthal mean velocity (left panel) and pressure (right panel) over the 48 h numerical simulation. The solid line denotes $t = 0$ h and the dotted line denotes $t = 48$ h.	114
6.1	Evolution of low-level moisture advection, deep layer vertical wind shear and thickness. Moisture advection is calculated at 1000 hPa and displayed with white contours ($\text{g kg}^{-1} \text{12 h}^{-1}$), the 200 hPa-850 hPa vertical wind shear is plotted in the solid black lines (m s^{-1}), and the 850 hPa-200 hPa thickness is shaded, with increasing heights as lighter shades (interval is 20 m, peak is 10980 m (white), and minimum is 10750 m (black)). Panels: (a) 1200 UTC September 9, (b) 0000 UTC September 10, (c) 1200 UTC September 10, and (d) 0000 UTC September 11. The NHC best track position of Gustav is marked with a "TS" symbol	121
6.2	Sea surface temperatures in the region where Gustav formed (C) from the AVHRR on board the NOAA polar orbiting satellites. The NHC best track position of the storm is marked by black circles: (1) 09/1200 UTC [31.6°N, 73.6°W], (2) 09/1800 UTC [31.9°N, 74.5°W], (3) 10/0000 UTC [32.1°N, 75.5°W], (4) 10/0600 UTC [33.0°N, 75.5°W], (5) 10/1200 UTC [33.7°N, 75.4°W], (6) 10/1800 UTC [35.0°N, 75.4°W], and (7) 11/0000 UTC [35.5°N, 74.7°W] (Figure is courtesy of the Johns Hopkins University Applied Physics Laboratory.)	122
6.3	Near-surface wind barbs and absolute vertical vorticity (in units of 10^{-5}s^{-1}) derived from the QuikSCAT scatterometer during 9-10 September 2002. Each contour represents an interval of $20 \times 10^{-5} \text{s}^{-1}$. Panels: (a) ascending pass at 0950 UTC September 9, (b) descending pass at 2350 UTC September 9 (c) ascending pass at 1106 UTC September 10, and (d) descending pass at 2325 UTC September 10. The NHC best track storm center fix is marked by the "TS" symbol. The direction of satellite movement and the UTC time of the eastern and western edge of the pass are also marked on the plot. . . .	124
6.4	Large-scale visible satellite image of Gustav at 1945 UTC on Sept 9. Multiple hot towers and two exposed mesovortices are evident	127
6.5	Representative sounding from of inflow air into Gustav on September 10 (courtesy of the University of Wyoming)	128
6.6	GOES-8 visible close-up depiction of mesovortices in Gustav at 1815 and 1945 UTC on September 9. The overshooting convective tops associated with multiple hot towers are circled in black and marked "HTs". The low level exposed mesovortices are circled in white and marked with "MV". The low level motion of the MVs is shown by the white arrows. The approximate scales of the structures can be discerned from the scale of the latitude-longitude box: 32-33° N (110 km) by 74-75° E (94 km). The system-scale low-level circulation is shown by the white arrows.	132
6.7	Mesovortices in T.S. Gustav on September 10. Panels: (a) 1615 UTC September 10, (b) 1925 UTC September 10	133

6.8 Partial evidence of the axisymmetrization of a low level mesovortex. At 2125 UTC 9 Sept 2002, MV1 appears to be strained and elongated from its earlier circular structure. The broader low level circulation is shown by the white arrows. 133

TABLES

2.1	Unstable vorticity ring parameters: ζ values are in 10^{-3} s^{-1} and r values are in km.	24
3.1	End State Definitions	52

Chapter 1

INTRODUCTION

This dissertation is a compilation of journal papers that are either already submitted or published, or nearly ready to be submitted. There are five separate papers. Each paper adds new insight into structural evolution and intensity change of tropical cyclones due solely to internal dynamical processes, i.e., in the absence of environmental influences (e.g., vertical wind shear) and ocean surface fluxes. Each chapter has its own introduction and conclusions section, and is meant to be read as a separate entity. Here, a brief overview of each chapter is given.

In chapter 2, the Hendricks and Schubert (2008) paper is given. In this paper, the effective diffusivity diagnostic is used to map out two-dimensional transport and mixing properties of hurricanes. An analysis of vortex Rossby wave dynamics contributing to internal mixing is undertaken for some idealized hurricane-like vortices in a nondivergent barotropic model. The results lend new insight into how passive tracers are radially mixed in hurricanes. Insights into internal mechanisms of hurricane intensity change are discussed in light of the results.

In chapter 3, the Hendricks et al. (2008) paper is given. This is a systematic study of structural and intensity changes in hurricanes due to potential vorticity (PV) mixing in the inner-core (eye and eyewall) resulting from dynamic instability of the eyewall PV ring. A sequence of numerical experiments is conducted covering a parameter space that represents all possible barotropic hurricane-like vortices, and the complete lifecycle of each PV ring is assessed.

In chapter 4, a draft of the Hendricks et al. (2009a) paper is given. Two mesoscale hydrostatic primitive equation models are described that are well-suited for idealized studies of geophysical vortex dynamics. The models were developed from a pre-existing periodic spectral shallow water model. The first model uses an isentropic vertical coordinate and the second uses a sigma (terrain following) vertical coordinate. Some verification and validation tests are presented, along with some simulations of evolution of hurricane-like PV hollow towers (the generalization of vorticity rings to the stratified atmosphere). Portions of this chapter will be used in the final paper, which will be devoted to understanding structural and intensity change resulting from three-dimensional PV mixing.

In chapter 5, a draft of the Hendricks et al. (2009b) paper is given. An analysis of a shallow water model simulation of a dynamically active tropical cyclone core is undertaken to understand aspects of spontaneous inertia-gravity wave emission from hurricanes. The conditions that favor spontaneous radiation are assessed. This work adds to the growing body of literature on spontaneous adjustment emission from atmospheric jets and vortices.

Finally, in chapter 6, the Hendricks and Montgomery (2006) paper is given. This is an observational study examining the evolution of vortical hot towers (VHTs) in tropical cyclone Gustav (2002). A large portion of Gustav was exposed due to vertical shear, uncovering multiple convectively generated low level mesovortices that originated from VHTs, but became decoupled due to the vertical shear. Synoptic-scale and mesoscale observations were used to understand the tropical transition that occurred, and comparisons were made between the observed mesoscale events and recent cloud resolving numerical simulations.

The broad conclusions of this dissertation, unifying the individual conclusions in each chapter, are given in chapter 7.

Chapter 2

BAROTROPIC ASPECTS OF TRANSPORT AND MIXING IN HURRICANES

2.1 Abstract

The two-dimensional transport and mixing properties of evolving hurricane-like vortices are examined using the effective diffusivity diagnostic on the output of numerical simulations with a nondivergent barotropic model. The internal dynamical processes causing mixing, as well as the location and magnitude of both chaotic mixing and partial barrier regions are identified in the evolving vortices. Breaking potential vorticity (PV) waves in hurricanes are found to create chaotic mixing regions of finite radial extent (approximately 20–30 km). These waves may break as a result of axisymmetrization or dynamic instability. For monotonic vortices, the wave breaking may create a surf zone outside the radius of maximum wind, while the vortex core remains a partial barrier. Although on a much smaller scale, this hurricane surf zone is analogous to the surf zone outside the wintertime stratospheric polar vortex. For unstable vorticity rings, which are analogous to intensifying hurricanes, the inner and outer breaking PV waves are quite effective at radially mixing a passive tracer locally. The horizontal mixing associated with the inner, breaking PV wave would support the hurricane superintensity mechanism, provided the passive tracer is equivalent potential temperature with a maximum in the eye. For thin rings, which are very dynamically unstable, the entire hurricane inner-core can become a chaotic mixing region during the breakdown, and passive tracers can be quickly mixed between the eye, eyewall, and local environment. Both primary and secondary azimuthal jets in hurricanes are iden-

tified as partial barriers. A surprising result is that for dynamically unstable thick rings, the disturbance exponential growth rates are small enough that the primary azimuthal jet may remain a partial barrier for a long time, even though the inner and outer PV waves are breaking. Consistent with past work, strong PV gradients in hurricanes are found to be barriers to mixing.

2.2 Introduction

Although large-scale environmental factors such as vertical wind shear and sea surface temperature are known to play an important role in intensity change of hurricanes, the role of internal dynamical processes is not so clearly understood (see the review by Wang and Wu 2004). Some important internal processes are wave-mean flow interaction due to vortex Rossby waves (Montgomery and Kallenbach 1997), potential vorticity (PV) mixing between the eyewall and eye (Schubert et al. 1999; Kossin and Schubert 2001; Montgomery et al. 2002), inner spiral rainbands (Guinn and Schubert 1993; Chen and Yau 2001), eyewall replacement cycles (Willoughby et al. 1982; Houze et al. 2007; Terwey and Montgomery 2008), and mixing of moist entropy between the eye and eyewall (Persing and Montgomery 2003; Braun et al. 2006; Cram et al. 2007). Accurate prediction of hurricane intensity change is currently limited by the lack of a comprehensive understanding of some or all of these processes. In particular, these internal processes may be important factors governing rapid intensification and weakening of hurricanes. As a striking example of the importance of mixing processes in the hurricane inner-core, observational evidence was presented (Montgomery et al. 2006a; Aberson et al. 2006) indicating that Hurricane Isabel (2003) was super-intense (i.e., exceeding its maximum potential intensity as defined by the axisymmetric theory of Emanuel (1986, 1988) due to the persistence of multiple eye mesovortices that transported high moist entropy air into the eyewall. The famous starfish mesovortex pattern (Fig. 2.1) was hypothesized to be largely a result of barotropic instability of the eyewall (Kossin and Schubert 2004).

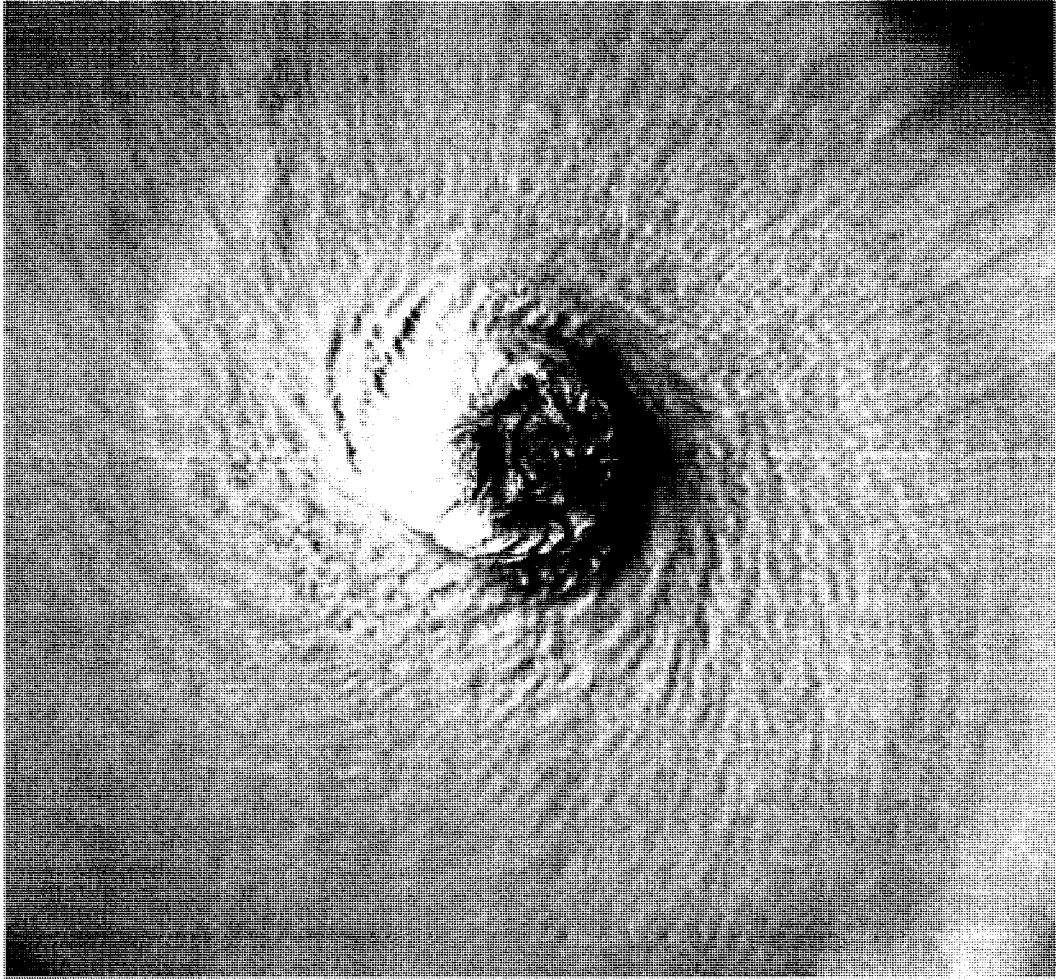


Figure 2.1: Visible satellite image of Hurricane Isabel at 1315 UTC on 12 September 2003 (from Kossin and Schubert 2004).

On the large scale, it is well known that geophysical vortices act as transport barriers. Their persistence as long-lived entities is believed due in part to this tendency. However, in local regions of the vortices and their near environment, strong mixing can occur. For example, it has been shown that Rossby wave breaking on the edge of the wintertime stratospheric vortex (McIntyre and Palmer 1983, 1984) produces long filamentary structures that can mix chemical species from the vortex to the midlatitudes (Waugh and et al. 1994). In complex hurricane flows, similar mixing processes due to vortex Rossby (or PV) wave activity are occurring at smaller scales, helping to determine the spatial distributions of both quasi-passive tracers (e.g., moist entropy or total airborne moisture) and active tracers (e.g., vorticity or potential vorticity).

Mixing is due to the combined effect of differential advection and turbulent (or inevitably, molecular) diffusion. Differential advection (i.e., stirring) stretches and deforms material lines from which diffusion accomplishes true irreversible mixing. The interplay between advection and diffusion in mixing makes it difficult to quantify. Even in rather simple unsteady nonturbulent flows, the phenomenon known as chaotic advection, where particle trajectories are not integrable, has been shown to exist (Aref 1984; Ottino 1989). Recent work has proposed the use of an area (Butchart and Remsberg 1986; Nakamura 1996; Winters and D’Asaro 1996; Shuckburgh and Haynes 2003) hybrid Eulerian-Lagrangian coordinate system that separates the reversible effects of advection (which is absorbed into the coordinate) with the irreversible effects of diffusion. When transforming the advection-diffusion equation into the area coordinate, an effective diffusion (i.e., diffusion only) equation is obtained with a diagnostic coefficient that quantifies the equivalent length (Nakamura 1996) of a tracer contour. As this equivalent length becomes large, there is more interface for diffusion to act and the “effective diffusivity” is larger. Thus the effective diffusivity encompasses aspects of both differential advection and diffusion in mixing. Shuckburgh and Haynes (2003) demonstrated that effective diffusivity is a useful mixing diagnostic for chaotic time-periodic flows.

In recent work the effective diffusivity diagnostic has been used to quantify transport and mixing properties in the upper troposphere and stratosphere (see Haynes and Shuckburgh (2000a,b); Allen and Nakamura (2001); Scott et al. (2003) and references therein). That work compliments the previous use of Lyapunov exponents (e.g., Lapeyre 2002) in large-scale transport and mixing (Pierrhumbert and Yang 1993; Ngan and Shepherd 1999a,b). In the present work, we apply the effective diffusivity diagnostic to aperiodic chaotic advective hurricane-like flows. In three dimensions, transport and mixing can be quite complicated due to interactions of multiscale three dimensional eddies, from the Kolmogorov inertial range to mesovortices that have been observed at scales of 10-50 km (Kossin et al. 2002; Reasor et al. 2005; Sippel et al. 2006; Hendricks and Montgomery 2006). In order to make this problem initially more tractable, we focus our study on two-dimensional hurricane-like vortices in a nondivergent barotropic model framework. Numerical solutions to the nondivergent barotropic vorticity equation and the advection-diffusion equation are obtained with suitable initial conditions, and the effective diffusivity diagnostic is used to quantify barotropic aspects of transport and mixing in a suite of hurricane-like vortices: (i) elliptical vorticity field, (ii) binary vortex interaction, (iii) Rankine vortex embedded in a turbulent background vorticity field, and (iv) unstable vorticity rings. As will be shown, these experiments illustrate some interesting internal barotropic dynamics of tropical cyclone evolution, such as secondary eyewall formation, PV wave breaking surf zones, and PV mixing between the eye and eyewall. The location and magnitude of strong partial barriers (time scale for transport across it is large), weak partial barriers (time scale for transport across it is small), and mixing (chaotic trajectories) regions are identified in these vortices. Implications for the evolution of passive tracers, and their relationship to intensity change, are discussed in light of the results.

The outline of this chapter is as follows. In section 2.2 the dynamical model and passive tracer equation used for this study are described. In section 2.3 we review the derivation of the transformation of the advection-diffusion equation into the area coordinate

and the equivalent radius coordinate, yielding the effective diffusivity diagnostic in a form useful for hurricane studies. In section 2.4 we present pseudospectral model results for several types of mixing scenarios believed to be relevant in hurricane dynamics. In section 2.5 we document the relative insensitivity of the effective diffusivity diagnostic to certain arbitrary choices made in its calculation from solutions of the passive tracer equation. Finally, the main conclusions of this study are presented in section 2.6.

2.3 Dynamical model and passive tracer equation

The dynamical model used here considers two-dimensional, nondivergent motions on a plane. The governing vorticity equation is

$$\frac{\partial \zeta}{\partial t} + \mathbf{u} \cdot \nabla \zeta = \nu \nabla^2 \zeta, \quad (2.1)$$

where $\mathbf{u} = \mathbf{k} \times \nabla \psi$ is the horizontal, nondivergent velocity, $\zeta = \nabla^2 \psi$ is the relative vorticity, and ν is the constant viscosity. The solutions presented here were obtained with a double Fourier pseudospectral code having 768×768 equally spaced points on a doubly periodic, $600 \text{ km} \times 600 \text{ km}$ domain. Since the code was run with a dealiased calculation of the nonlinear term in (2.1), there were 256×256 resolved Fourier modes. The wavelength of the highest Fourier mode is 2.3 km. A fourth-order Runge-Kutta scheme was used for time differencing, with a 3.5 s time step. The value of viscosity was chosen to be $\nu = 50 \text{ m}^2 \text{ s}^{-1}$, so the characteristic damping time for modes having total wavenumber equal to 256 is 2.4 hours, while the damping time for modes having total wavenumber equal to 170 is 5.5 hours.

As a way to understand the transport and mixing properties of an evolving flow described by (2.1), it is useful to also calculate the evolution of a passive tracer subject to diffusion and to advection by the nondivergent velocity \mathbf{u} . The advection-diffusion equation for this passive tracer is

$$\frac{\partial c}{\partial t} + \mathbf{u} \cdot \nabla c = \nabla \cdot (\kappa \nabla c), \quad (2.2)$$

where $c(x, y, t)$ is the concentration of the passive tracer and κ is the constant diffusivity. The numerical methods used to solve (2.2) are identical to those used to solve (2.1). However, the results to be presented here have quite different initial conditions on ζ and c . The passive tracer c is always initialized as an axisymmetric and monotonic function. We have chosen both linear and Gaussian functions with maxima at the vortex center. In contrast, the initial vorticity is not necessarily monotonic with radius (e.g., it may have the form of a barotropically unstable vorticity ring) and is not necessarily axisymmetric.

2.4 Area coordinate transformation and effective diffusivity

To aid in the derivation, a diagram of the area coordinate is shown in Fig. 2.2. Consider the transform from Cartesian (x, y) coordinates to tracer (C, s) coordinates, where C is a particular contour of the $c(x, y, t)$ field and s is the position along that contour. Let dC be the differential element of C and ds be the differential element of s . Let $A(C, t)$ denote the area of the region in which the tracer concentration satisfies $c(x, y, t) \geq C$, i.e.,

$$A(C, t) = \iint_{c \geq C} dx dy. \quad (2.3)$$

Let $\gamma(C, t)$ denote the boundary of this region. Note that $A(C, t)$ is a monotonically decreasing function of C and that $A(C_{\max}, t) = 0$. Now define \mathbf{u}^C as the velocity of the contour C , so that

$$\frac{\partial c}{\partial t} + \mathbf{u}^C \cdot \nabla c = 0. \quad (2.4)$$

Noting that $\nabla c / |\nabla c|$ is the unit vector normal to the contour, we can use (2.3) and (2.4) to write

$$\begin{aligned} \frac{\partial A(C, t)}{\partial t} &= \frac{\partial}{\partial t} \iint_{c \geq C} dx dy \\ &= - \int_{\gamma(C, t)} \mathbf{u}^C \cdot \frac{\nabla c}{|\nabla c|} ds \\ &= \int_{\gamma(C, t)} \frac{\partial c}{\partial t} \frac{ds}{|\nabla c|}. \end{aligned} \quad (2.5)$$

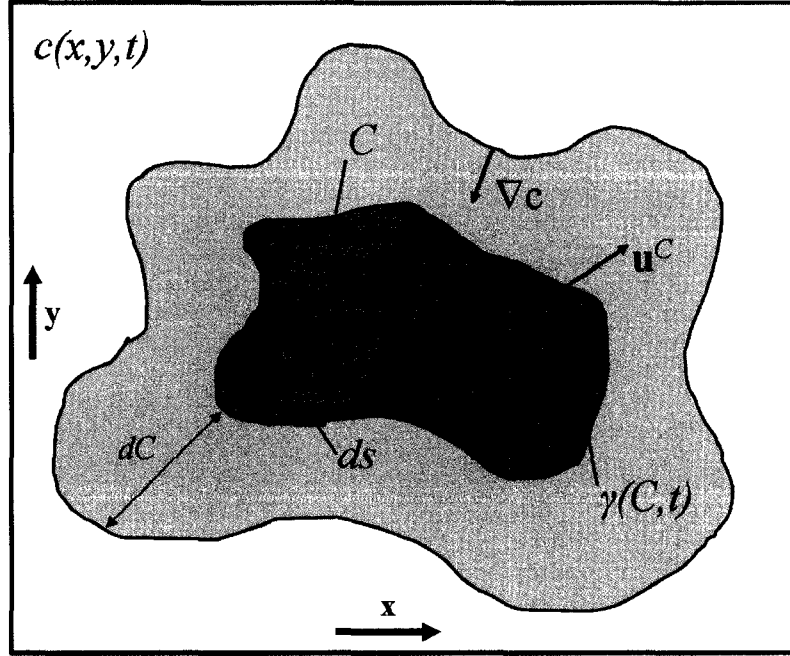


Figure 2.2: Diagram of the area coordinate. Two hypothetical contours C of the tracer field $c(x, y, t)$ are shown with corresponding area above the contours $A(C, t)$. The other parameters used in the derivation are illustrated as well.

Using (2.2) in the last equality of (2.5) we obtain

$$\frac{\partial A(C, t)}{\partial t} = \int_{\gamma(C, t)} \nabla \cdot (\kappa \nabla c) \frac{ds}{|\nabla c|} - \int_{\gamma(C, t)} \mathbf{u} \cdot \nabla c \frac{ds}{|\nabla c|}. \quad (2.6)$$

We now note that (since $dx dy = ds dC' / |\nabla c|$)

$$\begin{aligned} \frac{\partial}{\partial C} \iint_{c \geq C} () dx dy &= \frac{\partial}{\partial C} \iint_{c \geq C} () \frac{ds dC'}{|\nabla c|} \\ &= - \int_{\gamma(C, t)} () \frac{ds}{|\nabla c|}. \end{aligned} \quad (2.7)$$

Using (2.7) in (2.6) while noting that $\mathbf{u} \cdot \nabla c = \nabla \cdot (c\mathbf{u})$ because \mathbf{u} is nondivergent, we obtain

$$\begin{aligned} \frac{\partial A(C, t)}{\partial t} &= - \frac{\partial}{\partial C} \iint_{c \geq C} \nabla \cdot (\kappa \nabla c) \frac{ds dC'}{|\nabla c|} \\ &\quad + \frac{\partial}{\partial C} \iint_{c \geq C} \nabla \cdot (c\mathbf{u}) \frac{ds dC'}{|\nabla c|} \\ &= - \frac{\partial}{\partial C} \int_{\gamma(C, t)} \kappa |\nabla c| ds \\ &\quad + \frac{\partial}{\partial C} \int_{\gamma(C, t)} c\mathbf{u} \cdot \frac{\nabla c}{|\nabla c|} ds. \end{aligned} \quad (2.8)$$

The third and fourth lines of (2.8) are obtained using the divergence theorem. The fourth line of (2.8) vanishes because the factor c in the integrand can come outside the integral, leaving $\int_{\gamma(C,t)} \mathbf{u} \cdot (\nabla c / |\nabla c|) ds$, which vanishes because \mathbf{u} is nondivergent.

Since $A(C, t)$ is a monotonic function of C , there exists a unique inverse function $C(A, t)$. We now transform (2.8) from a predictive equation for $A(C, t)$ to a predictive equation for $C(A, t)$. This transformation is aided by

$$\frac{\partial A(C, t)}{\partial t} \frac{\partial C(A, t)}{\partial A} = -\frac{\partial C(A, t)}{\partial t}, \quad (2.9)$$

which, when used in (2.8), yields

$$\begin{aligned} \frac{\partial C(A, t)}{\partial t} &= \frac{\partial C(A, t)}{\partial A} \frac{\partial}{\partial C} \int_{\gamma(C,t)} \kappa |\nabla c| ds \\ &= \frac{\partial}{\partial A} \int_{\gamma(C,t)} \kappa |\nabla c| ds. \end{aligned} \quad (2.10)$$

Because of (2.7), the integral $\int_{\gamma(C,t)} \kappa |\nabla c| ds$ on the right hand side of (2.10) can be replaced by $(\partial/\partial C) \iint_{e \geq C} \kappa |\nabla c|^2 dx dy$. Then, (2.10) can be written in the form

$$\frac{\partial C(A, t)}{\partial t} = \frac{\partial}{\partial A} \left(K_{\text{eff}}(A, t) \frac{\partial C(A, t)}{\partial A} \right), \quad (2.11)$$

where

$$K_{\text{eff}}(A, t) = \left(\frac{\partial C}{\partial A} \right)^{-2} \frac{\partial}{\partial A} \iint_{e \geq C} \kappa |\nabla c|^2 dx dy. \quad (2.12)$$

To summarize, the area coordinate has been used to transform the advection-diffusion equation (2.2) into the diffusion-only equation (2.11), in the process yielding the effective diffusivity $K_{\text{eff}}(A, t)$. Since $K_{\text{eff}}(A, t)$ can be computed from (2.12), it can serve as a useful diagnostic tool to help understand the interplay of advection and diffusion in (2.2). However, note that, because of the use of A as an independent variable, the effective diffusivity $K_{\text{eff}}(A, t)$ has the rather awkward units $\text{m}^4 \text{s}^{-1}$. This is easily corrected by mapping the area coordinate into the equivalent radius coordinate r_e , which is defined by $\pi r_e^2 = A$. Thus, transforming (2.11) to the equivalent radius using $2\pi r_e (\partial/\partial A) = (\partial/\partial r_e)$, we obtain

$$\frac{\partial C(r_e, t)}{\partial t} = \frac{\partial}{r_e \partial r_e} \left(r_e K_{\text{eff}}(r_e, t) \frac{\partial C(r_e, t)}{\partial r_e} \right) \quad (2.13)$$

where

$$\kappa_{\text{eff}}(r_e, t) = \frac{K_{\text{eff}}(A, t)}{4\pi A}. \quad (2.14)$$

Note that, with the use of r_e as an independent variable, the effective diffusivity $\kappa_{\text{eff}}(r_e, t)$ has the units $\text{m}^2 \text{s}^{-1}$. Two other interesting diagnostics are the equivalent length, defined by

$$L_e(r_e, t) = \left(\frac{\kappa_{\text{eff}}(r_e, t)}{\kappa} \right)^{1/2} 2\pi r_e, \quad (2.15)$$

and the normalized effective diffusivity,

$$\Lambda_e(r_e, t) = \left(\frac{L_e(r_e, t)}{2\pi r_e} \right)^2 = \frac{\kappa_{\text{eff}}(r_e, t)}{\kappa}. \quad (2.16)$$

Since the minimum value of κ_{eff} is κ , we conclude that $L_e(r_e, t) \geq 2\pi r_e$. As will be shown, $L_e(r_e, t)$ greatly exceeds $2\pi r_e$ during strong mixing. The $\Lambda_e(r_e, t)$ diagnostic is the best measure of chaotic advection because it is normalized by the tracer diffusivity. It may be the most relevant effective diffusivity diagnostic for direct comparisons to Lagrangian mixing diagnostics such as Finite Time Lyapunov Exponents (FTLEs).

The effective diffusivity diagnostics $K_{\text{eff}}(A, t)$, $\kappa_{\text{eff}}(r_e, t)$, $L_e(r_e, t)$, and $\Lambda_e(r_e, t)$ can be calculated at a given time t from the output $c(x, y, t)$ of the numerical solution of (2.2). The calculation of $K_{\text{eff}}(A, t)$ involves the following discrete approximation of the right hand side of (2.12). First, the desired number of area coordinate points is chosen ($n_A = 200$ for the results shown here). The tracer contour interval is set using $\Delta C = [\max(c) - \min(c)]/n_A$. Next, $|\nabla c|^2$ is calculated at each model grid point. Then, a discrete approximation of the function $A(C, t)$ is determined by adding up the area within each chosen C contour, i.e., by using a discrete approximation to (2.3). The discrete approximation to $A(C, t)$ is then converted to a discrete approximation of its inverse, $C(A, t)$. The denominator of the effective diffusivity diagnostic, $(dC/dA)^2$, is calculated by taking second order accurate finite differences of $C(A, t)$. The numerator of the right hand side of (2.12) is then calculated in the same manner, which completes the calculation of the effective diffusivity $K_{\text{eff}}(A, t)$. The remaining effective diffusivity diagnostics $\kappa_{\text{eff}}(r_e, t)$, $L_e(r_e, t)$, and $\Lambda_e(r_e, t)$ are then

easily computed using (2.14)–(2.17). As will be shown, plots of these diagnostics reveal the locations of partial barrier and mixing regions in the vortex.

For comparison purposes it is useful to have solutions of (2.13) for the special case $\kappa_{\text{eff}} = \kappa$ and $r_e = r$. These can also be interpreted as solutions of (2.2) for the special case in which \mathbf{u} is purely azimuthal and the passive tracer concentration c remains axisymmetric. One such solution can be easily obtained on an infinite domain for the initial condition

$$C(r, 0) = C_0 \exp\left(-\frac{r^2}{r_0^2}\right), \quad (2.17)$$

where C_0 and r_0 are specified constants. The solution is

$$C(r, t) = C_0 \left(\frac{r_0^2}{r_0^2 + 4\kappa t}\right) \exp\left(-\frac{r^2}{r_0^2 + 4\kappa t}\right). \quad (2.18)$$

In the next section, two-dimensional plots of effective diffusivity will be shown. This can be done because effective diffusivity is constant along a tracer contour, and tracer contours meander in (x, y) space. From another point of view, $\kappa_{\text{eff}}(r_e, t)$ can be mapped to $\kappa_{\text{eff}}(x, y, t)$ because each horizontal grid point is associated with an equivalent radius.

2.5 Pseudospectral model experiments and results

We now use the effective diffusivity diagnostic to understand the transport and mixing properties of a number of idealized hurricane-like vortices. The cases selected here are: (i) an elliptical vorticity field, (ii) a binary vortex interaction, (iii) a Rankine-like vortex embedded in a random turbulent vorticity field, and (iv) breakdown of unstable vorticity rings. All of the experiments are unforced and exhibit properties of two dimensional turbulence, in particular the selective decay of enstrophy over kinetic energy. In the following subsections, the initial condition and parameters for each experiment are shown, and the results are presented and discussed.

2.5.1 Elliptical vorticity field

The initial elliptical vorticity field is constructed in a manner similar to Guinn (1992).

In polar coordinates, the initial vorticity field is specified by

$$\zeta(r, \phi, 0) = \zeta_0 \begin{cases} 1 & 0 \leq r \leq r_i \alpha(\phi) \\ 1 - f_\lambda(r') & r_i \alpha(\phi) \leq r \leq r_0 \alpha(\phi), \\ 0 & r_0 \alpha(\phi) \leq r \end{cases} \quad (2.19)$$

where $\alpha(\phi)$ is an ellipticity augmentation factor described in the next paragraph. Here, ζ_0 is the maximum vorticity at the center, $f_\lambda(r') = \exp[-(\lambda/r') \exp(1/(r' - 1))]$ is a monotonic shape function with transition steepness parameter λ , $r' = (r - r_i \alpha(\phi)) / (r_0 \alpha(\phi) - r_i \alpha(\phi))$ is a nondimensional radius proportional to $r = (x^2 + y^2)^{1/2}$, and r_i and r_0 are the radii where the vorticity begins to decrease and where it vanishes, respectively. For the special case of $\alpha(\phi) = 1$ the field is axisymmetric.

This field may then be deformed into an ellipse by specifying an eccentricity $\epsilon = (1 - (b^2/a^2))^{1/2}$, where a is the semi-major axis and b is the semi-minor axis of the ellipse $(x/a)^2 + (y/b)^2 = 1$. Using the eccentricity and the angle ϕ , an augmentation factor $\alpha(\phi) = ((1 - \epsilon^2) / (1 - \epsilon^2 \cos^2(\phi)))^{1/2}$ may be defined, and when used in (2.20) the field is changed to elliptical for $0 < \epsilon < 1$. For the experiment conducted, $\lambda = 2.0$, $\epsilon = 0.70$, and the radii r_i and r_0 were set to 30 km and 60 km, respectively.

Plots of vorticity and effective diffusivity κ_{eff} at $t = 1.5$ h during the evolution of the elliptical vorticity field are shown in Fig. 2.3. At this time, two filaments of high vorticity associated with breaking PV waves are clearly visible. Associated with these filaments are regions of large effective diffusivity. The effective diffusivity peaks just upwind of the filaments and extends further upwind. The main vortex acts as a transport barrier during the filamentation. In terms of an arbitrary passive tracer, these results indicate that the tracer will tend to be well-mixed horizontally in the wave breaking surf zone, and tracers initially in the vortex core will be trapped there. During its evolution, continued wave

breaking episodes occur as the ellipse tries to axisymmetrize. However, axisymmetrization is not complete here within $t \leq 48$ h, and the surf zone is a robust feature throughout the entire simulation. The persistence of the surf zone is clearly illustrated in Fig. 2.4, where the equivalent length and normalized effective diffusivity are large. The ability of an elliptical vorticity field to axisymmetrize (Melander et al. 1987) via inviscid dynamics was shown to be determined by the sharpness of its edge (Dritschel 1998). If the vortex is more Rankine-like (i.e., possessing a sharp edge), it will tend to rotate and not generate filaments. If, on the other hand, the transition is not sharp, there will be a tendency to generate filaments and axisymmetrize.

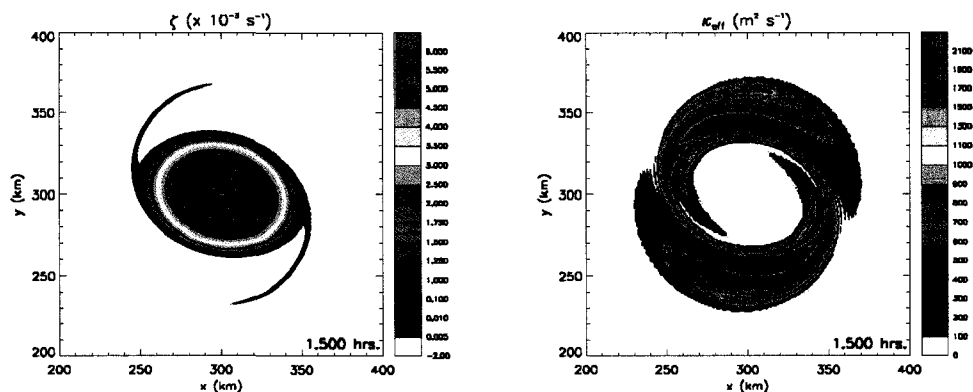


Figure 2.3: The relative vorticity and effective diffusivity κ_{eff} for the evolution of the elliptical vorticity field at $t = 1.5$ h.

Although it occurs on much smaller time and length scales, there is an analogy between this surf zone in tropical cyclones and the planetary Rossby wave breaking surf zone associated with the wintertime stratospheric polar vortices (McIntyre and Palmer 1983, 1984, 1985; McIntyre 1989; Jukes and McIntyre 1992; Bowman 1993; Waugh and et al. 1994). Planetary waves excited in the troposphere may propagate vertically and cause wave breaking to occur on the edge of the stratospheric polar vortex, from which chemical constituents can be mixed into the midlatitudes. The wintertime stratospheric polar vortices display similar processes to our experiment, namely the core vortex is a transport barrier and the surf zone is a chaotic mixing region. The existence of the main

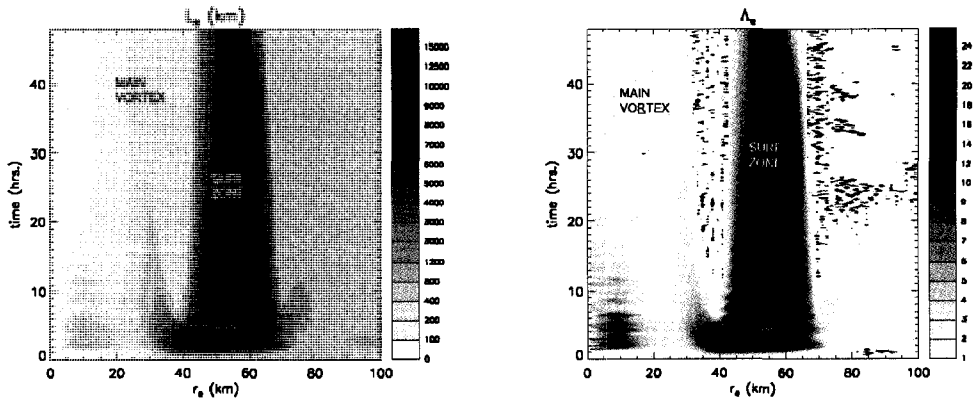


Figure 2.4: Hovmöller plots of the equivalent length $L_e(r_e, t)$ (left panel) and dimensionless equivalent length $\Lambda_e(r_e, t)$ (right panel) for the evolution of the elliptical vorticity field. Two consistent regions are evident throughout the simulation: the *main vortex* partial barrier and the *surf zone* chaotic mixing region.

vortex barrier was thought to be due to the strong PV gradient, a restoring mechanism for perturbations imposed upon it. Rossby wave breaking has also been examined in more idealized frameworks (Polvani and Plumb 1992; Koh and Plumb 2000).

In tropical cyclones, the deformation of an initially circular vortex core to an ellipse may happen due to external (e.g., vertical shear) or internal (e.g., PV generation by asymmetric moist convection) processes. The relaxation to axisymmetry will produce wave breaking episodes, and, as we have shown here, moderate mixing regions in the associated surf zone.

2.5.2 Binary vortex interaction

The initial condition for the binary vortex interaction cases are two Gaussian vortices defined by $\zeta(r, 0) = \zeta_m e^{-r^2/b^2}$, where r is the distance from the vortex center, b is the horizontal scale of the vortex and ζ_m is the peak vorticity at the center. For the experiment, we use $\zeta_m = 6.0 \times 10^{-3} \text{ s}^{-1}$ and $1.0 \times 10^{-3} \text{ s}^{-1}$, and $b = 15 \text{ km}$ and 45 km , for the strong and weak vortices, respectively. The vortex centers are initially 75 km apart.

Theoretical work on binary vortex interactions has been done by Dritschel and Waugh

(1992), who developed a classification scheme for these interactions based upon the separation distance and the ratio of the initial patch radii. Based on these two parameters, five regimes were identified: (a) complete merger, (b) partial merger, (c) complete straining out, (d) partial straining out, and (e) elastic interaction. Generally, as the separation distance increases, there is a tendency to move from (a) to (e). This theoretical work was extended to the binary interaction of tropical cyclones (Ritchie and Holland 1993; Prieto et al. 2003) and into vortex interactions within the tropical cyclone (Kuo et al. 2004, 2008). Kuo et al. (2004) examined the straining out regime further to describe a barotropic mechanism for the formation of concentric vorticity structures in typhoons. The experiment conducted here is in the straining-out regime ((c) or (d)) and forms a secondary ring of enhanced vorticity.

Relative vorticity and effective diffusivity for the binary vortex experiment are shown in Fig. 2.5. The initial condition (top panel) shows the two vortices, with the stronger one north of the weaker one. Progressing to the middle panels, at $t = 4.0$ h the stronger vortex is completely straining out the weaker vortex. During this period the effective diffusivity shows a mixing region in the strong vortex (with oscillatory rings), and a mixing region associated with the large spiral band from the strained out weaker vortex. Similar to the elliptical vorticity case, the enhanced mixing region extends from the filamentary structure upwind. By $t = 24.0$ h, the core vortex has completely strained out the weaker vortex into a thin secondary ring (bottom left panel) and a low vorticity moat exists between the two vorticity regions. At this time the effective diffusivity (bottom right panel) shows a partial barrier region associated with the vortex core, and a mixing region extending radially outward.

Hovmöller plots of effective diffusivity and normalized effective diffusivity are shown in Fig. 2.6. Two important features to note are that the mixing region moves radially outward in time and the core vortex becomes more of a transport barrier region. Thus, during binary vortex interactions, the “victorious” vortex tends to isolate itself and become

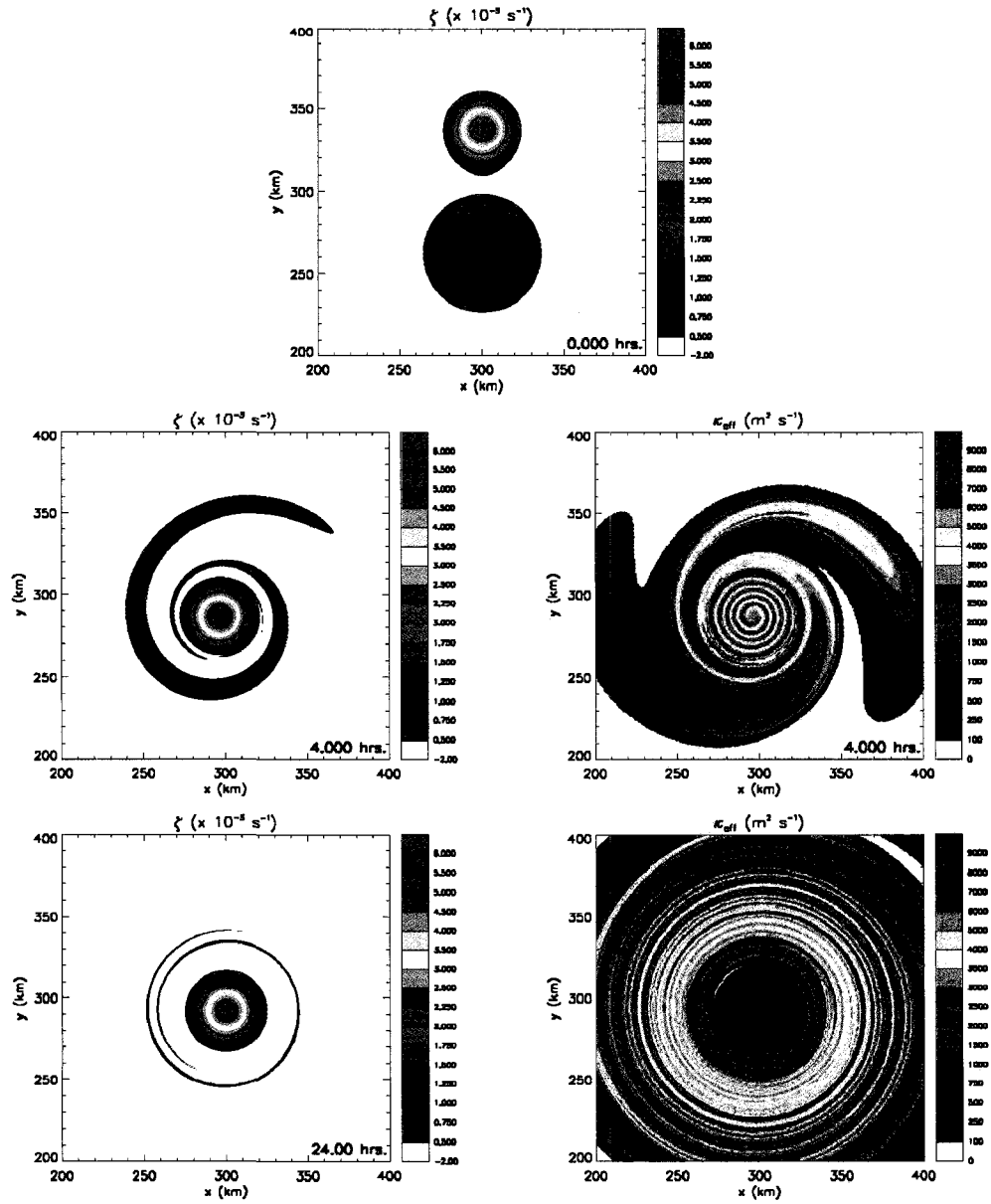


Figure 2.5: The initial vorticity field (top panel) and side-by-side panels (at 4 h and 24 h) of relative vorticity and effective diffusivity for the binary vortex interaction. The model domain is 600 km by 600 km, but only the inner 200 km by 200 km is shown.

resistant to radial mixing.

To illustrate how the initial tracer field is modified by the binary vortex interaction, side-by-side Hovmöller plots of the numerical and analytic solution, equation (2.19), are

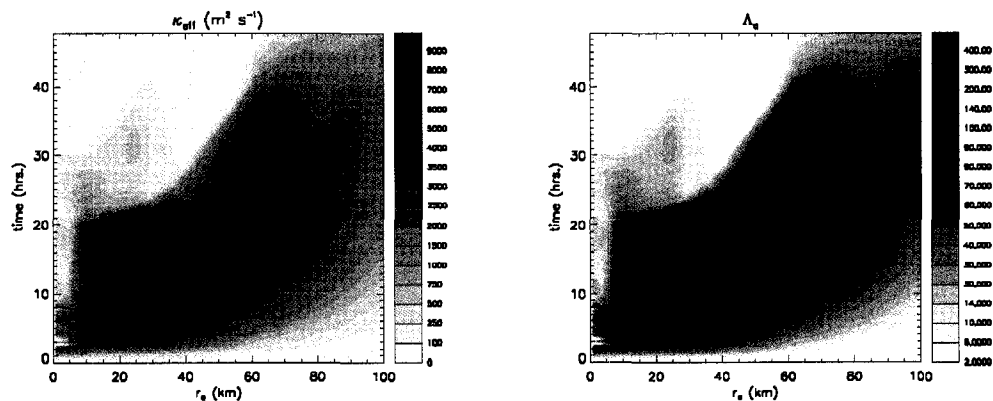


Figure 2.6: Hovmöller plots of $\kappa_{\text{eff}}(r_e, t)$ (left panel) and $\Lambda_e(r_e, t)$ (right panel) for the binary vortex interaction.

shown in Fig. 2.7. The analytic solution is obtained using $\kappa = \kappa_{\text{eff}} = 2500 \text{ m}^2 \text{ s}^{-1}$, which is approximately the average effective diffusivity during the interaction (Fig. 2.6 left panel). Although there are differences, the broadening of the tracer concentration with time from its initial Gaussian form is evident in both plots. We interpret this result as follows. The advection-diffusion equation was transformed into a diffusion only equation using a quasi-Lagrangian area coordinate that has advection absorbed into it (Eqns. 2.11 and 2.13). Mere diffusion could not possibly smooth out the initial tracer gradient in the short time frame of 48 h. The combined effects of differential advection and diffusion are responsible for smoothing the initial Gaussian tracer field significantly by 48 h. By inserting an average effective diffusivity, which includes differential advection, into the radial diffusion equation (2.13), we were able to obtain a similar evolution of the initial Gaussian tracer field. Thus, in a coarse-grained sense mixing, due to the combined effects of differential advection and diffusion, can be parameterized by a large effective diffusivity in the diffusion-only equation (cf. Bowman 1995).

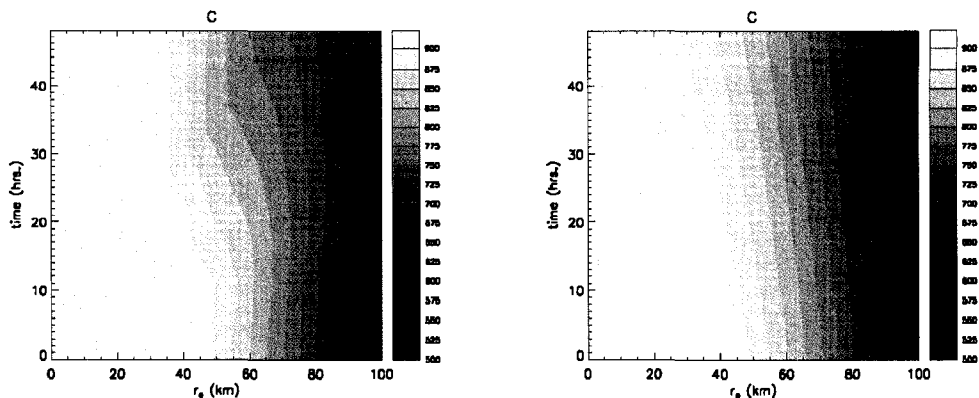


Figure 2.7: Hovmöller plots of the numerical solution (left) and the analytic solution (equation (19); right) of the tracer concentration $C(r_e, t)$ for the binary vortex interaction. The analytic solution is obtained with $\kappa_{\text{eff}} = \kappa = 2500 \text{ m}^2 \text{ s}^{-1}$.

2.5.3 Rankine vortex in a turbulent vorticity field

A Rankine vortex in a stirred vorticity field may be represented mathematically by

$$\zeta(x, y, 0) = \zeta_1 \begin{cases} 1 & 0 \leq r \leq r_1 \\ S\left(\frac{r-r_1}{r_2-r_1}\right) & r_1 \leq r \leq r_2 \\ 0 & r_2 \leq r \end{cases} \quad (2.20)$$

$$+ \zeta_{\text{turb}}(x, y) \begin{cases} 1 & 0 \leq r \leq r_3 \\ S\left(\frac{r-r_3}{r_4-r_3}\right) & r_3 \leq r \leq r_4, \\ 0 & r_4 \leq r \end{cases}$$

where ζ_1 is the maximum vorticity of the Rankine vortex, $S(x) = 1 - 3x^2 + 2x^3$ is a cubic polynomial shape function providing smooth transitions from r_1 to r_2 , and from r_3 to r_4 , and $\zeta_{\text{turb}}(x, y)$ is a random turbulent vorticity field (Rozoff et al. 2006) given by

$$\zeta_{\text{turb}}(x, y) = \sum_{k=-k_{\text{max}}}^{k_{\text{max}}} \sum_{\ell=-\ell_{\text{max}}}^{\ell_{\text{max}}} \zeta_{k,\ell} e^{i(2\pi/L)(kx+\ell y)}. \quad (2.21)$$

Here, k_{max} and ℓ_{max} are the spectral truncation limits in x and y , L is the domain length, $\zeta_{k,\ell}$ is random with maximum amplitude of $1.5 \times 10^{-5} \text{ s}^{-1}$, and the total wavenumber

$\kappa = (k^2 + \ell^2)^{1/2}$ is set for spatial scales primarily between 20 and 40 km. For the experiment, we use $r_1 = 20$ km, $r_2 = 30$ km, $r_3 = 120$ km, $r_4 = 180$ km, and $\zeta_1 = 5 \times 10^{-3} \text{ s}^{-1}$.

As an analogy to real tropical cyclones, the Rankine-like vortex can be thought of as the tropical cyclone core and the stirred vorticity field can be thought of as generated by random convection. The initial condition for this experiment is shown in the top panel of Fig. 2.8. As the simulation evolves, the core vortex begins to axisymmetrize the random vorticity elements. At $t = 9.5$ h the core vortex begins to act like a partial barrier region. Outside the vortex core, chaotic mixing is occurring as the random vorticity anomalies are being axisymmetrized. By $t = 40.0$ h (bottom panels), the relative vorticity exhibits a central monopole, a low vorticity moat, and a secondary ring of enhanced vorticity. Comparing the two bottom panels, the low vorticity moat is coincident with the ring of moderate effective diffusivity ($100 \leq \kappa_{\text{eff}} \leq 250 \text{ m}^2 \text{ s}^{-1}$). In real tropical cyclones, the moat region is a region of suppressed convective activity due to the combined effects of subsidence (Schubert et al. 2007) and strain-dominated flow (Rozoff et al. 2006). The moat here was identified as a region of enhanced mixing. The secondary ring of enhanced vorticity is coincident with the ring of low effective diffusivity ($\kappa_{\text{eff}} \leq 100 \text{ m}^2 \text{ s}^{-1}$). The azimuthal mean wind (not shown) associated with the bottom left panel of Fig. 2.8 has two maxima. The first is the primary azimuthal jet located at the edge of the central vorticity monopole, and the second is the secondary azimuthal jet that occurs at the outer edge of the secondary ring of enhanced vorticity. In the effective diffusivity plot, these jets are partial barriers (white rings) with $\kappa_{\text{eff}} \leq 100 \text{ m}^2 \text{ s}^{-1}$. Therefore, azimuthal jets in hurricanes are likely to be transport barriers, resistant to horizontal mixing.

2.5.4 *Unstable vorticity rings*

Five experiments were conducted for different unstable hurricane-like vortices. The initial vorticity field consists of a vorticity ring (the eyewall) and a relatively low vorticity center (the eye). Observations (Kossin and Eastin 2001; Mallen et al. 2005) indicate that

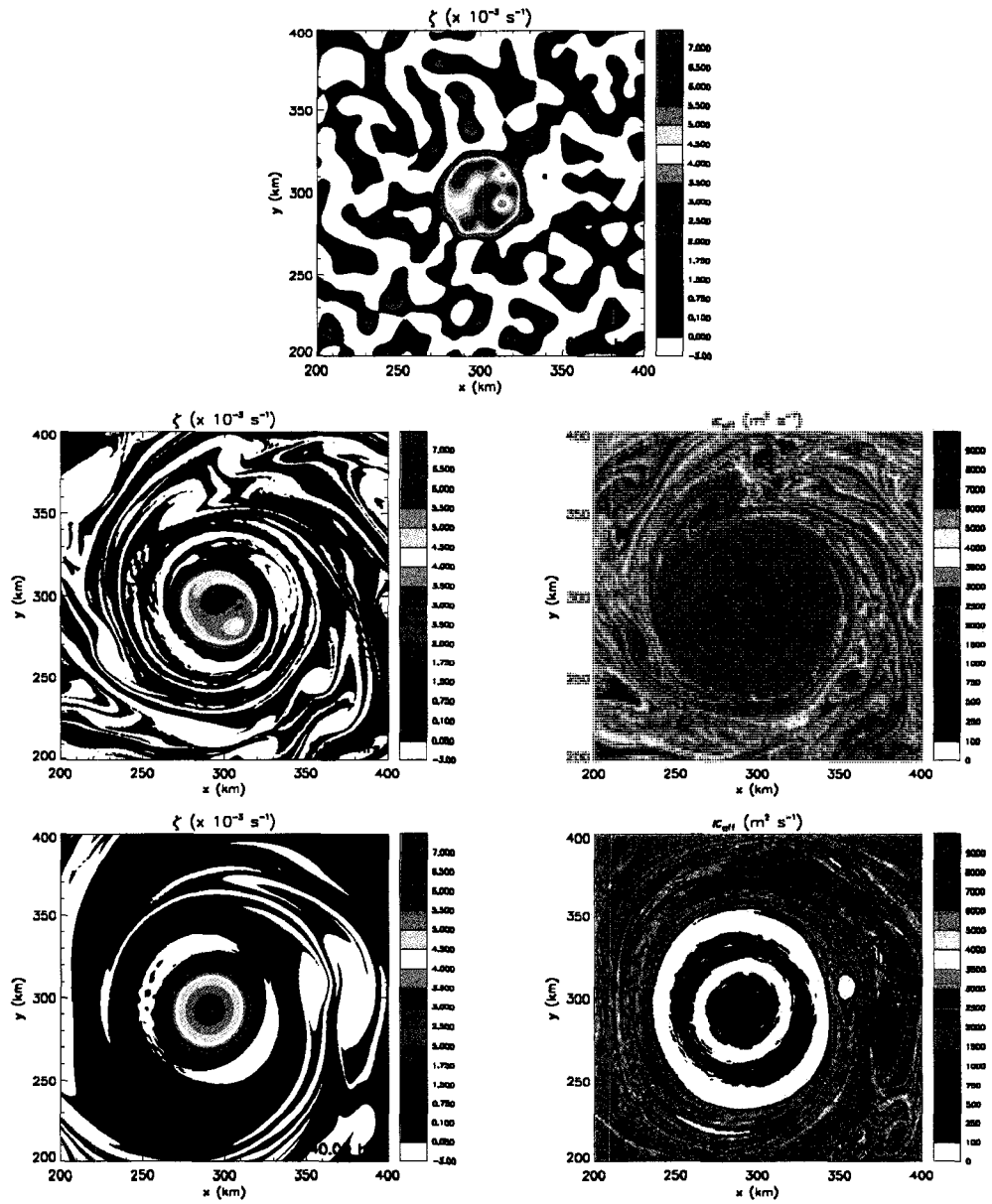


Figure 2.8: The initial vorticity field (top panel) and side-by-side panels (at 9.5 h and 40 h) of relative vorticity and effective diffusivity for the Rankine-like vortex in a turbulent vorticity field. The model domain is 600 km by 600 km, but only the inner 200 km by 200 km is shown.

strong or intensifying hurricanes are often characterized by such vorticity fields. The average vorticity over the inner-core was set to be $\zeta_{av} = 2.0 \times 10^{-3} \text{ s}^{-1}$, corresponding to a peak

tangential wind of approximately 40 m s^{-1} in each case.

The initial condition on the vorticity is given in polar coordinates by $\zeta(r, \phi) = \bar{\zeta}(r) + \zeta'(r, \phi)$, where $\bar{\zeta}(r)$ is an axisymmetric vorticity ring defined by

$$\bar{\zeta}(r, 0) = \begin{cases} \zeta_1 & 0 \leq r \leq r_1 \\ \zeta_1 S\left(\frac{r-r_1}{r_2-r_1}\right) + \zeta_2 S\left(\frac{r_2-r}{r_2-r_1}\right) & r_1 \leq r \leq r_2 \\ \zeta_2 & r_2 \leq r \leq r_3, \\ \zeta_2 S\left(\frac{r-r_3}{r_4-r_3}\right) + \zeta_3 S\left(\frac{r_4-r}{r_4-r_3}\right) & r_3 \leq r \leq r_4 \\ \zeta_3 & r_4 \leq r \leq \infty \end{cases} \quad (2.22)$$

where ζ_1 , ζ_2 , ζ_3 , r_1 , r_2 , r_3 , and r_4 are constants, and $S(x)$ is the cubic polynomial interpolation function defined previously. The eyewall is defined as the region between r_2 and r_3 . Schubert et al. (1999) defined two parameters to describe these hurricane-like vorticity rings: a ring thickness parameter $\delta = (r_1 + r_2)/(r_3 + r_4)$, and a ring hollowness parameter $\gamma = \zeta_1/\zeta_{\text{av}}$. The relative vorticity and radii used for each of the five experiments is shown in Table 2.1. Each ring is perturbed with a broadband impulse of the form

$$\zeta'(r, \phi, 0) = \zeta_{\text{amp}} \sum_{m=1}^8 \cos(m\phi + \phi_m) \times \begin{cases} 0 & 0 \leq r \leq r_1 \\ S\left(\frac{r_2-r}{r_2-r_1}\right) & r_1 \leq r \leq r_2 \\ 1 & r_2 \leq r \leq r_3, \\ S\left(\frac{r-r_3}{r_4-r_3}\right) & r_3 \leq r \leq r_4 \\ 0 & r_4 \leq r \leq \infty \end{cases} \quad (2.23)$$

where $\zeta_{\text{amp}} = 1.0 \times 10^{-5} \text{ s}^{-1}$ is the amplitude and ϕ_m the phase of azimuthal wavenumber m . For this set of experiments, the phase angles ϕ_m were chosen to be random numbers in the range $0 \leq \phi_m \leq 2\pi$. In real hurricanes, such asymmetries are expected to develop from a wide spectrum of background turbulent and convective motions.

Table 2.1: Unstable vorticity ring parameters: ζ values are in 10^{-3} s^{-1} and r values are in km.

Exp.	ζ_1	ζ_2	r_1	r_2	r_3	r_4	δ	γ
A	0.8	2.7	22	26	38	42	0.60	0.40
B	0.0	3.1	22	26	38	42	0.60	0.00
C	0.0	4.6	28	32	38	42	0.75	0.00
D	0.0	7.2	32	36	38	42	0.85	0.00
E	0.2	6.7	32	36	38	42	0.85	0.10

Two simulations from Table 2.1 are illustrated. The first (Exp. A) is a thick, filled ring, while the second (Exp. D) is a thin, hollow ring. According to Schubert et al. (1999), as the rings become thicker and filled, disturbance growth rates become smaller and at lower wavenumber. As the rings become very thin and hollow, they rapidly break down and sometimes evolve into persistent mesovortices (Kossin and Schubert 2001). Experiment A is shown in Fig. 2.9. At $t = 13.0$ h (middle left panel), the ring is breaking down at azimuthal wavenumber $m = 4$ giving the appearance of a polygonal eyewall with straight line segments. The breaking of the inner PV wave has allowed vorticity to be pooled into four regions. In the effective diffusivity plot (middle right panel), there are two distinct radial intervals of mixing, separated by a rather strong, thin barrier region. The inner mixing region is approximately coincident with the vorticity pools, while the outer mixing region exists just outside the vorticity core. These two mixing regions are due to the inner and outer counterpropagating, breaking, PV waves. The waves are phase-locked and helping each other grow, resulting in radial air movement and mixing. During this time the passive tracer field becomes relatively well-mixed in the radial intervals of the PV wave activity, however the initial gradient is maintained in the barrier region in between (not shown). Progressing to $t = 41.0$ h, the magnitude of the mixing due to the wave activity is smaller, but the barrier region still exists.

The breakdown of the Experiment D ring is shown in Fig. 2.10. The disturbance growth rates are larger in this case, allowing the ring to break down much faster. Multiple

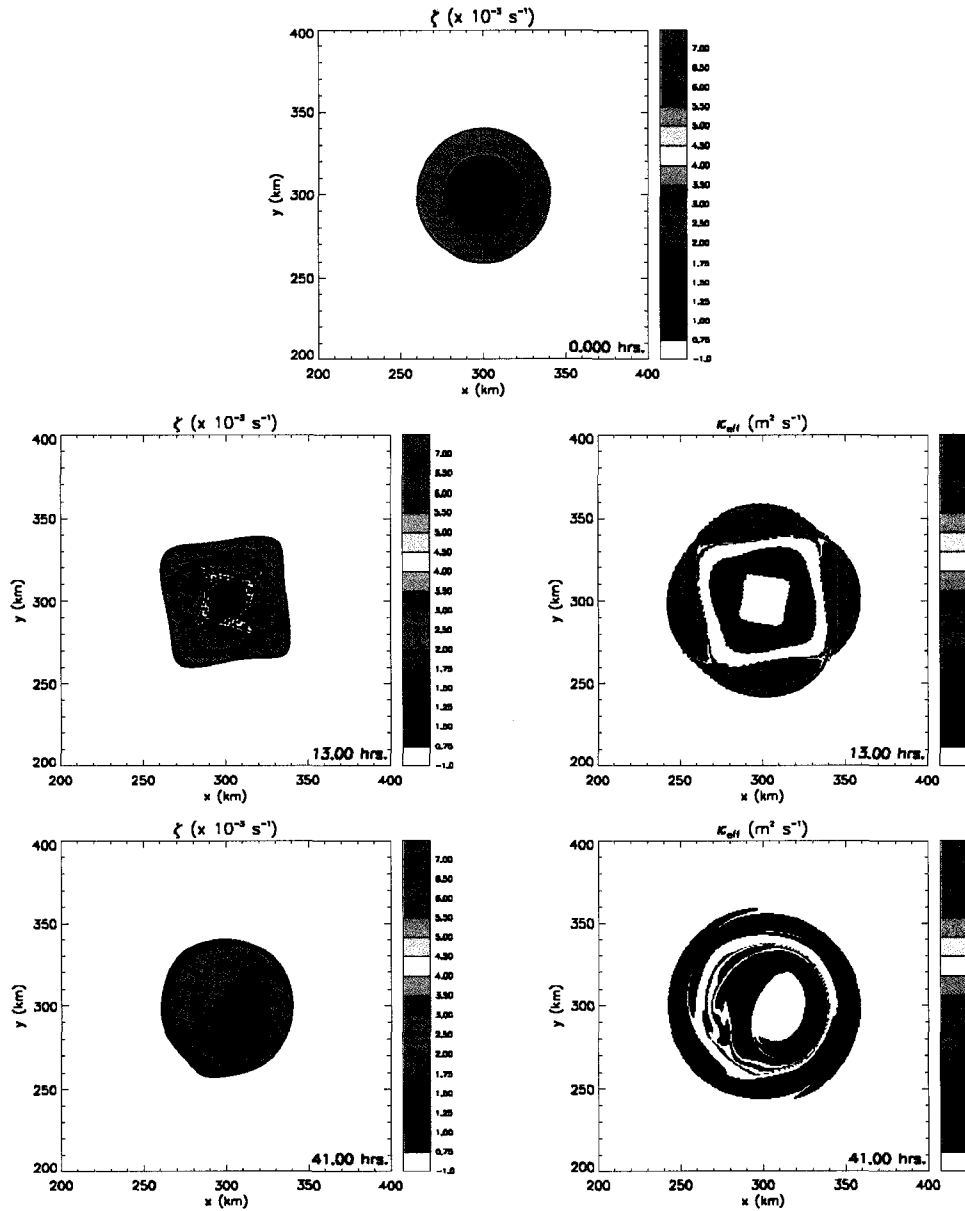


Figure 2.9: The initial vorticity field (top panel) and side-by-side panels (at 13 h and 41 h) of relative vorticity and effective diffusivity κ_{eff} for a prototypical thick, filled unstable vorticity ring (Experiment A of Table 1).

mesovortices initially form (middle left panel). During the formation stage, these mesovortices and associated filamentary structures are strong mixing regions (middle right panel of Fig. 2.10). The mesovortices persist for a very long time, and at $t = 20.0$ h there are

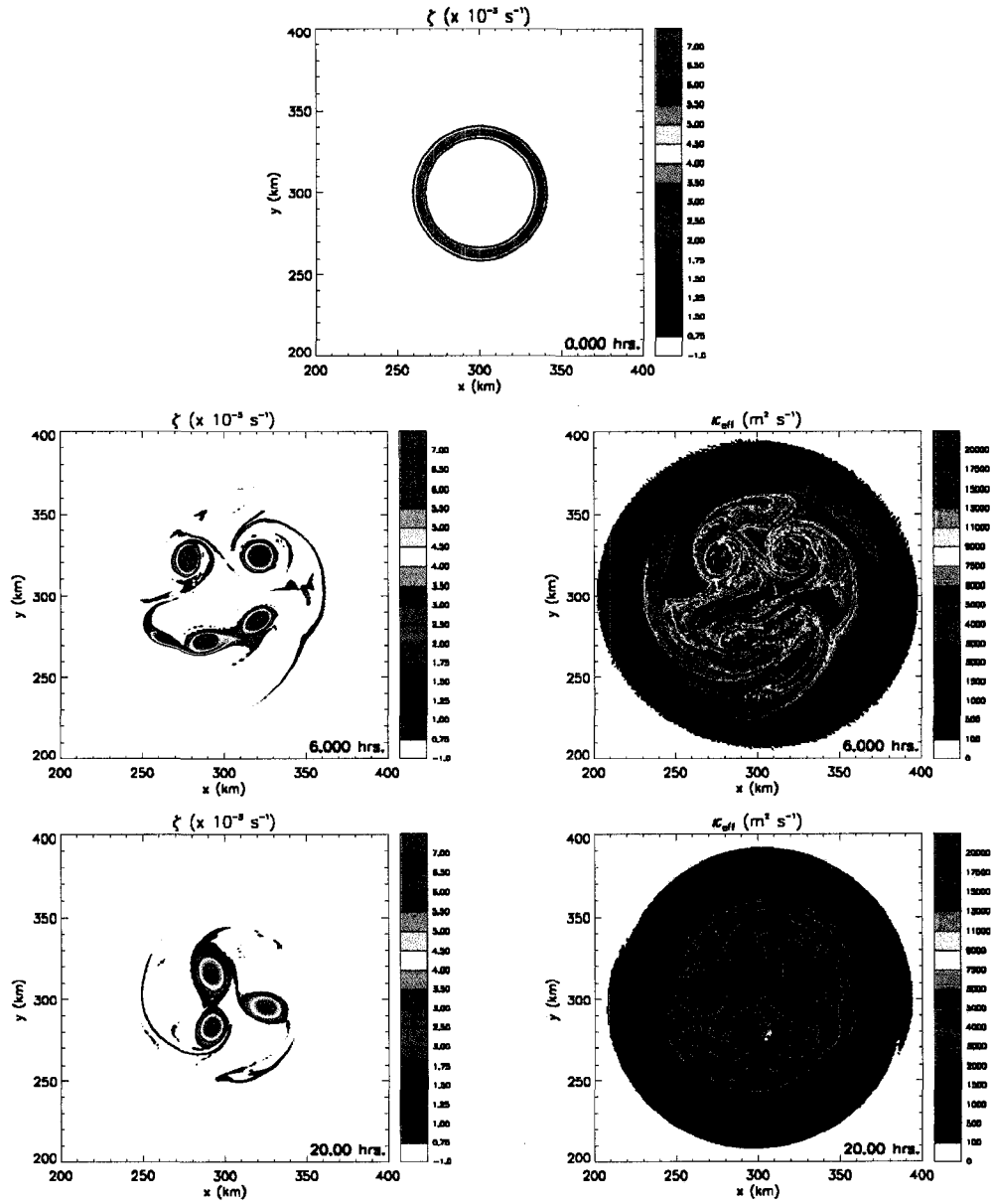


Figure 2.10: The initial vorticity field (top panel) and side-by-side panels (at 6 h and 20 h) of relative vorticity and effective diffusivity κ_{eff} for a prototypical thin, hollow unstable vorticity ring (Experiment D of Table 1).

three mesovortices left after some mergers have occurred. At this time the mesovortices act as transport barrier regions. Based on these results, in conjunction with the binary vortex interaction and Rankine-like vortex in a turbulent vorticity field, we find that barotropic

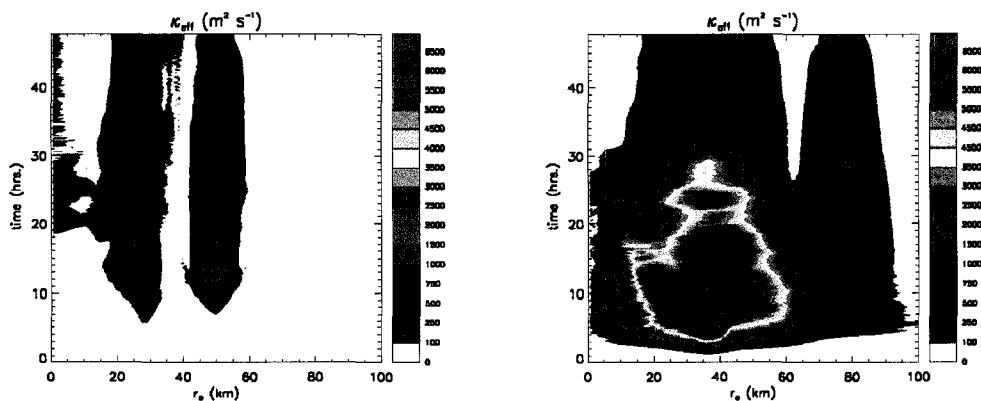


Figure 2.11: Hovmöller plots depicting the temporal evolution of $\kappa_{\text{eff}}(r_e, t)$ for the A ring (left) and the D ring (right).

geophysical vortices of all horizontal scales tend to act as partial barrier regions when they are long-lived.

To further illustrate the two regimes of internal mixing, Hovmöller plots of $\kappa_{\text{eff}}(r_e, t)$ are shown in Fig. 2.11 for Experiments A and D. For the A ring (left panel), there exists two distinct mixing regions at $20 \text{ km} \leq r_e \leq 30 \text{ km}$ and $40 \text{ km} \leq r_e \leq 55 \text{ km}$. These mixing regions are associated with the counterpropagating PV waves evident in the middle panels of Fig. 2.9. For the D ring, in which a rapid breakdown occurs, the entire hurricane inner-core ($10 \text{ km} \leq r_e \leq 60 \text{ km}$) is a chaotic mixing region. These two types of mixing regimes are further clarified in Fig. 2.12, which shows the time-averaged effective diffusivity κ_{eff} for all five rings. For the rings with slower growth rates (A and B), there exist two peaks in $\kappa_{\text{eff}}(r_e)$ coincident with inner and outer PV wave activity. For the rings with faster growth rates (C, D, and E), the entire inner core is a chaotic mixing region. During the evolution of each ring, the radius of maximum wind varies, but it is generally confined to radii between 30 km and 40 km. Thus, for thick, filled rings the hurricane tangential jet acts as a partial barrier region for $t \leq 48 \text{ h}$, while for thin, hollow rings, the hurricane tangential jet breaks down and chaotic mixing in the entire inner core ensues. The implication of this result for real hurricanes is that if the eyewall is very thick, passive tracers will not easily be mixed

across the eyewall during barotropic instability, but may be mixed between the eye-eyewall and environment-eyewall by the inner and outer breaking PV waves, respectively. If, on the other hand, the eyewall is thin, as in rapidly intensifying hurricanes (Kossin and Eastin 2001), passive tracers can be mixed across the eye, eyewall and environment, and at a much faster rate. Assuming hurricanes have a maximum of equivalent potential temperature (θ_e) at low levels in the eye, our results indicate that the inner, breaking, PV wave will mix air parcels with high θ_e into the eyewall, supporting the hurricane superintensity mechanism (Persing and Montgomery 2003). This mixing will be more rapid for the breakdown of thin rings.

The mixing regime in which the tangential jet acts as a partial barrier is analogous to the results of Bowman and Chen (1994), who found that air poleward of a barotropically unstable stratospheric jet remained nearly perfectly separated from midlatitude air. Our hurricane results are again analogous to planetary-scale mixing, and it appears that under certain conditions azimuthal jets in hurricanes can become asymmetric but still remain partial (but leaky) barriers to radial mixing.

2.6 Sensitivity tests

In order to assess the robustness of effective diffusivity as a diagnostic of mixing properties of a flow, a number of sensitivity tests were conducted: (i) tracer diffusion coefficient, (ii) initial tracer distribution, and (iii) the accuracy of the discrete approximation to the diagnostic (2.12).

2.6.1 *Tracer diffusion coefficient*

In the area-based coordinate system, it is expected that the effective diffusivity will increase with increasing tracer diffusivity κ . As material lines are stretched and folded there exists more interface for diffusion to produce irreversible mixing, and if the diffusion coefficient is larger, the level of mixing should be larger as area can diffuse faster between

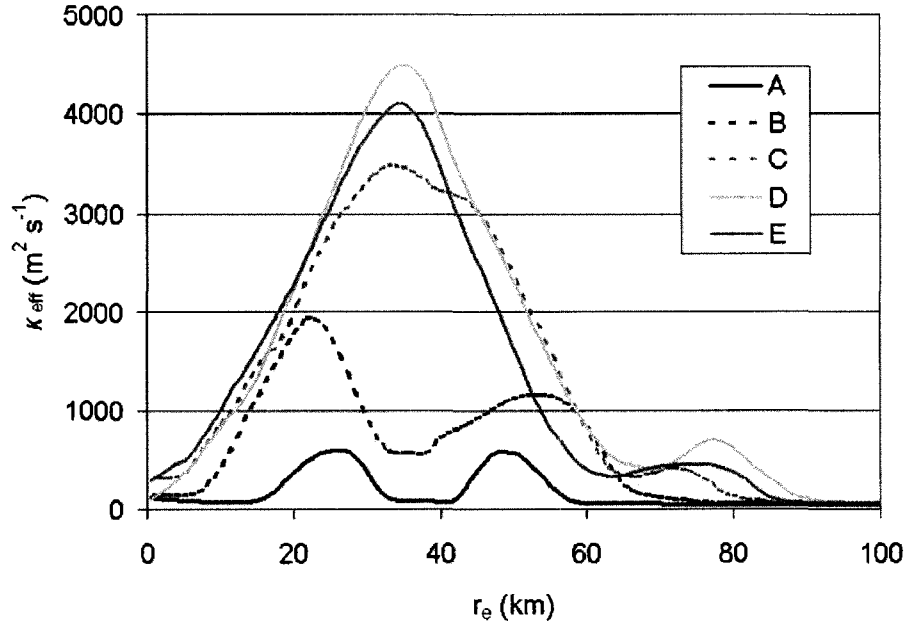


Figure 2.12: Time-averaged (0-48 h) effective diffusivity for all unstable rings versus equivalent radius. The radius of maximum wind varies during the evolution but generally lies in the region between 30–40 km.

tracer contours. This is clearly illustrated in Fig. 2.13 for the C unstable ring experiment. This experiment is similar to the Experiment D in that a large radial segment becomes a chaotic mixing region (Fig. 2.11, right panel). Four different values of the tracer diffusivity are chosen: $\kappa = 50, 25, 10, \text{ and } 0.1 \text{ m}^2 \text{ s}^{-1}$. The larger tracer diffusivities clearly have larger effective diffusivities, and the radial character of the profiles is broadly preserved for each case. For example, the $\kappa = 50, 25, \text{ and } 10 \text{ m}^2 \text{ s}^{-1}$ cases are able to capture the peak effective diffusivity at $r_e = 30 \text{ km}$. The $\kappa = 0.1 \text{ m}^2 \text{ s}^{-1}$ is not seen on the figure because the peak effective diffusivity associated with it is only $\kappa_{\text{eff}} = 20 \text{ m}^2 \text{ s}^{-1}$, too low to be visible with the plot scaling. The same plot is shown in Fig. 2.14 for $\Lambda_e(r_e, t)$. Note that $\Lambda_e(r_e, t)$ is not very sensitive to varying κ , and as stated earlier, is the best measure of chaotic advection.

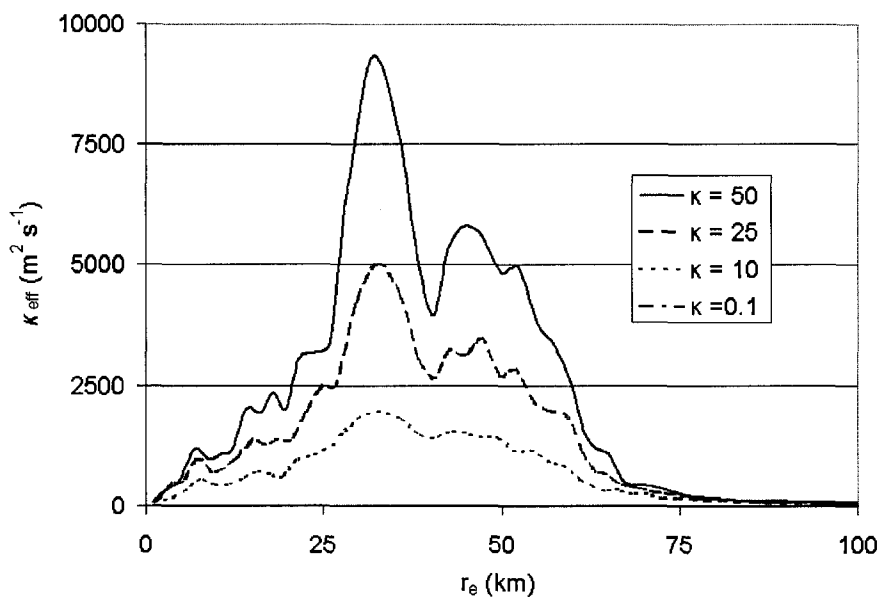


Figure 2.13: Effective diffusivity versus equivalent radius for varying values of the tracer diffusivity κ (units of $\text{m}^2 \text{s}^{-1}$) for the C unstable ring experiment at $t = 6.3$ h.

2.6.2 Initial tracer distribution

Since effective diffusivity maps out the mixing properties of a flow, it is supposed to be mostly insensitive to the initial tracer field, provided it is monotonic and well behaved. In order to illustrate this, plots of effective diffusivity versus equivalent radius are shown in Fig. 2.15 for three different initial axisymmetric tracer fields: a Gaussian distribution with maximum value of 1000 (used in the elliptical vorticity field, binary vortex interaction, and Rankine-like vortex in a turbulent vorticity field), and linearly decreasing distributions with maximum values of 1000 (used in the unstable vorticity ring experiments) and 5000. Each of these curves has different dC/dr_e (or dC/dA), used in the denominator of the effective diffusivity diagnostic. The κ_{eff} profiles are almost identical for the two linear cases, and only a slight variation is found for the Gaussian case. The Gaussian case departs from the linear cases slightly at small radii. The likely reason for this is that the slope of the tangent line (dC/dr_e) is very small there, causing the effective diffusivity diagnostic to be

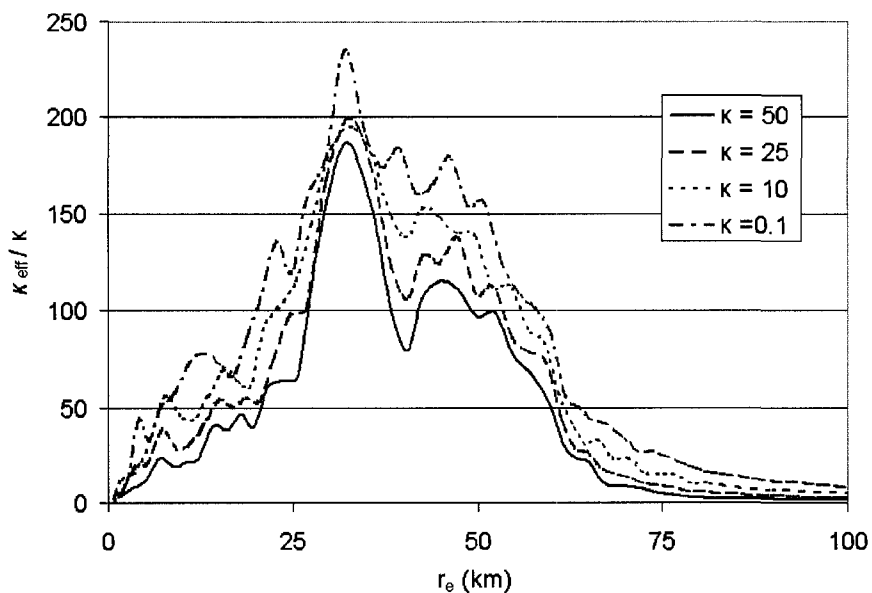


Figure 2.14: Normalized effective diffusivity $\Lambda_e(r_e, t) = \kappa_{\text{eff}}(r_e, t)/\kappa$. versus equivalent radius for varying values of the tracer diffusivity κ (units of $\text{m}^2 \text{s}^{-1}$) for the C unstable ring experiment at $t = 6.3$ h.

unrealistically distorted. We feel that the linearly decreasing initial tracer profile is the best to use because it guarantees constancy of the initial dC/dA in the domain. Overall, effective diffusivity is insensitive to the initial tracer profile and is therefore a robust diagnostic for mixing properties of a two-dimensional aperiodic flow.

2.6.3 Number of area points

Sensitivity tests were performed using varying numbers of area points in the discrete approximation to the effective diffusivity diagnostic (2.12). To illustrate the sensitivity to the discrete approximation, the effective diffusivity versus equivalent radius is shown in Fig. 2.16 for the C unstable ring with $n_A = 50$, $n_A = 200$ (used in all the experiments in this paper), and $n_A = 1000$ points. All three curves produce peaks near $r_e = 30$ km, but only the $n_A = 200$ and $n_A = 1000$ curves capture the peak value of $\kappa_{\text{eff}} = 5000 \text{ m}^2 \text{ s}^{-1}$ at $r_e \approx 35$ km and the dip at $r_e = 40$ km. The conclusion is that $n_A = 50$ is not sufficient to

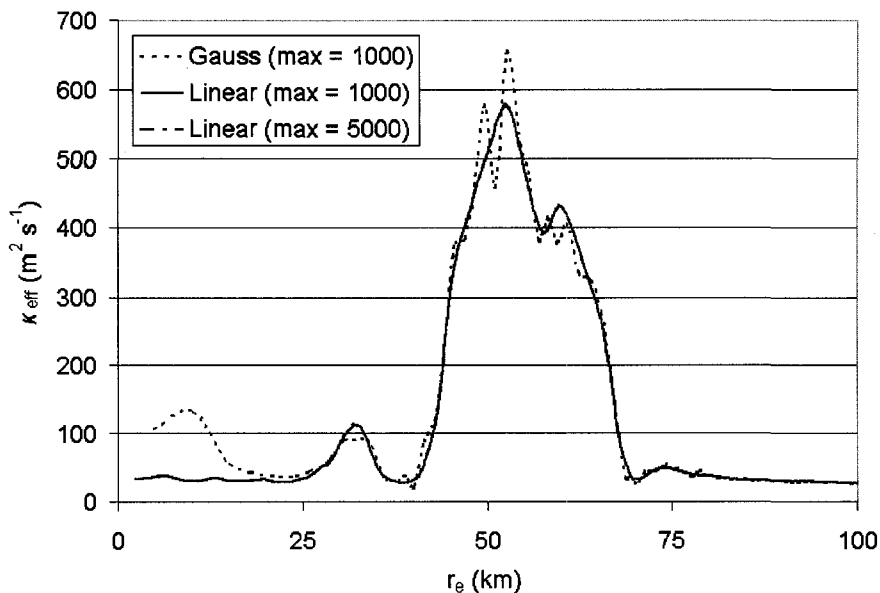


Figure 2.15: Sensitivity of effective diffusivity to the initial tracer field. Three curves are shown: Gaussian profile with maximum value of 1000 and linearly decreasing profiles with maximum values of 1000 and 5000.

resolve the mixing properties of the inner-core, but little is gained in going from $n_A = 200$ to $n_A = 1000$. Thus, our choice of $n_A = 200$ is sufficient to resolve the effective diffusivity variability. Although the $n_A = 1000$ curve does produce more variability, it is not known whether the highly oscillatory nature of the curve is real or an oversampling issue.

2.7 Conclusions

The two-dimensional mixing properties of aperiodic evolving hurricane-like vortical flows were quantified using the effective diffusivity diagnostic on the output of numerical simulations with a nondivergent barotropic model. The location and magnitude of both chaotic mixing and partial barrier regions were identified, yielding insight into how passive tracers are asymmetrically mixed at low levels of hurricanes. The primary finding is that breaking PV waves, resulting from either axisymmetrization or dynamic instability, are quite effective at mixing passive tracers over large horizontal distances in hurricanes.

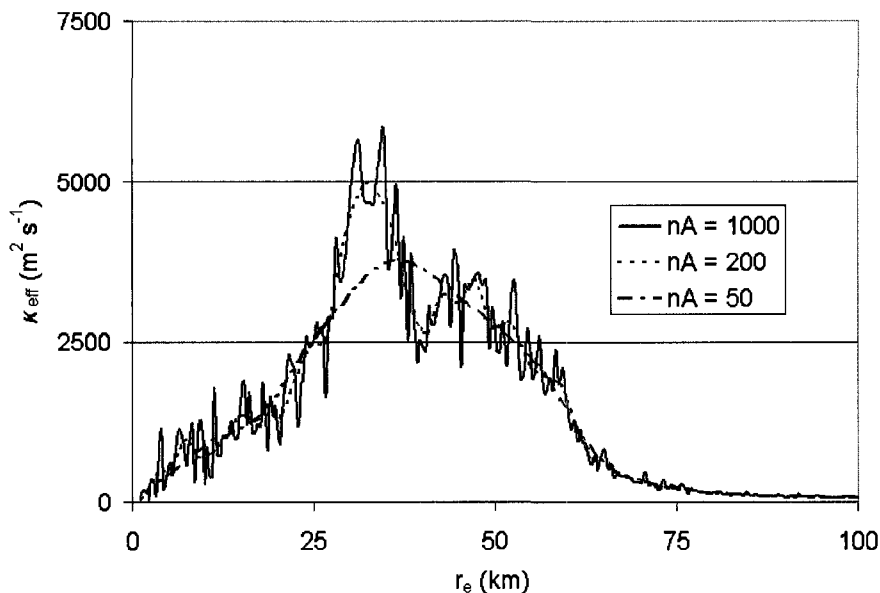


Figure 2.16: Sensitivity of effective diffusivity to the number of area points: 50, 200, and 1000. The case shown is the C unstable ring at $t = 6.3$ h.

For monotonic vortices, the wave breaking and mixing was confined to a 20–30 km wide surf zone outside the radius of maximum wind, while the vortex core remained a barrier. In these cases, the eye is a containment vessel and eye air is not easily mixed with the environment. For unstable rings, which are analogous to strong or intensifying hurricanes, both the inner and outer counterpropagating PV waves break causing two mixing regions: one between the eye and eyewall and one between the eyewall and local environment. In the case of thick rings, the disturbance exponential growth rates are small and a long-lived asymmetric partial barrier region may exist between the two breaking waves, coincident with the tangential jet. In the case of thin rings that are very dynamically unstable, the rapid breakdown created a strong chaotic mixing region over the entire hurricane inner-core (eye, eyewall, and local environment). In this case, passive tracers may be horizontally mixed over large radial distances (approximately 60–80 km in our experiments). Since observations show a maximum of θ_e at low levels in the eye (Eastin et al. 2002), our results indicate that

the inner, breaking PV wave would be quite effective at mixing air parcels with high θ_e into the eyewall, supporting the hurricane superintensity mechanism (Persing and Montgomery 2003). The hurricane eye remains a partial barrier during barotropic instability because the inner, breaking PV wave generally does not penetrate all the way into the center. Thus, it is possible that the highest θ_e air may never be mixed into the eyewall, limiting the level of superintensity.

Both primary and secondary azimuthal wind maxima were identified as partial barriers in our simulations. These jets act as mixing barriers because they are located near regions of strong radial PV gradients (cf. McIntyre 1989). A surprising result is that the primary jet barrier region can be maintained for long times during barotropic instability. Additionally, it can maintain itself as a partial barrier when it is deformed asymmetrically to a polygon with straight line segments. Therefore in this simple framework, the hurricane primary jet appears to be a *robust transport barrier* for both dynamically stable and unstable vortices, provided the latter vortices are characterized by thick annular vorticity structures.

The present work could be extended in a number of ways. Effective diffusivity could be used as a diagnostic for transport and mixing in axisymmetric hurricane models (Rotunno and Emanuel 1987; Hausman et al. 2006). Of particular interest would be examining the vertical structure of mixing processes between the eye and eyewall. Effective diffusivity can also be used as a diagnostic for three dimensional hurricane simulations, provided the evolution is approximately nondivergent. In this case, the area coordinate becomes a volume coordinate (Appendix A), which can be mapped to equivalent heights to assess the vertical structure of mixing. For the case of either two or three dimensional divergent flow, the area coordinate becomes a mass coordinate (Nakamura 1995). Further theoretical work would need to be done to obtain a useful mixing diagnostic for these flows, but its utility would extend to the output of more complex three dimensional full-physics models. The diagnostic could also be used to understand aspects of transport and mixing of water vapor

in the frictional boundary layer of hurricanes.

Chapter 3

LIFECYCLES OF HURRICANE-LIKE POTENTIAL VORTICITY RINGS

3.1 Abstract

The asymmetric dynamics of potential vorticity (PV) mixing in the hurricane inner-core are further advanced by examining the end states that result from the unforced evolution of hurricane-like vorticity rings in a nondivergent barotropic model. The results from a sequence of 170 numerical simulations are summarized. The sequence covers a two-dimensional parameter space, with the first parameter defining the hollowness of the vortex (i.e., the ratio of eye to inner-core relative vorticity) and the second parameter defining the thickness of the ring (i.e., the ratio of the inner and outer radii of the ring). In approximately one half of the cases, the ring becomes barotropically unstable, and there ensues a vigorous vorticity mixing episode between the eye and eyewall. The output of the barotropic model is used to: (i) verify that the nonlinear model approximately replicates the linear theory of fastest growing azimuthal mode in the early phase of the evolution, and (ii) characterize the end states (defined at $t = 48$ h) that result from the nonlinear chaotic vorticity advection and mixing. It is found that the linear stability theory is a good guide to the observed fastest growing exponential mode in the numerical model. Two additional features are observed in the numerical model results. The first is an azimuthal wavenumber-2 deformation of the PV ring that occurs for moderately thick, nearly filled rings. The second is an algebraically growing wavenumber-1 instability (not present in the linear theory due to the assumed solution) that is observed as a wobbling eye (or the trochoidal oscillation for a moving vortex)

for thick rings that are stable to all exponentially growing instabilities. Most end states are found to be monopoles. For very hollow and thin rings, persistent mesovortices may exist for more than fifteen hours before merging to a monopole. For thicker rings, the relaxation to a monopole takes longer (between 48 and 72 h). For moderately thick rings with nearly filled cores, the most likely end state is an elliptical eyewall. In this nondivergent barotropic context, both the minimum central pressure and maximum tangential velocity simultaneously decrease over 48 h during all PV mixing events. Thus care must be taken when using empirical pressure-wind relationships that assume an inverse relationship during PV mixing events.

3.2 Introduction

Diabatic heating due to moist convection in the eyewall of a hurricane produces a hollow tower of potential vorticity (PV) in the lower to mid-troposphere (Möller and Smith 1994; Yau et al. 2004). The sign reversal of the radial gradient of PV sets the stage for dynamic instability. If the hollow tower is thin enough, it may break down, causing PV to be mixed into the eye. During these PV mixing episodes, the existence of polygonal eyewalls with straight line segments, asymmetric eye contraction, and eye mesovortices have been documented in numerical models, laboratory experiments, and observational studies (Schubert et al. 1999; Kossin and Schubert 2001; Montgomery et al. 2002; Kossin et al. 2002; Kossin and Schubert 2004). Eye mesovortices are often visible as vortical cloud swirls in the eyes of strong hurricanes (see Fig. 3.1 for an example). Although the Rayleigh necessary condition for dynamic instability is satisfied for all rings, not all rings are unstable. In particular, thick rings, which may be analogous to annular hurricanes (Knaff et al. 2003), are usually stable to exponentially growing perturbations.

These PV mixing episodes are thought to be an important internal mechanism governing hurricane intensity change on short time scales (less than 48 h) because, by inversion, PV may be partitioned into both inertial and static stability. From another perspective, mixing

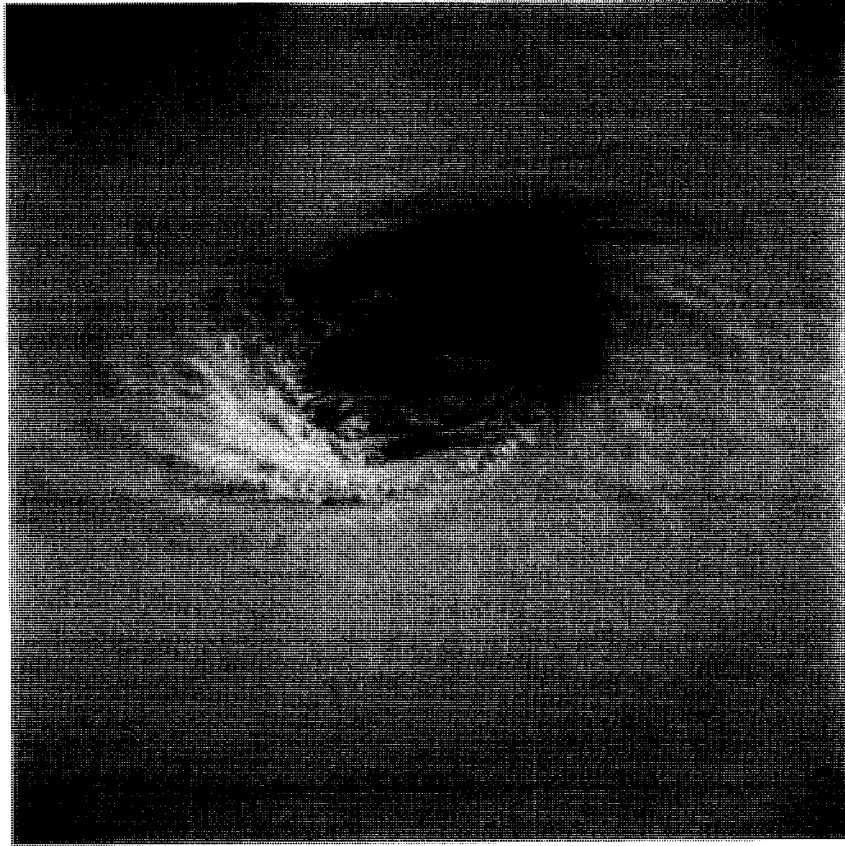


Figure 3.1: Vortical swirls observed in the eye of Super Typhoon Yuri (1991). (Credit: Image Science and Analysis Laboratory, NASA-Johnson Space Center)

of PV from the eyewall into the eye changes the azimuthal mean tangential wind profile inside the radius of maximum wind (RMW) from U-shaped ($\partial^2 v / \partial r^2 > 0$) to Rankine-like ($\partial^2 v / \partial r^2 \approx 0$). While it may be expected that the maximum tangential velocity would decrease as the PV is radially broadened, the mixing of PV into the eye causes the v^2/r term in the gradient wind equation to become very large, which supports a decrease in central pressure leading to further intensification. This dual nature of PV mixing has recently been studied using a forced barotropic model (Kossin et al. 2006; Rozoff et al. 2008). In addition, eye mesovortices that sometimes form are thought to be important factors governing intensity change because they may serve as efficient transporters of warm and moist air at low levels of the eye to the eyewall (Persing and Montgomery 2003; Montgomery et al.

2006a; Cram et al. 2007) allowing the hurricane to exceed its axisymmetric energetically based maximum potential intensity (Emanuel 1986, 1988).

In order to obtain insight into the basic dynamics of this problem, Schubert et al. (1999) (hereafter S99) performed a linear stability analysis for hurricane-like rings of enhanced vorticity. By defining a ring thickness parameter (ratio of the inner and outer radii) and a ring hollowness parameter (ratio of the eye to the inner-core vorticity), they were able to express the exponential growth rates of disturbances of various azimuthal wavenumbers in this thickness-hollowness space. In the aggregate, they found that the fastest growth rates existed for thin, hollow rings, while slower growth rates existed for thick, filled rings. Very thick rings were found to be stable to exponentially growing perturbations of all azimuthal wavenumbers. The nonlinear evolution of a prototypical hurricane-like vorticity ring was examined to study asymmetric details of the vorticity mixing episode. In the early phase, a polygonal eyewall (multiple straight line segments) was observed, and later, as high PV fluid was mixed from the eyewall to the eye, asymmetric eye contraction was illustrated. This confirmed that polygonal eyewalls can be attributed solely to slow vorticity dynamics, rather than transient inertia-gravity wave interference patterns (Lewis and Hawkins 1982). After approximately two days, the initial vorticity field was redistributed to an end state of an axisymmetric monopole. In general, it is not possible to accurately predict these end states analytically (i.e., without numerically simulating the nonlinear advection); however, the use of vortex minimum enstrophy and maximum entropy approaches have yielded some useful insight (S99 sections 5 and 6).

In the present work, we examine the complete lifecycles of 170 different PV rings in a nondivergent barotropic model framework. The model experiments sample the two dimensional parameter space using 10 points of varying hollowness of the core (hollow to nearly filled) and 17 points of varying thickness of the ring (thick to thin). These rings are indicative of vorticity structures present in a wide spectrum of real hurricanes. In the initial linear wave growth phase, the nondivergent barotropic model results are compared to the

S99 linear theory for the most unstable azimuthal mode. The unforced evolution is then allowed to progress into its fully nonlinear advective regime. The end states (defined at $t = 48$ h) are assessed and characterized for each ring. Azimuthal mean diagnostics are also presented showing the evolution of the radial pressure and tangential wind profiles for each ring to assess the relationship between PV mixing events and hurricane intensity change. Provided the axisymmetric potential vorticity field can be ascertained, these results can be used as a gauge for understanding the PV redistribution process in real hurricanes.

The outline of this chapter is as follows. In section 3.3, the linear stability analysis of S99 is briefly reviewed. The pseudospectral barotropic model and initial conditions are described in section 3.4. A comparison of the fastest growing azimuthal mode observed in the numerical model to the linear stability analysis is given in section 3.5. The end states of the unstable vortices are characterized and discussed in section 3.6. A discussion of the relationship between PV mixing and hurricane intensity change is presented in section 3.7. Finally, a summary of the results is given in section 3.8.

3.3 Review of linear stability analysis

It is well known that the sign reversal in the radial vorticity gradient in hurricanes satisfies the Rayleigh necessary condition for barotropic instability¹. One can view the instability as originating from the interaction of two counterpropagating vortex Rossby (or PV) waves (Guinn and Schubert 1993; Montgomery and Kallenbach 1997). A Rossby wave on the inner edge of the annulus will prograde relative to the mean flow, and a Rossby wave on the outer edge will retrograde relative to the mean flow. If these waves phase-lock (i.e., have the same angular velocity), it is possible for the whole wave pattern to amplify.

The linear stability analysis of initially hollow vorticity structures was performed by S99 (their section 2). A brief review of that work is presented here. First, the discrete vor-

¹ In real hurricanes, where vertical shear and baroclinity is nontrivial, we expect the instability to be a combined barotropic-baroclinic one. See Montgomery and Shapiro (1995) for a discussion of the Charney-Stern and Fjortoft theorems applicable to baroclinic vortices

ticity model is defined as three separate regions: eye ($\xi_a + \xi_b$), eyewall (ξ_b), and environment (Michalke and Timme 1967; Vladimirov and Tarasov 1980; Terwey and Montgomery 2002):

$$\bar{\zeta}(r) = \begin{cases} \xi_a + \xi_b & \text{if } 0 \leq r < r_a \text{ (eye)} \\ \xi_b & \text{if } r_a < r < r_b \text{ (eyewall)} \\ 0 & \text{if } r_b < r < \infty \text{ (far-field)} \end{cases} . \quad (3.1)$$

Small amplitude perturbations to this basic state vorticity are governed by the linearized nondivergent barotropic vorticity equation:

$$\left(\frac{\partial}{\partial t} + \bar{\omega} \frac{\partial}{\partial \phi} \right) \nabla^2 \psi' - \frac{\partial \psi'}{r \partial \phi} \frac{d\bar{\zeta}}{dr} = 0. \quad (3.2)$$

Here, $\bar{\omega}(r) = \bar{v}/r$ is the basic state angular velocity, ψ' is the perturbation streamfunction from which the nondivergent velocity can be obtained (i.e., $u' = -\partial\psi'/r\partial\phi$ is the perturbation radial velocity and $v' = \partial\psi'/\partial r$ is the perturbation azimuthal velocity), and $\zeta' = \nabla^2\psi'$ is the perturbation relative vorticity. By seeking solutions to (3.2) of the form $\psi'(r, \phi, t) = \hat{\psi}(r)e^{i(m\phi - \nu t)}$ (where m is the azimuthal wavenumber and ν is the complex frequency), (3.2) reduces to an ordinary differential equation for the radial structure function $\hat{\psi}(r)$. Using the $\hat{\psi}(r)$ solution in conjunction with appropriate boundary conditions, a mathematical description of the traveling vortex Rossby waves at the two vorticity jumps is obtained, along with their mutual interaction. The eigenvalue relation can be written in a physically revealing form by introducing two vortex parameters, $\delta = r_a/r_b$ (where r_a and r_b are the radii of the vorticity jumps from the eye to the eyewall and from the eyewall to the environment, respectively) and $\gamma = (\xi_a + \xi_b)/\zeta_{av}$ (where $\zeta_{av} = \xi_a\delta^2 + \xi_b$ is the average vorticity over the entire hurricane inner-core). Then, the dimensionless complex frequency ν/ζ_{av} can be expressed solely in terms of the azimuthal wavenumber m , the ring thickness

parameter δ , and the ring hollowness parameter γ as

$$\frac{\nu}{\zeta_{av}} = \frac{1}{4} \left\{ m + (m-1)\gamma \pm \left[\left(m - (m-1)\gamma - 2 \left(\frac{1-\gamma\delta^2}{1-\delta^2} \right) \right)^2 + 4 \left(\frac{1-\gamma\delta^2}{1-\delta^2} \right) \left(\gamma - \frac{1-\gamma\delta^2}{1-\delta^2} \right) \delta^{2m} \right]^{\frac{1}{2}} \right\}. \quad (3.3)$$

Exponentially growing or decaying modes occur when the imaginary part of the frequency, ν_i , is nonzero, i.e., when the term in brackets is negative. Isolines of the dimensionless growth rate ν_i/ζ_{av} can then be drawn in the (δ, γ) -parameter space for each azimuthal wavenumber m . This set of diagrams can be collapsed into a single summary diagram by choosing the most rapidly growing wave for each point in the (δ, γ) -parameter space. This summary diagram is shown in Fig. 3.2. As an example of interpreting this diagram, consider a vortex defined by $(\delta, \gamma) = (0.7, 0.3)$. According to Fig. 3.2, the most unstable mode is $m = 4$, and this mode grows at the rate $\nu_i/\zeta_{av} \approx 0.15$. For a hurricane-like vorticity of $\zeta_{av} = 2.0 \times 10^{-3} \text{ s}^{-1}$, this corresponds to an e -folding time of 0.93 h.

The rings considered in S99 were stable to exponentially growing modes of wavenumber $m = 1$ and $m = 2$. As shown by Terwey and Montgomery (2002), there does exist an exponentially growing $m = 2$ mode in the discrete model; however, a necessary condition for it is that $|\xi_b| < |\xi_a|$ (the eye vorticity is negative). This was absent from S99 because $\gamma > 0$ for their vortices. In the analagous continuous model (6) with smooth transitions instead of vorticity jumps, exponentially growing $m = 2$ modes are also possible (Schubert et al. 1999; Reasor et al. 2000).

Both the discrete and continuous models are stable to exponentially growing wavenumber $m = 1$ modes. However, an algebraic $m = 1$ instability that grows at $t^{1/2}$ (Smith and Rosenbluth 1990) exists. The only requirement for this instability is a local maximum in angular velocity (Nolan and Montgomery 2000), which occurs for every vortex considered in S99 and here. However (as will be shown) the $m = 1$ algebraically growing mode is only visible in rings that are stable to all faster exponentially growing modes (thick and filled rings). The $m = 1$ instability is visible as a growing wobble of the eye (Nolan et al. 2001).

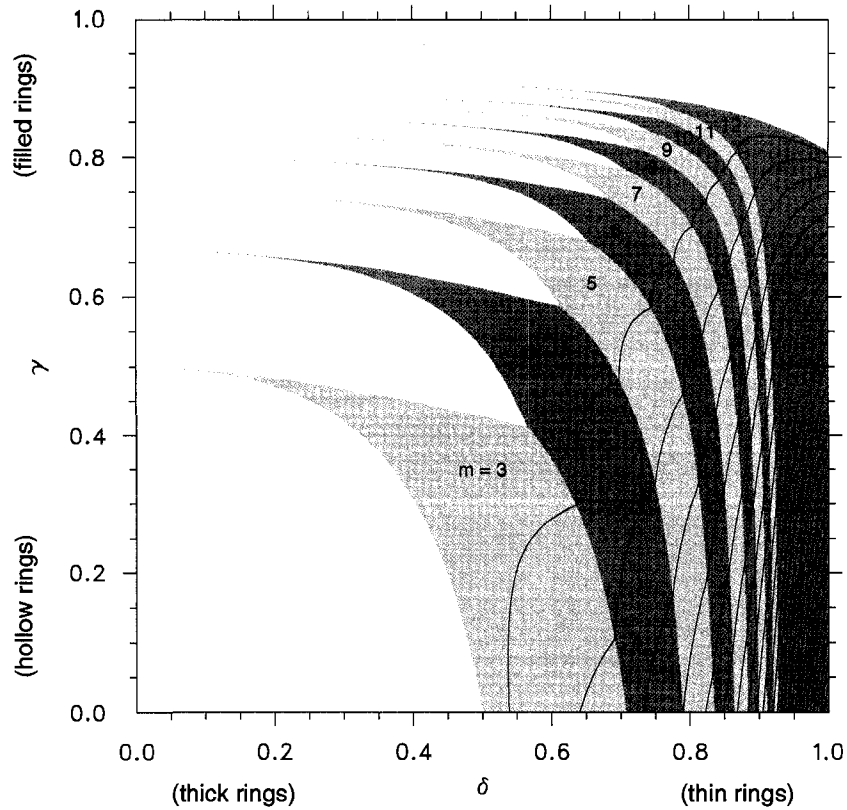


Figure 3.2: Isolines of the maximum dimensionless growth rate ν_i/ζ_{av} for azimuthal wavenumbers $m = 3, 4, \dots, 12$. Contours range from 0.1 to 2.7 (lower right), with an interval of 0.1. The shaded regions indicate the wavenumber of the maximum growth rate at each δ (abscissa) and γ (ordinate) point.

The S99 linear analysis was generalized by Nolan and Montgomery (2002) to three-dimensional idealized hurricane-like vortices. Broadly, they found that the unstable modes were close analogs of their barotropic counterparts.

3.4 Pseudospectral model experiments

A pseudospectral nondivergent barotropic model is used for all the simulations. The model is based on one prognostic equation for the relative vorticity and a diagnostic equation for the streamfunction, from which the winds are obtained ($u = -\partial\psi/\partial y$ and $v = \partial\psi/\partial x$),

i.e.,

$$\frac{\partial \zeta}{\partial t} + \frac{\partial(\psi, \zeta)}{\partial(x, y)} = \nu \nabla^2 \zeta, \quad (3.4)$$

$$\zeta = \nabla^2 \psi, \quad (3.5)$$

where ν is the kinematic viscosity. The initial condition consists of an axisymmetric vorticity ring defined by

$$\bar{\zeta}(r, 0) = \begin{cases} \zeta_1 & 0 \leq r \leq r_1 \\ \zeta_1 S\left(\frac{r-r_1}{r_2-r_1}\right) + \zeta_2 S\left(\frac{r_2-r}{r_2-r_1}\right) & r_1 \leq r \leq r_2 \\ \zeta_2 & r_2 \leq r \leq r_3, \\ \zeta_2 S\left(\frac{r-r_3}{r_4-r_3}\right) + \zeta_3 S\left(\frac{r_4-r}{r_4-r_3}\right) & r_3 \leq r \leq r_4 \\ \zeta_3 & r_4 \leq r \leq \infty \end{cases} \quad (3.6)$$

where $\zeta_1, \zeta_2, \zeta_3, r_1, r_2, r_3,$ and r_4 are constants, and $S(s) = 1 - 3s^2 + 2s^3$ is a cubic Hermite shape function that provides smooth transition zones. The eyewall is defined as the region between r_2 and r_3 , and the transition zones are defined as the regions between r_1 and r_2 , and r_3 and r_4 . In order to relate the smooth continuous model (3.6) to the discrete model (3.1), the midpoints of the smooth transition zones are used to compute the thickness parameter, so that $\delta = (r_1 + r_2)/(r_3 + r_4)$.

To initiate the instability process, a broadband perturbation (impulse) was added to the basic state vorticity (3.6) of the form

$$\zeta'(r, \phi, 0) = \zeta_{\text{amp}} \sum_{m=1}^{12} \cos(m\phi + \phi_m) \times \begin{cases} 0 & 0 \leq r \leq r_1, \\ S\left(\frac{r_2-r}{r_2-r_1}\right) & r_1 \leq r \leq r_2, \\ 1 & r_2 \leq r \leq r_3, \\ S\left(\frac{r-r_3}{r_4-r_3}\right) & r_3 \leq r \leq r_4, \\ 0 & r_4 \leq r < \infty, \end{cases} \quad (3.7)$$

where $\zeta_{\text{amp}} = 1.0 \times 10^{-5} \text{ s}^{-1}$ is the amplitude and ϕ_m the phase of azimuthal wavenumber m . For this set of experiments, the phase angles ϕ_m were chosen to be random numbers in

the range $0 \leq \phi_m \leq 2\pi$. In real hurricanes, the impulse is expected to develop from a wide spectrum of background turbulent and convective motions.

A sequence of 170 numerical experiments was conducted with the pseudospectral model. The experiments were designed to cover the thickness-hollowness (δ, γ) parameter space described above at regular intervals. The four radii (r_1, r_2, r_3, r_4) were chosen to create 17 distinct values of the thickness parameter $\delta = (r_1 + r_2)/(r_3 + r_4)$ points: [0.05, 0.10, ..., 0.85]. This was accomplished by first setting r_3 and r_4 constant at 38 km and 42 km, respectively. Then, r_1 and r_2 were varied under the constraint that $r_2 - r_1 = r_4 - r_3 = 4$ km to produce the desired values of δ . For example, $r_1 = 0$ km and $r_2 = 4$ km defined the $\delta = 0.05$ point, $r_1 = 2$ km and $r_2 = 6$ km defined the $\delta = 0.10$ point, and so forth. The thinnest ring was defined by $r_1 = 32$ km and $r_2 = 36$ km, corresponding to $\delta = 0.85$ and resulting in a 6 km thick eyewall. The γ points were defined as follows. First, the inner-core average vorticity was set to $\zeta_{av} = 2.0 \times 10^{-3} \text{ s}^{-1}$ (this value corresponds to a hurricane with maximum sustained winds of approximately 40 m s^{-1} for the radii chosen). Then, the eye vorticity ζ_1 was incremented to produce 10 values of $\gamma = \zeta_1/\zeta_{av}$: [0.00, 0.10, ..., 0.90]. The eyewall vorticity ζ_2 was then calculated by $\zeta_2 = \zeta_{av}(1 - \gamma\delta^2)/(1 - \delta^2)$. In each experiment the environmental vorticity ζ_3 was set so that the domain average vorticity would vanish.

The numerical solution was obtained on a $600 \text{ km} \times 600 \text{ km}$ doubly periodic domain using 512×512 equally spaced points. One 48 h simulation was conducted for each of the 170 δ and γ points described above. After dealiasing of the quadratic advection term, 170 Fourier modes were kept yielding an effective resolution of 3.52 km. A standard fourth order Runge-Kutta time scheme was used with a time step of 10 s. Ordinary (∇^2) diffusion was used with $\nu = 25 \text{ m}^2 \text{ s}^{-1}$ resulting in an e -folding time of 3.5 h for all modes having total wavenumber 170. The same random impulse (3.7) was added to the basic state axisymmetric vorticity field in the eyewall region for each experiment.

The initial conditions of the numerical model experiments are shown in Fig. 3.3. In the left panel, the mean relative vorticity, tangential velocity, and pressure anomaly are

shown for the $[\gamma = 0.0, \delta = 0.00, 0.05, \dots, 0.85]$ rings. This illustrates how varying the ring thickness affects the three curves while holding the hollowness fixed. Similarly the initial conditions for the $[\gamma = 0.0, 0.1, \dots, 0.9, \delta = 0.75]$ rings are shown in the right panel. This illustrates how the three curves change as the hollowness parameter γ is varied while holding the thickness parameter δ fixed. In the left panel, thicker curves represent thinner rings, and in the right panel, thicker curves represent more filled rings. Note that in each case only the inner core profiles ($r < 42$ km) are changing and that the maximum tangential velocity is always the same (approximately 40 m s^{-1}).

The pressure is obtained by solving the nonlinear balance equation

$$\frac{1}{\rho} \nabla^2 p = f \nabla^2 \psi - 2 \left[\left(\frac{\partial^2 \psi}{\partial x \partial y} \right)^2 - \frac{\partial^2 \psi}{\partial x^2} \frac{\partial^2 \psi}{\partial y^2} \right], \quad (3.8)$$

using $f = 5 \times 10^{-5} \text{ s}^{-1}$ and $\rho = 1.13 \text{ kg m}^{-3}$. According to (3.8), in the nondivergent barotropic model the pressure immediately adjusts to the evolving wind field. In the real atmosphere, the adjustment may be accompanied by inertia-gravity wave emission (nonexistent in the nondivergent barotropic model).

Two integral properties associated with (3.4) and (3.5) on a closed domain are the kinetic energy and enstrophy relations

$$\frac{d\mathcal{E}}{dt} = -2\nu\mathcal{Z}, \quad (3.9)$$

$$\frac{d\mathcal{Z}}{dt} = -2\nu\mathcal{P}, \quad (3.10)$$

where the kinetic energy $\mathcal{E} = \iint \frac{1}{2} \nabla \psi \cdot \nabla \psi \, dx \, dy$, the enstrophy $\mathcal{Z} = \iint \frac{1}{2} \zeta^2 \, dx \, dy$, and the palinstrophy $\mathcal{P} = \iint \frac{1}{2} \nabla \zeta \cdot \nabla \zeta \, dx \, dy$. In the absence of diffusion, both kinetic energy and enstrophy are conserved. However, diffusion is necessary to damp the enstrophy cascade to high wavenumbers in a finite resolution model. During vorticity mixing events \mathcal{P} becomes very large causing \mathcal{Z} to decrease. As \mathcal{Z} becomes smaller \mathcal{E} decreases at a slower rate. Thus enstrophy is selectively decayed over energy.

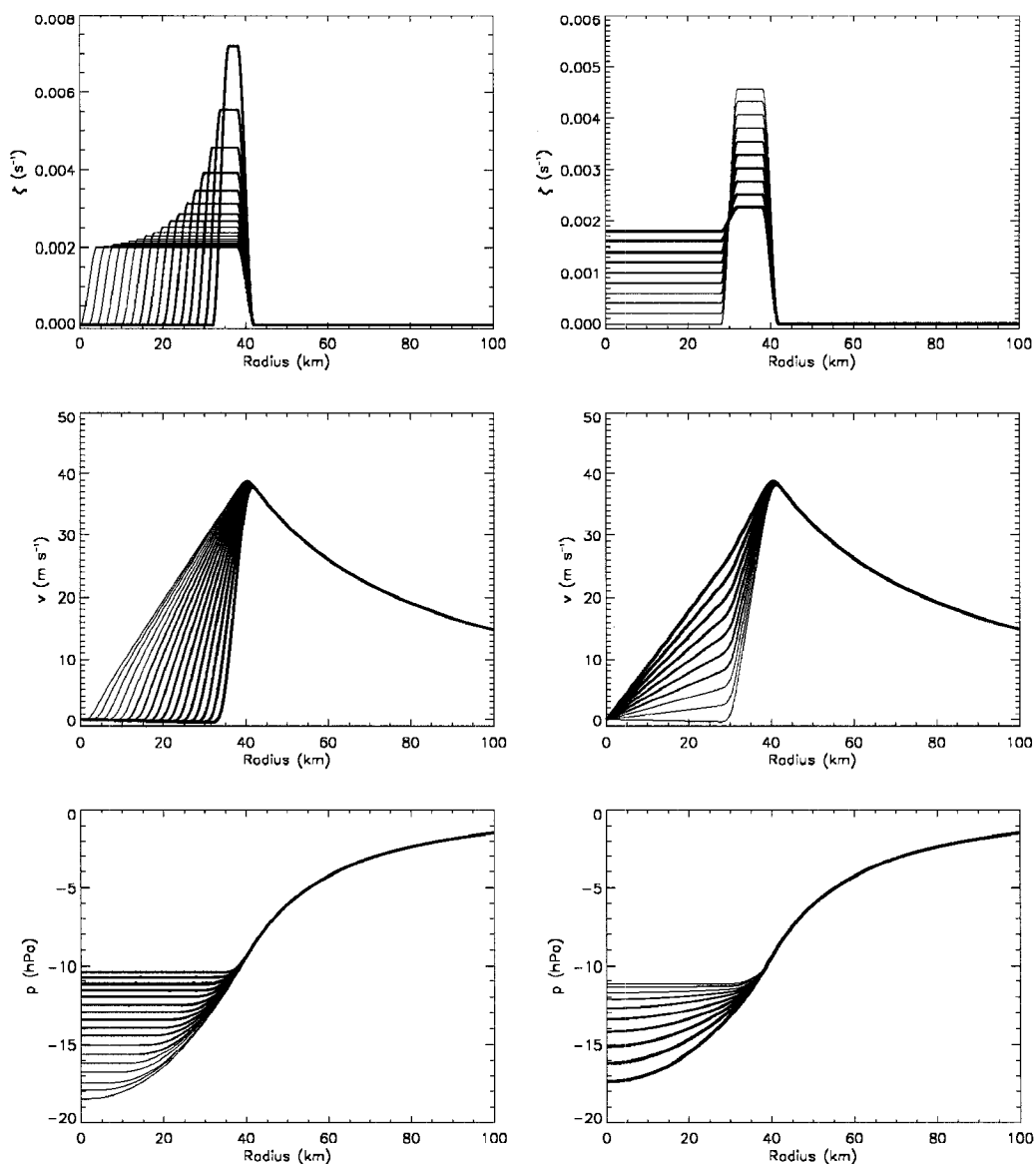


Figure 3.3: Basic state initial condition of various rings. Azimuthal mean relative vorticity, tangential velocity, and pressure are shown for $\gamma = 0.0$ and $\delta = 0.00, 0.05, \dots, 0.85$ (left panels) and for $\gamma = 0.0, 0.1, \dots, 0.9$ and $\delta = 0.75$ (right panels). In the left panels thicker lines indicate increasing δ (rings become thinner) and in the right panels thicker lines indicate increasing γ (rings become more filled).

3.5 Comparison of numerical model results to linear theory

The fastest growing mode at each (δ, γ) point is determined from the output of the pseudospectral model and compared to the linear stability analysis displayed in Fig. 3.2.

By definition, barotropic instability grows by extracting kinetic energy from the mean flow. Therefore, the initial instability seen is the fastest growing mode (largest dimensionless growth rate), and once that mode extracts significant kinetic energy from the mean flow, there is no energy left to support any other slower growing modes. The mode with the maximum dimensionless growth rate is shown in Fig. 3.4 at each of the discrete (δ, γ) points for both the exact linear solution (top panel) and the observed output from the pseudospectral model (bottom panel). In the limit of very fine resolution in (δ, γ) space, the top panel of Fig. 3.4 would reduce to the shaded regions of Fig. 3.2. However, the fastest growing mode is shown at the coarser experimental (δ, γ) points in Fig. 3.4 to allow for a direct comparison with the numerical model (bottom panel). It is clear that when $\delta < 0.5$ the rings are usually stable to exponentially growing modes. Thicker rings are found to be more prone to lower wavenumber growth, while thinner rings are more prone to higher wavenumber growth. As the ring becomes more filled, there is a tendency for the disturbance instability to be at a higher wavenumber.

In comparing the numerical results of the pseudospectral model to the exact linear results of S99 (Fig. 3.4 top and bottom panels), it is found that the S99 linear stability analysis is a good guide to the nonlinear model behavior in the early stages of the evolution. The (δ, γ) structure of the wave growth bands is similar in both cases for W3, W4, ..., etc. There are two main differences. The first and most obvious is the W1 and W2 features observed in the numerical model that are not present in the linear stability analysis. The W1 feature is the algebraically growing instability that is not present in the linear stability analysis due to the assumed form of solution. The observed W2 feature is not present in the linear stability analysis because it is nonexistent in the discrete three-region model with $\gamma > 0$. The analogous continuous three-region model on the other hand does support this instability. It is not clear whether the W2 pattern is a result of an exponential instability (Reasor et al. 2000), diffusion effects (Nolan and Farrell 1999), or a byproduct of nonlinear breakdown of the vorticity ring. In some of these cases the fastest growing mode appears to

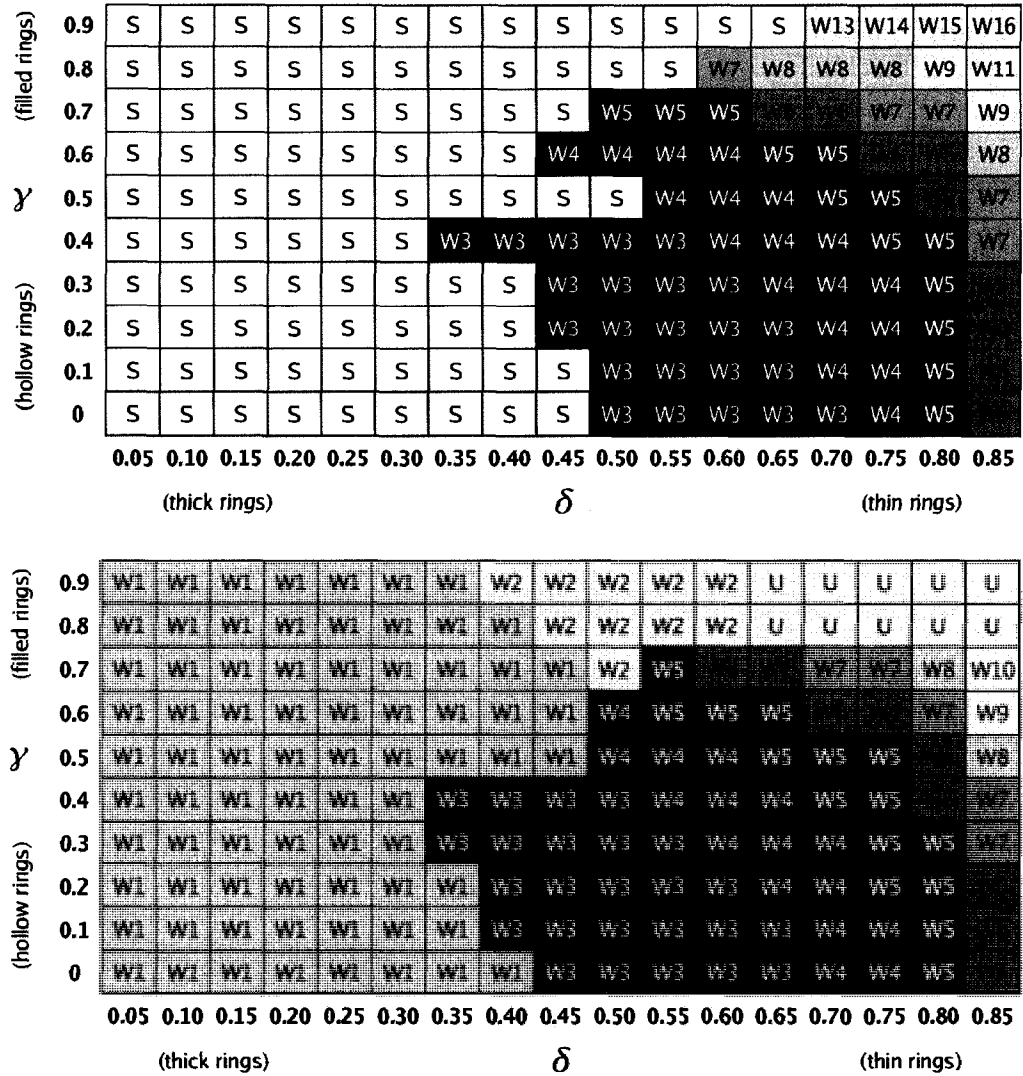


Figure 3.4: Fastest growing wavenumber m (W_m) instability at the discrete δ (abscissa) and γ (ordinate) points using the linear stability analysis of S99 (top), and the observed values from the pseudospectral model (bottom). In the top panel, the 'S' denotes that the vortex was stable to exponentially growing perturbations of all azimuthal wavenumbers. The 'U' in the bottom panel signifies that the initial wavenumber of the instability was undetermined.

be at a higher wavenumber, but then either a secondary instability or nonlinear interactions cause it to slowly evolve into an ellipse. The second difference is that for a given ring thickness in the unstable regime, the numerical model tends to produce a slightly higher

wavenumber exponentially growing mode than expected by the linear theory. As an example of this, at the $(\delta, \gamma) = (0.60, 0.30)$ point the fastest growing mode in the numerical model is wavenumber $m = 4$, while the linear stability analysis of S99 predicts the fastest growing mode to be wavenumber $m = 3$. This difference is probably due to the inclusion of 4 km thick smooth Hermite transition zones between the eye-eyewall and the eyewall-environment in the numerical simulations. Although the average eyewall vorticity in each case is the same, effectively these transition zones make the region of peak vorticity in the experimental rings 4 km thinner than the linear theory rings. In order to illustrate this, take the following example. The $(\delta = 0.70, \gamma)$ points correspond to rings with $r_1 = 26$ km, $r_2 = 30$ km, $r_3 = 38$ km, $r_4 = 42$ km that are filled to various degrees. The same δ value would yield jump radii (r_a and r_b) from the linear theory of $r_a = 28$ km and $r_b = 40$ km. Thus, for this set of δ values, the numerical model sees a peak vorticity region (minus the smooth transitions) that is $r_3 - r_2 = 8$ km thick, while in the linear stability analysis the region would be $r_b - r_a = 12$ km thick. This is the primary reason that the pseudospectral model produces a higher wavenumber instability for a given δ value, and it is particularly more pronounced for thicker rings (essentially the top and bottom panels of Fig. 3.4 cannot be viewed exactly as a one-to-one comparison for the δ points).

Other factors that may contribute weakly to the observed differences are the model horizontal resolution, diffusion (not present in the inviscid vortex used in the linear stability analysis), and periodic boundary conditions. The horizontal resolution (3.52 km) is a little coarse to resolve the early disturbance growth of the thinnest rings ($\delta = 0.85$), but should be sufficient for all other rings. The inclusion of explicit diffusion ($25 \text{ m}^2 \text{ s}^{-1}$) in the numerical model may have some effect on the initial wavenumber instability, but it is likely to be minor since the e -folding time for damping is 3.5 h. Finally, it is possible that the periodicity that exists on a square domain could induce a nonphysical $m = 4$ mode, which would tend to broaden the areal extend of the W4 region in (δ, γ) -space as compared to theory. However, examining Fig. 3.4, this does not appear to occur. Hence, the domain size of $600 \text{ km} \times 600$

km is large enough so that the periodic boundary conditions do not appear to influence the solution to any appreciable degree.

3.6 End states after nonlinear mixing

The end states for each of the 170 experiments were determined. Generally the end states were defined as the stable vorticity structure that existed at $t = 48$ h; however, in some cases additional information during the lifecycle was included. The purpose of characterizing these end states is to provide a guide for assessing the most probable vorticity redistribution in the short term (less than 48 h) given the known axisymmetric characteristics of the initial PV ring.

The list of end state classifications is shown in Table 3.1. The monopole (MP) classification denotes that at $t = 48$ h an approximately axisymmetric, monotonically decreasing vorticity structure has been established. The slow monopole (SP) classification denotes that at $t = 48$ h a monopole did not yet exist, but the trend was such that if the model was run longer (in most cases, less than $t = 72$ h) a monopole would likely form. In these cases, the model was not run long enough to capture the full axisymmetrization process. The mesovortices (MV) classification denotes that two or more local vorticity centers persisted for at least 15 h during the unforced evolution of the ring. With the exception of the $(\delta, \gamma) = (0.85, 0.10)$ ring (in which a stable configuration of four mesovortices existed at $t = 48$ h; Fig. 3.8 left panel), the mesovortices merged into a monopole by $t = 48$ h. The elliptical eyewall (EE) classification denotes an end state involving an ellipse of high vorticity. The polygonal eyewall (PE) classification denotes an end state involving a nonannular eyewall with multiple straight line segments. The shape of the polygon was found to be the same shape as the initial exponentially growing mode. Note that many of the rings having an MP or SP end state exhibited polygonal eyewalls during their evolution to a monopole (see Fig. 3.6). Finally, the trochoidal oscillation (TO) classification signifies that the end state is more or less identical to the initial state, with the exception of the

Table 3.1: End State Definitions

Identifier	Name	Description
TO	Trochoidal Oscillation	Trochoidal oscillation due to the $m=1$ instability
MP	Monopole	Monotonically decreasing vorticity from center
SP	Slow Monopole	Same as monopole but takes longer ($48 \text{ h} \leq t \leq 72 \text{ h}$)
MV	Mesovortices	Two or more mesovortices exist for $\Delta t \geq 15 \text{ h}$
EE	Elliptical Eyewall	Elliptically shaped eyewall
PE	Polygonal Eyewall	Polygonal eyewall with straight line segments

diffusive weakening of the gradients and the trochoidal wobble of the eye due to the $m = 1$ algebraic instability.

The actual end states observed at $t = 48 \text{ h}$ for each (δ, γ) -point are shown in Fig. 3.5. For very thin rings ($\delta = 0.85$), there is a strong tendency to produce multiple persistent, long-lived mesovortices. In the unforced experiments of Kossin and Schubert (2001), mesovortices similar to these had significant meso low pressure areas (as much as 50 mb lower than the environment) and this barotropic breakdown was therefore hypothesized to precede a rapid fall in central pressure. Examining the $\gamma = 0$ row, we see that for moderately thin hollow rings ($0.60 \leq \delta \leq 0.75$), the mostly likely end states are monopoles (MP); for thicker hollow rings ($0.45 \leq \delta \leq 0.55$), the tendency is for slow monopoles (SP); and for thick, hollow rings ($\delta \leq 0.45$), the end states are trochoidal oscillations (TO) generally. For a given δ value, as the eye becomes more filled (increasing γ) there is a tendency for the mixing to a monopole to take longer (more like an SP), and it is less likely to have persistent mesovortices. For moderately thin rings ($0.45 \leq \delta \leq 0.75$) with nearly filled cores ($\gamma \geq 0.60$), there is a tendency for an end state of an elliptical eyewall (EE). This tendency is probably the result of either a slower growing wavenumber $m = 2$ exponential mode or nonlinear effects. For a few moderately filled thick rings there was a tendency for polygonal eyewalls (PE) to exist at $t = 48 \text{ h}$. In these cases, the initial wavenumber $m = 3$ and 4 instability was so slow growing that the low vorticity eye could not be expelled or mixed out, and the resultant structure was an polygonal eyewall of the same character as

the initial instability.

(filled rings)	0.9	TO	TO	TO	TO	TO	TO	TO	EE	EE	EE	EE	EE	SP	SP	SP	SP	SP	
	0.8	TO	TO	TO	TO	TO	TO	TO	TO	EE	EE	EE	EE	SP	SP	SP	SP	SP	
(hollow rings)	0.7	TO	TO	TO	TO	TO	TO	TO	TO	TO	EE	EE	SP	SP	SP	SP	SP	MP	
	0.6	TO	TO	TO	TO	TO	TO	TO	TO	TO	EE	EE	EE	SP	SP	SP	MP	MP	
	0.5	TO	TO	TO	TO	TO	TO	TO	TO	TO	PE	PE	SP	SP	MP	MP	MP	MP	
	0.4	TO	TO	TO	TO	TO	TO	TO	PE	PE	PE	PE	SP	SP	SP	MP	MP	MP	MV
	0.3	TO	TO	TO	TO	TO	TO	TO	PE	SP	SP	SP	SP	MP	MP	MP	MP	MP	MV
	0.2	TO	TO	TO	TO	TO	TO	TO	PE	SP	SP	SP	SP	MP	MP	MP	MP	MP	MV
	0.1	TO	TO	TO	TO	TO	TO	TO	PE	SP	SP	SP	SP	MP	MP	MP	MP	MP	MV
	0	TO	TO	TO	TO	TO	TO	TO	TO	SP	SP	SP	SP	MP	MP	MP	MP	MP	MV
			0.05	0.10	0.15	0.20	0.25	0.30	0.35	0.40	0.45	0.50	0.55	0.60	0.65	0.70	0.75	0.80	0.85
			(thick rings)							δ					(thin rings)				

Figure 3.5: End states observed in the pseudospectral model after nonlinear vorticity mixing at $t = 48$ h at the discrete δ (abscissa) and γ (ordinate) points

The complete lifecycles of some unstable rings are shown in Figs. 3.6, 3.7, and 3.8. The left panel of Fig. 3.6 depicts the evolution of the $(\delta, \gamma) = (0.75, 0.20)$ ring. The initial instability is $m = 5$ (although close to $m = 4$), and the end state is a monopole. The right panel of Fig. 3.6 depicts the evolution of the $(\delta, \gamma) = (0.50, 0.20)$ ring. The initial instability is $m = 3$, and the end state is a slow monopole. If the model were run slightly longer the PV mixing process would be complete and the low vorticity eye would be expelled. Fig. 3.7 (left panel) depicts the evolution of the $(\delta, \gamma) = (0.55, 0.80)$ ring. The initial instability is $m = 2$, and the end state is an elliptical eyewall. Fig. 3.7 (right panel) depicts the evolution of the $(\delta, \gamma) = (0.50, 0.50)$ ring. The initial instability is $m = 4$, and the end state is a square, polygonal eyewall. Fig. 3.8 (left panel) depicts the evolution of the $(\delta, \gamma) = (0.85, 0.10)$ ring. The initial instability is $m = 6$, and the end state is a stable (non-merging) pattern of four mesovortices. Fig. 3.8 (right panel) depicts the evolution of the $(\delta, \gamma) = (0.25, 0.70)$ ring. The initial instability is $m = 1$, and the end state is a wobbling eye (TO).

The evolution of the normalized enstrophy $\mathcal{Z}(t)/\mathcal{Z}(0)$ for each of the above rings is

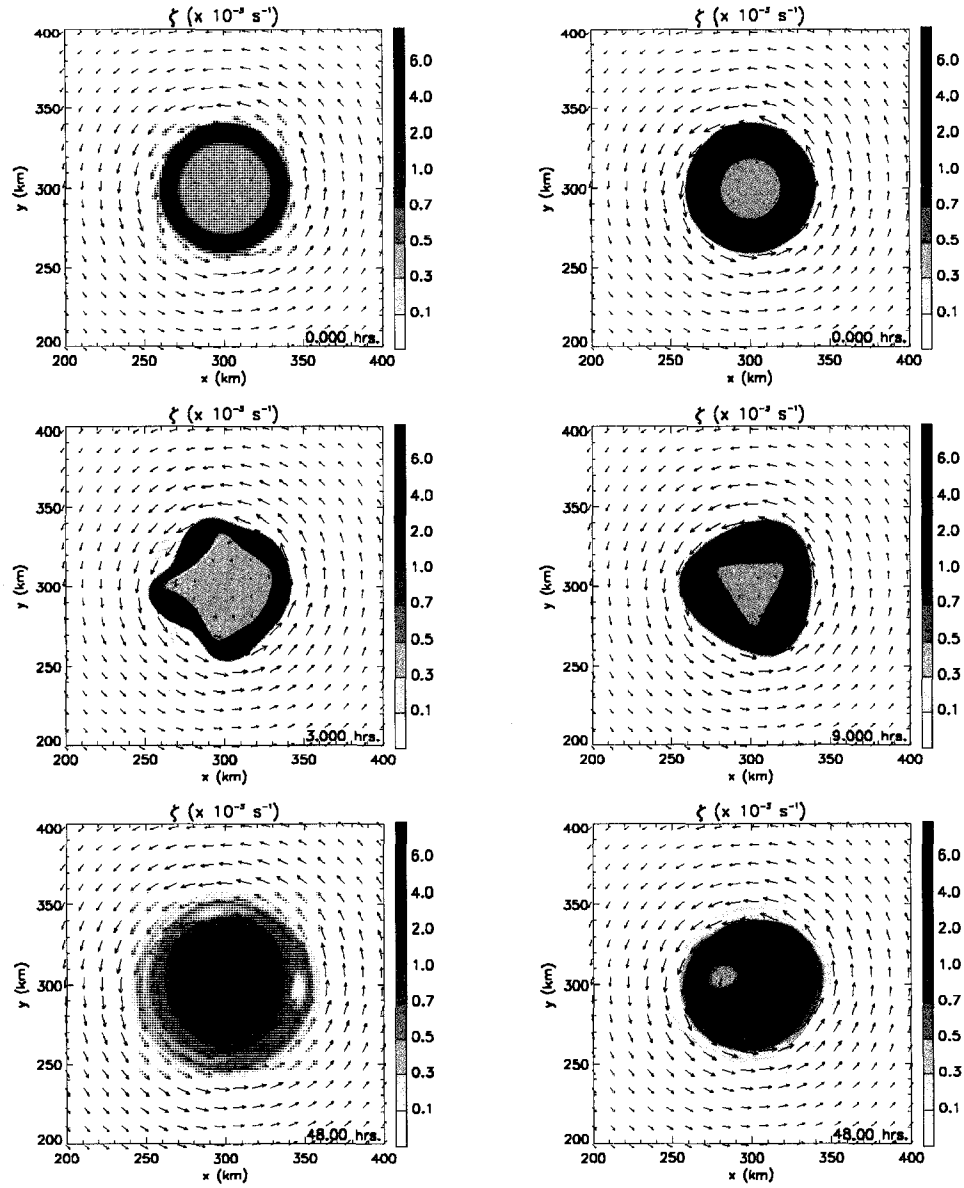


Figure 3.6: The evolution of the $(\delta, \gamma) = (0.75, 0.20)$ ring (left) and the $(\delta, \gamma) = (0.50, 0.20)$ ring (right). The end states are MP and SP respectively.

shown in Fig. 3.9. For the SR, EE and PE classifications the enstrophy decay was gradual and small. For the SP classification, the enstrophy decay was gradual and slightly larger. For the MP and MV classifications, the enstrophy decay was rapid and large. In one MV case, the $(\delta, \gamma) = (0.85, 0.00)$ ring, a staircase pattern was observed associated with

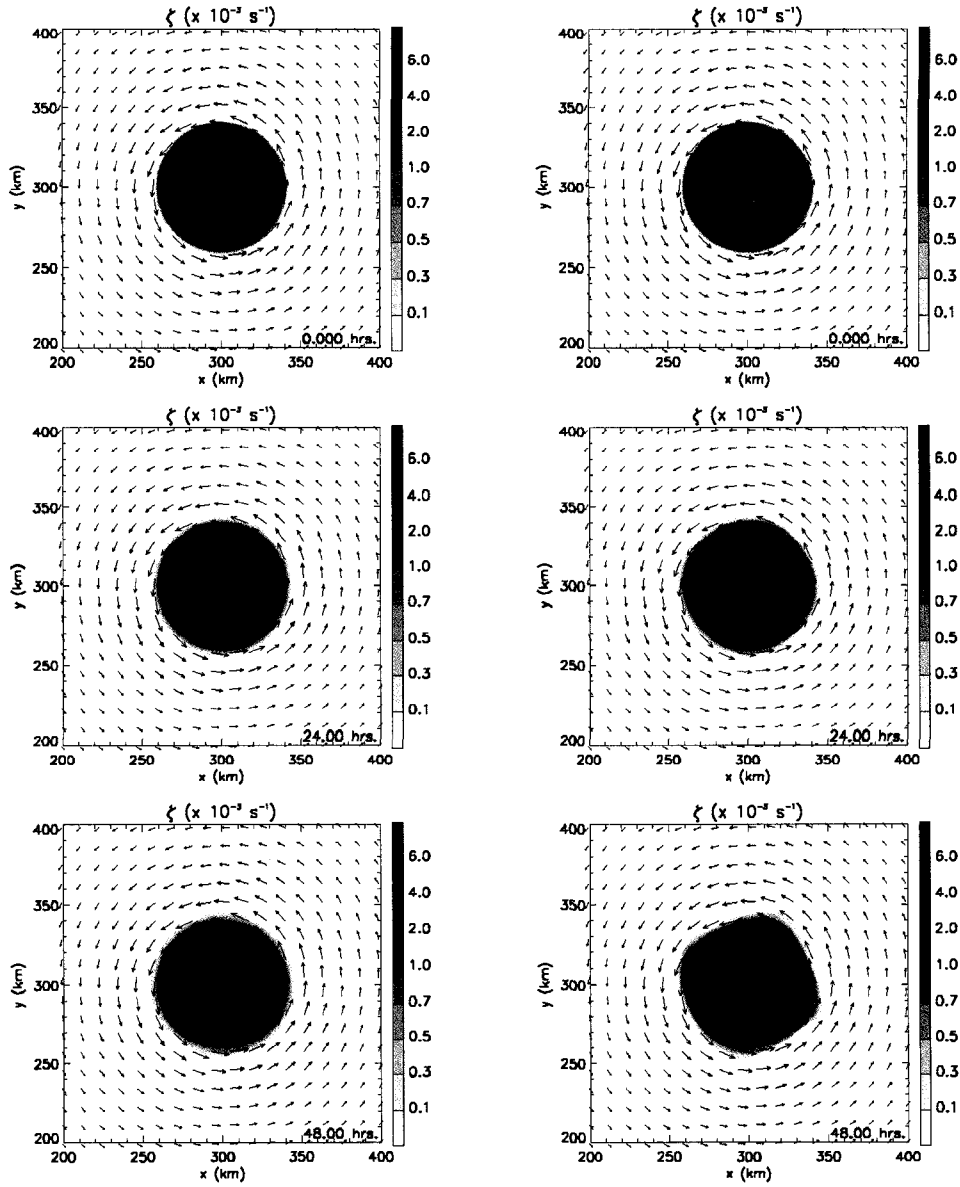


Figure 3.7: The evolution of the $(\delta, \gamma) = (0.55, 0.80)$ ring (left) and the $(\delta, \gamma) = (0.50, 0.50)$ ring (right). The end states are EE and PE respectively.

mesovortex mergers. In the other MV case, this pattern was not observed because the four mesovortices that formed during the initial ring breakdown did not undergo any subsequent mergers. These results are broadly consistent with the PV ring rearrangement study of Wang (2002).

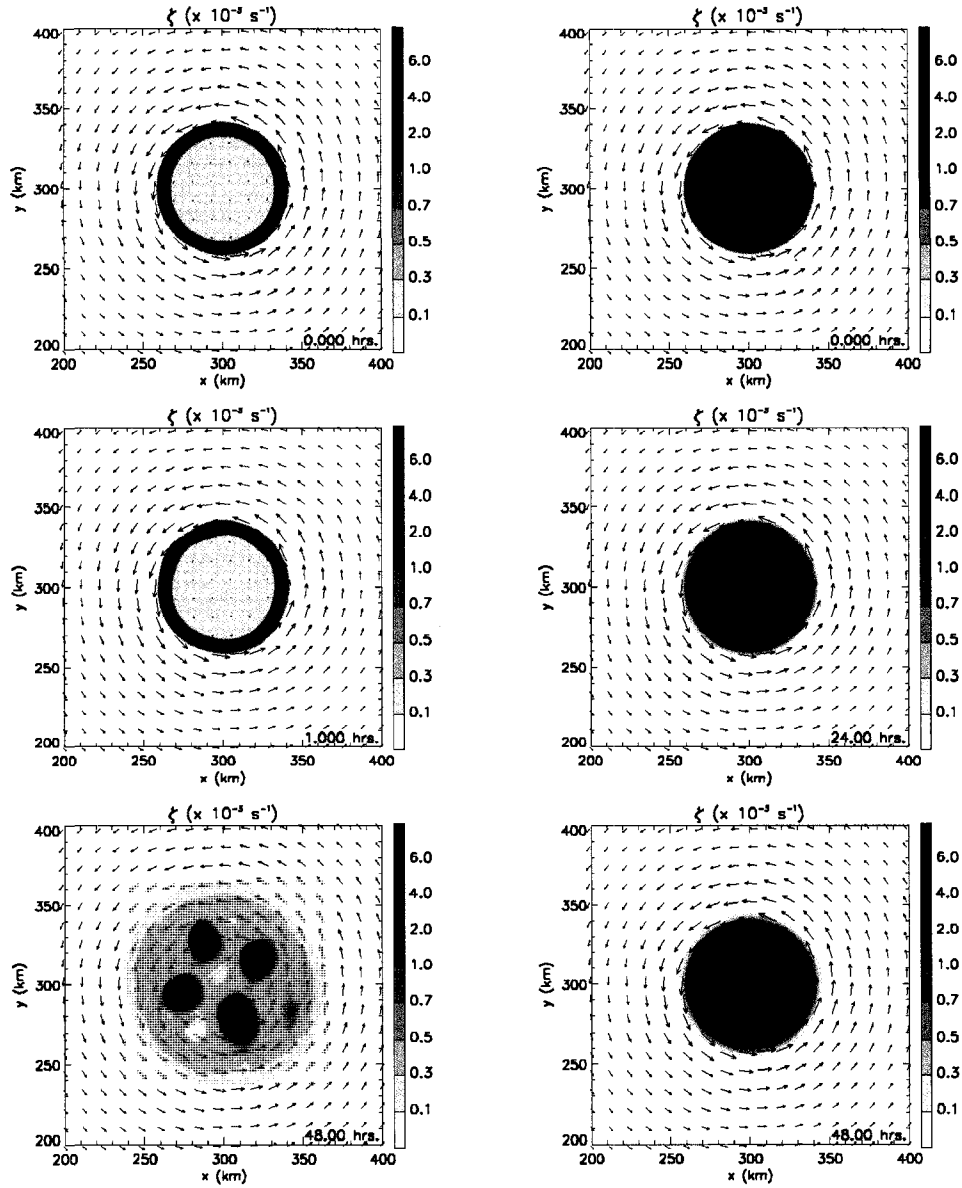


Figure 3.8: The evolution of the $(\delta, \gamma) = (0.85, 0.10)$ ring (left) and the $(\delta, \gamma) = (0.25, 0.70)$ ring (right). The end states are MV and TO respectively.

3.7 PV mixing and hurricane intensity change

What is the relationship between inner-core PV mixing and hurricane intensity change?

A complete answer to this question would require a comprehensive study of both forced (with diabatic heating effects) and unforced simulations using a hierarchy of numerical models:

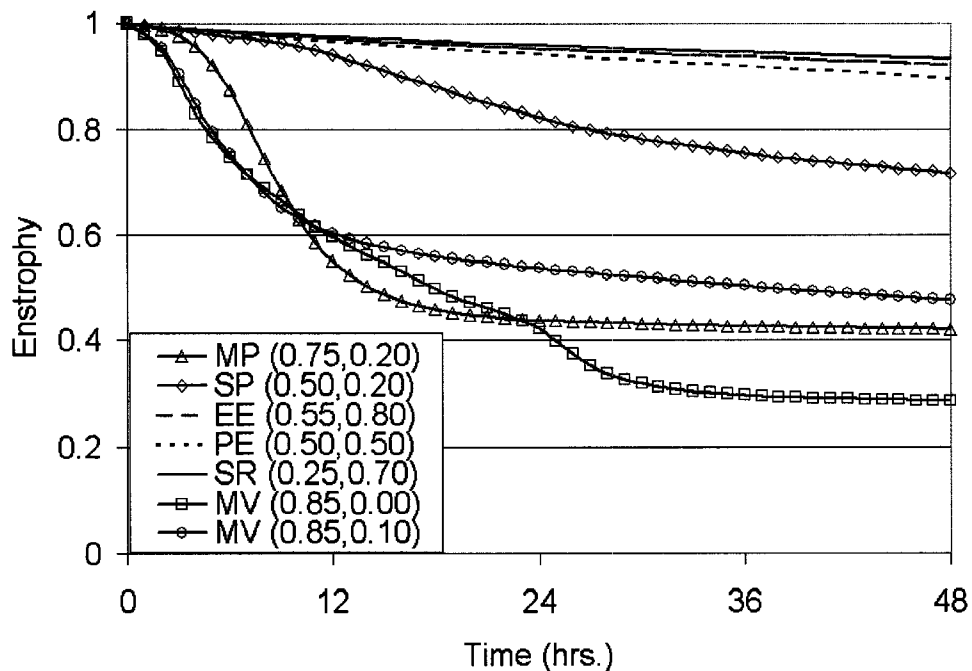


Figure 3.9: Evolution of the enstrophy $\mathcal{Z}(t)/\mathcal{Z}(0)$ for the rings in Figs. 3.6–3.8. An additional MV curve is plotted for the $(\delta, \gamma) = (0.85, 0.00)$ ring.

the nondivergent barotropic model, shallow water model, quasi-static primitive equation model, and full-physics nonhydrostatic model. And that work should be complemented with available observational data. In this section, we examine the relationship between PV mixing and intensity change in the unforced nondivergent barotropic context – see Rozoff et al. (2008) for the analogous problem in the forced nondivergent barotropic model.

In Fig. 3.10, the changes in azimuthal mean vorticity, tangential velocity, and central pressure from $t = 0$ h (solid curve) to $t = 48$ h (dashed curve) are shown for the evolution of two rings: $(\delta, \gamma) = (0.7, 0.7)$ (left panel) and $(\delta, \gamma) = (0.0, 0.85)$ (right panel). The end states are SP and MP, respectively. In the left panel, it can be seen that the azimuthal mean relative vorticity is not yet monotonic, however the mixing is proceeding such that a monopole would form later. During its evolution both the peak tangential velocity and central pressure decreased slightly ($\Delta \bar{v}_{\max} = -3.9 \text{ m s}^{-1}$ and $\Delta p_{\min} = -0.8 \text{ hPa}$). In the

right panel, the annulus of vorticity was redistributed to a monopole causing the radius of maximum wind (RMW) to contract approximately 25 km in 48 hours. Both the tangential velocity and central pressure decreased significantly ($\Delta\bar{v}_{\max} = -7.7 \text{ m s}^{-1}$ and $\Delta p_{\min} = -14.4 \text{ hPa}$) during this period.

The changes in maximum tangential velocity and central pressure for each ring examined in this study is shown in Fig. 3.11. In the top panel the change in central pressure is shown with light gray denoting a pressure change of $-5 \text{ hPa} \leq \Delta p_{\min} < 0 \text{ hPa}$ and dark gray denoting a pressure change of $\Delta p_{\min} < -5 \text{ hPa}$. In the bottom panel the changes in peak tangential velocity are shown with light gray denoting a change $-7 \text{ m s}^{-1} \leq \Delta\bar{v}_{\max} < -3 \text{ m s}^{-1}$ and dark gray denoting a change $\Delta\bar{v}_{\max} < -7 \text{ m s}^{-1}$. The main conclusion from this figure is that for all rings that underwent PV mixing episodes both the tangential velocity and central pressure decreased. The decreases were most pronounced for thin, hollow rings that mixed to a monopole or mesovortices that persisted and then merged into a monopole (cf. Kossin and Schubert 2001). Note that since the $(\delta, \gamma) = (0.85, 0.10)$ ring had an end state of 4 mesovortices, the central pressure fall was weak; however, lower pressure anomalies were associated with each mesovortex.

Empirical pressure-wind relationships² generally have the form

$$v_{\max} = C(p_{\text{ref}} - p_c)^n, \quad (3.11)$$

where C and n are empirical constants, v_{\max} is the maximum azimuthal velocity, p_{ref} is the reference pressure, and p_c is the central pressure. Such approximations may not be valid during PV mixing events. To illustrate why this is the case, we write the cyclostrophic balance equation $v^2/r = (1/\rho)(\partial p/\partial r)$ in its integral form:

$$\int_0^{r_{\text{ref}}} \rho \frac{v^2}{r} dr = p_{\text{ref}} - p_c, \quad (3.12)$$

where r_{ref} is the radius at which the pressure equals p_{ref} . Comparing the empirical relation (3.11) with the cyclostrophic balance relation (3.12), we see that (3.11) is justified if the

² For a review of empirical pressure-wind relationships and a reanalysis of their validity with observed storms, see Knaff and Zehr (2007).

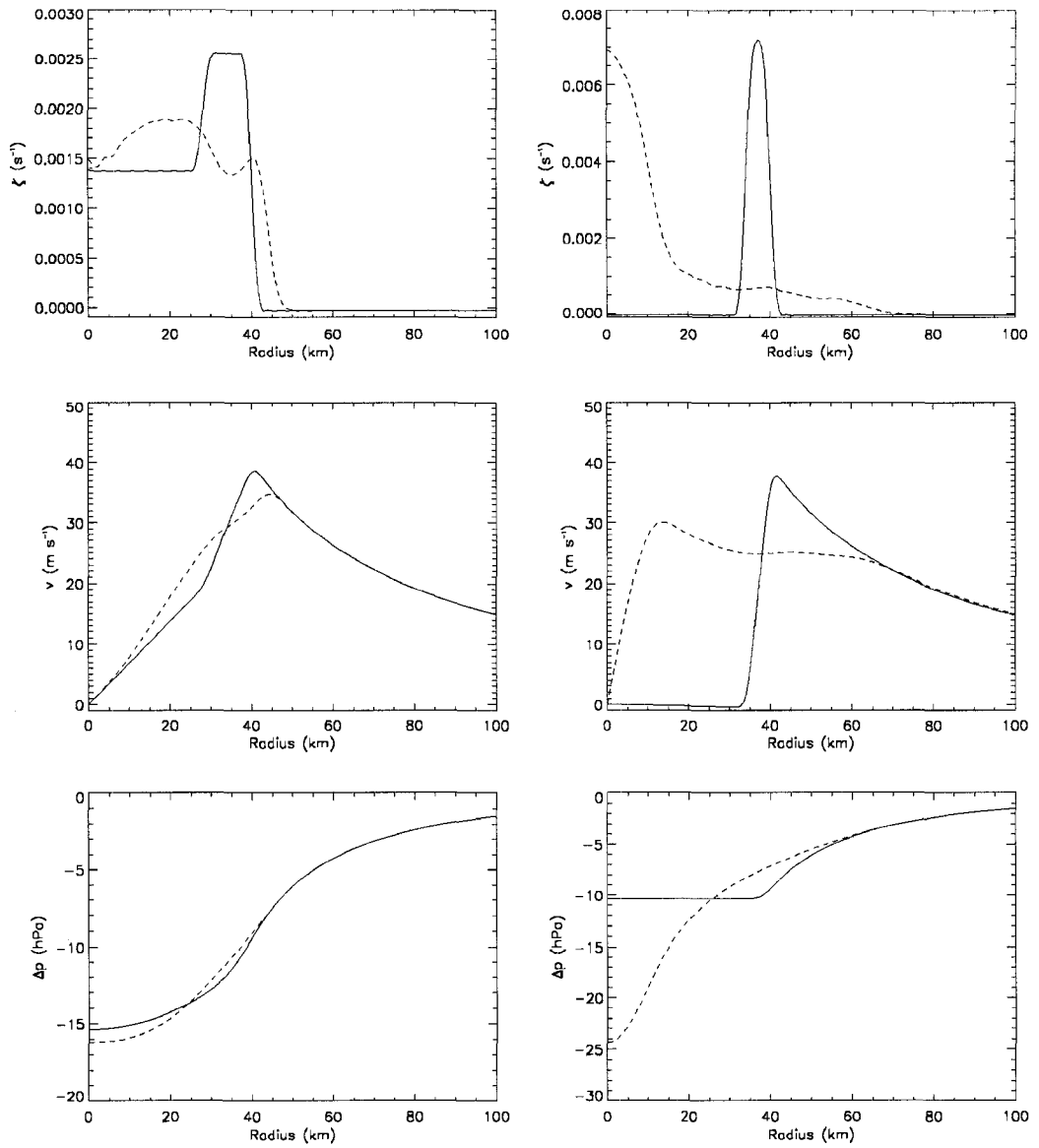


Figure 3.10: The initial ($t = 0$ h; solid curve) and final ($t = 48$ h; dashed curve) azimuthal mean relative vorticity, tangential velocity, and pressure for the $(\delta, \gamma) = (0.70, 0.70)$ ring (left) and the $(\delta, \gamma) = (0.85, 0.00)$ ring (right). The pressure is expressed as a deviation from the environment. The end states of the two rings are SP and MP, respectively.

integral on the left hand side of (3.12) can be accurately approximated by $(v_{\max}/C)^{1/n}$ for all the $v(r)$ profiles encountered during PV mixing events. Examining the two tangential velocity profiles in Fig. 3.10 (middle right panel), we see that although the peak tangential

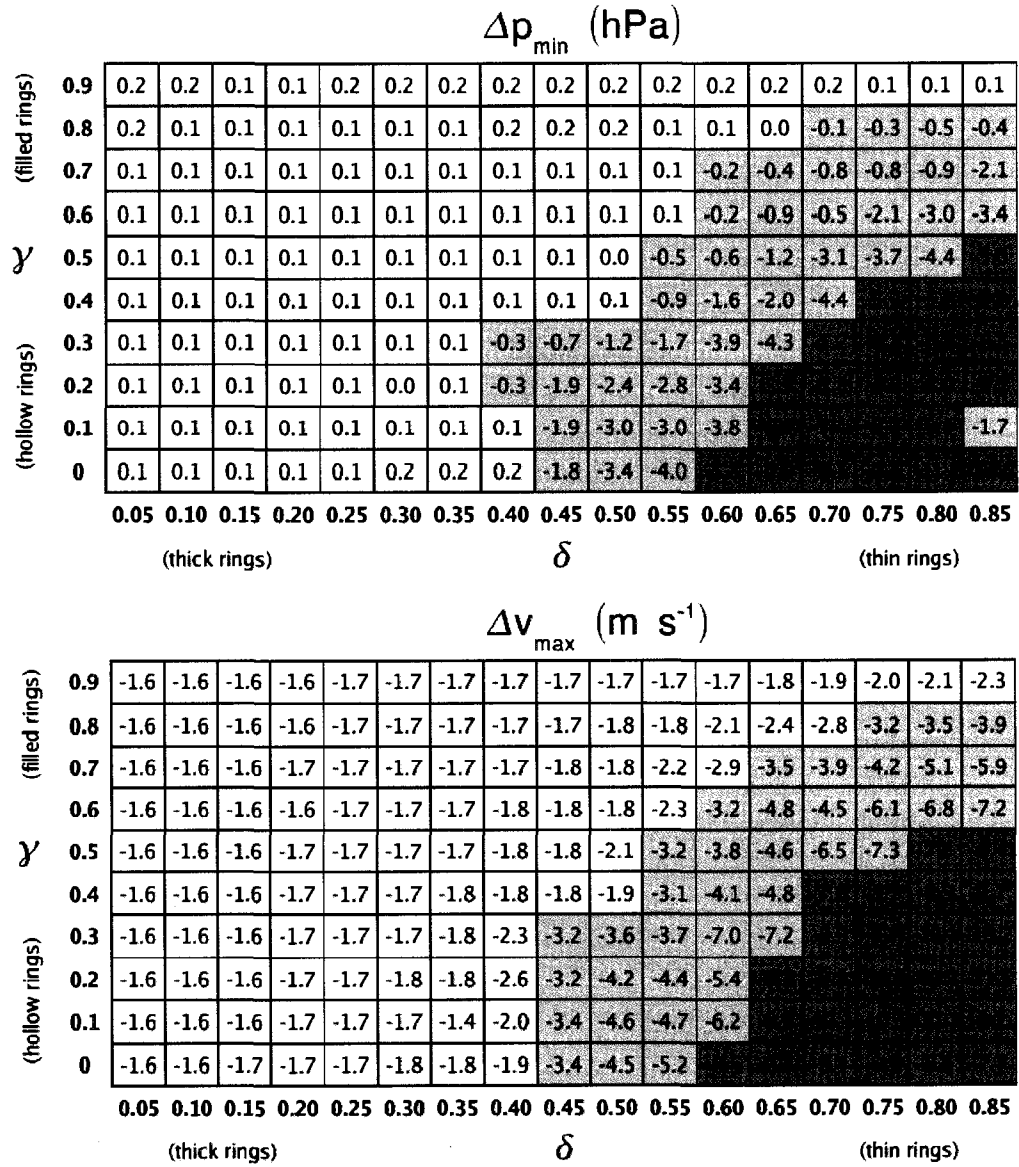


Figure 3.11: (top panel) Central pressure change (hPa) from $t = 0$ h to $t = 48$ h for each ring. Negative values (pressure drop) are shaded with $-5 \leq \Delta p_{\min} \leq 0$ in light gray and $\Delta p_{\min} \leq -5$ in dark gray. (bottom panel) Maximum tangential velocity change (m s⁻¹) from $t = 0$ h to $t = 48$ h for each ring: $-7 \leq \Delta \bar{v}_{\max} \leq -3$ (light gray shading) and $\Delta \bar{v}_{\max} \leq -7$ (dark gray shading).

velocity decreased, there exists a much larger radial region of higher winds for the dashed curve at $t = 48$ h. The pressure fall, which must account for the entire radial integral, is

therefore larger in this case even though the peak winds decreased. In addition, mixing of angular momentum to small radii causes the v^2/r term to be large there, contributing to the pressure fall. Based on these results, special care must be taken when using empirical pressure-wind relationships during PV mixing events. We have examined this issue in the context of a nondivergent barotropic model, which is an oversimplification of the moist atmosphere. Nonetheless, if PV mixing is primarily a barotropic process that proceeds adiabatically (even though the hollow tower generation is diabatic) with little gravity wave radiation, these results should generalize to the real atmosphere with only minor changes.

3.8 Summary

The lifecycles of 170 different hurricane-like potential vorticity (PV) rings, filling the parameter space of the hollowness of the core (defined by the ratio of eye to inner-core relative vorticity) and the thickness of the ring (defined by the ratio of the inner and outer radii), were examined in a nondivergent barotropic model framework. In approximately one-half the cases the ring became dynamically unstable, causing vorticity to be mixed from the eyewall to the eye. In the early part of the lifecycle, the fastest growing exponential mode was compared to the linear stability analysis of Schubert et al. (1999). In the later part (nonlinear mixing), the resultant end states were characterized for each ring at $t = 48$ h.

It was found that the linear stability analysis of S99 is a good guide to the nonlinear model behavior in the exponential wave growth phase of the lifecycle. The assumptions used in the S99 linear stability analysis eliminated the possibility of wavenumbers $m = 1$ (algebraic) and $m = 2$ instabilities, which were both observed in the pseudospectral model results. The slowly growing wavenumber $m = 1$ instability was visible as a wobble of the eye in thick, filled rings that were stable to all other exponentially growing modes. If the vortex were moving, this wobble would be observed as a trochoidal oscillation. A wavenumber $m = 2$ pattern was observed for a few moderately thick, nearly filled rings. This

was most likely due to either an exponential instability (allowed by the model's continuous vorticity profile), or nonlinear vorticity mixing. Elliptically shaped vorticity structures have been observed in hurricanes (Reasor et al. 2000; Corbosiero et al. 2006) and simulated as a nonlinear interaction between a monopole and a secondary ring of enhanced vorticity (Kossin et al. 2000), however their formation dynamics are not clear in the evolution of unforced PV rings.

The most likely end state of all unstable rings was a monopole. For thick, filled rings, the relaxation to a monopole took longer than for thin, hollow rings. For very thin rings with relatively hollow cores, multiple long-lived (order 15 h) mesovortices persisted before mixing to a monopole. For moderately thick and filled rings, the end state was an elliptical eyewall that formed due to the wavenumber $m = 2$ feature described above. For some thick and moderately filled rings, the end state was a polygonal eyewall of the same character as the initial instability.

For all rings that underwent a barotropic breakdown and PV mixing, both the central pressure and peak azimuthal mean tangential velocity decreased. The most dramatic pressure and tangential velocity decreases were found for thin, hollow rings that formed monopoles, or mesovortices that persisted and then merged into monopoles. In a 48 h time frame, the storms that formed monopoles (on average) had a central pressure fall of 6 hPa and tangential velocity fall of 9 m s^{-1} . Weaker falls for both quantities were found for slow monopoles (1 hPa and 4 m s^{-1} , respectively). Very minor changes occurred for all other rings.

In real hurricanes, diabatic effects tend to constantly produce a PV hollow tower. This hollow tower will periodically become dynamically unstable and PV will be mixed from the eyewall into the eye. Subsequently, diabatic heating will tend to regenerate the hollow tower, from which another mixing episode may occur, and so forth. In this work, we have shown what end states are most likely to result from these short term (order of a couple days) episodic PV mixing events for hollow towers (PV rings in the barotropic context) that

are filled and thin to various degrees. For strong and intensifying hurricanes that produce thin hollow towers, these results suggest another mechanism by which the central pressure can rapidly fall. Thus PV mixing may complement the intensification process.

Finally, we have chosen a very simple framework (nondivergent barotropic model) to study this problem. In real hurricanes, where baroclinity and moist processes are important, these results may change to some degree. Future work should be focused on studying the relationship between inner-core PV mixing and hurricane intensity change in more complex models. Logical next steps to the current work would be the examination of PV mixing in both shallow water and three-dimensional quasi-hydrostatic primitive equation model frameworks. In the former case, the results are hypothesized to be nearly the same, however, spontaneous gravity wave emission from thin ring breakdowns may be significant. In the latter case, one could examine the adiabatic lifecycles of initially hollow PV towers, including the preferred isentropic layers for PV mixing.

Chapter 4

IDEALIZED MESOSCALE MODELS FOR STUDYING TROPICAL CYCLONE DYNAMICS

4.1 Introduction

In constructing an atmospheric mesoscale model many choices must be made. First, the desired fidelity of the model must be determined: (i) hydrostatic or nonhydrostatic, (ii) inclusion or exclusion of moist processes, (iii) inclusion and complexity of various physics parameterizations, such as planetary boundary layer, microphysical, cumulus and radiation schemes. Next, numerical considerations must be taken into account such as the use of the finite difference, finite volume or spectral methods for solving the governing equations. One of major appeals of the spectral method is that the error decays exponentially with increasing resolution, while for finite difference methods the error generally decays algebraically (Fulton and Schubert 1987a,b). However, this nice quality is partially negated by the requirement of periodicity at the lateral boundaries (for Fourier spectral methods) and the Gibbs phenomenon that arises when attempting to represent steep gradients.

Choices must also be made for the vertical coordinate. A popular choice is the terrain-following σ -coordinate which is used in many mesoscale models such as the full-physics Regional Atmospheric Modeling System (RAMS; Pielke et al. 1992) and the Weather Research and Forecasting Model (WRF; Skamarock et al. 2005). However, the expense that is paid for the terrain-following property is the separation of the horizontal pressure gradient force into two terms that may be large and of opposite sign near steep topography. Another option is the isentropic vertical coordinate. Since isentropic surfaces are material surfaces,

a quasi-Lagrangian view of the atmosphere may be obtained in these models. The primary problem with this coordinate is that for realistic planetary boundary layers θ -surfaces will intersect the ground. The benefits of the isentropic coordinate at upper levels and σ -coordinate near the surface have led to the development of hybrid σ - θ coordinates (Simmons and Burridge 1981; Konor and Arakawa 1997). With any hybrid coordinate, however, there are consistency issues at the coordinate surface transitions. Although not widely used in numerical models, some other vertical choices are physical height, pseudoheight (Hoskins and Bretherton 1972), pressure and log-pressure coordinates.

With idealized hurricane and vortex simulations in mind, two hydrostatic primitive equation models were made using a periodic, spectral shallow water model (Fulton 2007) as a starting point. The first model uses an isentropic vertical coordinate and the second uses a sigma-vertical coordinate. The models include dynamical cores with the option of prognostic equations for either the momentum or the vertical vorticity and divergence. The equations are solved on a limited area periodic, f -plane domain. At this point, the models are simple. There is no moisture or surface fluxes. Similar to operational global models (e.g., the ECMWF model), the model uses the Fourier spectral representation in the horizontal and finite difference schemes in the vertical. As we will see, the horizontal Fourier spectral representation is ideal for simulating the intricate details of asymmetric PV mixing in hurricanes. In section 4.2, the quasi-hydrostatic primitive equations on which the model is based are shown. In section 4.3, the horizontal discretizations are described. The temporal discretization options are discussed in section 4.4. The vertically discrete isentropic and sigma coordinate models are described in section 4.5. Some additional features of the model are described in section 4.6. The initialization procedure is shown in section 4.7. Some preliminary verification and validation tests are presented in section 4.8, including unforced PV hollow tower simulations. Finally, a summary of the results is presented in section 4.9.

4.2 Governing Equations

We consider a compressible atmosphere constrained by quasi-hydrostatic motions on an f -plane. Using the generalized $\eta(p, p_s, \theta)$ vertical coordinate, the equations are shown for both isentropic ($\eta = \theta$) and sigma ($\eta = \sigma = (p - p_t)/(p_s - p_t)$) vertical coordinates.

4.2.1 Isentropic vertical coordinate

The isentropic vertical coordinate primitive equations in rotational form are shown below. The horizontal momentum equations can be cast in either layer momentum and vorticity-divergence form. In momentum form, given a layer velocity $\mathbf{u} = (u, v)$ the equations for zonal and meridional momentum are

$$\frac{\partial u}{\partial t} + \dot{\theta} \frac{\partial u}{\partial \theta} - mPv + \frac{\partial}{\partial x} (M + K) = F_u, \quad (4.1)$$

$$\frac{\partial v}{\partial t} + \dot{\theta} \frac{\partial v}{\partial \theta} + mPu + \frac{\partial}{\partial y} (M + K) = F_v. \quad (4.2)$$

By taking the curl ($\mathbf{k} \cdot \nabla_{\theta} \times$) and divergence ($\nabla_{\theta} \cdot$) of $\partial \mathbf{u} / \partial t$, the equations in vorticity-divergence form are

$$\frac{\partial \zeta_{\theta}}{\partial t} + \frac{\partial}{\partial x} \left(\dot{\theta} \frac{\partial v}{\partial \theta} \right) - \frac{\partial}{\partial y} \left(\dot{\theta} \frac{\partial u}{\partial \theta} \right) + \frac{\partial(mPu)}{\partial x} + \frac{\partial(mPv)}{\partial y} = F_{\zeta}, \quad (4.3)$$

$$\frac{\partial \delta_{\theta}}{\partial t} + \frac{\partial}{\partial x} \left(\dot{\theta} \frac{\partial u}{\partial \theta} \right) + \frac{\partial}{\partial y} \left(\dot{\theta} \frac{\partial v}{\partial \theta} \right) + \frac{\partial(mPu)}{\partial y} - \frac{\partial(mPv)}{\partial x} + \nabla^2 (K + M) = F_{\delta}. \quad (4.4)$$

The hydrostatic, continuity, and thermodynamic equations are the same for both formulations:

$$\frac{\partial M}{\partial \theta} = \Pi, \quad (4.5)$$

$$\frac{\partial m}{\partial t} + \frac{\partial(mu)}{\partial x} + \frac{\partial(mv)}{\partial y} + \frac{\partial(m\dot{\theta})}{\partial \theta} = 0, \quad (4.6)$$

$$\dot{\theta} = \frac{Q}{\Pi}. \quad (4.7)$$

Here, u is zonal momentum, v is the meridional momentum, $K = (u^2 + v^2)/2$ is the kinetic energy, $\Pi = c_p(p/p_0)^\kappa$ is the Exner function, $\Phi = gz$ is the geopotential, $M = \theta\Pi + \Phi$ is the Montgomery potential, F are arbitrary momentum sources and sinks, Q is a heat source or sink, $\eta_\theta = f + \partial v/\partial x - \partial u/\partial y$ is the isentropic absolute vertical vorticity, $\zeta_\theta = \partial v/\partial x - \partial u/\partial y$ is the isentropic relative vertical vorticity, $m = -\partial p/\partial \theta$ is the pseudodensity, $\dot{\theta}$ is the diabatic heating rate, and $P = \eta_\theta/m$ is the potential vorticity. All variables are functions of x , y , θ , and t , and all horizontal derivatives are taken on isentropic ($\theta = \text{const.}$) surfaces.

The potential vorticity principle can be obtained by combining (4.3) and (4.6) while eliminating the isentropic divergence:

$$\frac{DP}{Dt} = \frac{1}{m} \left[P \frac{\partial(m\dot{\theta})}{\partial \theta} - \frac{\partial}{\partial x} \left(\dot{\theta} \frac{\partial v}{\partial \theta} \right) + \frac{\partial}{\partial y} \left(\dot{\theta} \frac{\partial u}{\partial \theta} \right) + F_\zeta \right]. \quad (4.8)$$

Note than in the absence of diabatic heating and friction, P is materially conserved.

4.2.2 *Sigma vertical coordinate*

The sigma vertical coordinate primitive equations in rotational form are shown below, in both momentum and vorticity-divergence formulations as well. The horizontal momentum equations are

$$\frac{\partial u}{\partial t} + \dot{\sigma} \frac{\partial u}{\partial \sigma} - \eta_\sigma v + \frac{\partial}{\partial x} (\Phi + K) + \sigma \alpha \frac{\partial p_s}{\partial x} = F_u, \quad (4.9)$$

$$\frac{\partial v}{\partial t} + \dot{\sigma} \frac{\partial v}{\partial \sigma} + \eta_\sigma u + \frac{\partial}{\partial y} (\Phi + K) + \sigma \alpha \frac{\partial p_s}{\partial y} = F_v. \quad (4.10)$$

Similarly taking the curl ($\mathbf{k} \cdot \nabla_\sigma \times$) and divergence ($\nabla_\sigma \cdot$) of $\partial \mathbf{u}/\partial t$, the σ -coordinate equations in vorticity-divergence form are

$$\begin{aligned} \frac{\partial \zeta_\sigma}{\partial t} + \frac{\partial}{\partial x} \left(\dot{\sigma} \frac{\partial v}{\partial \sigma} \right) - \frac{\partial}{\partial y} \left(\dot{\sigma} \frac{\partial u}{\partial \sigma} \right) + \frac{\partial(\eta_\sigma u)}{\partial x} \\ + \frac{\partial(\eta_\sigma v)}{\partial y} + \sigma \left(\frac{\partial \alpha}{\partial x} \frac{\partial p_s}{\partial y} - \frac{\partial \alpha}{\partial y} \frac{\partial p_s}{\partial x} \right) = F_\zeta, \end{aligned} \quad (4.11)$$

$$\begin{aligned} \frac{\partial \delta_\sigma}{\partial t} + \frac{\partial}{\partial x} \left(\dot{\sigma} \frac{\partial u}{\partial \sigma} \right) + \frac{\partial}{\partial y} \left(\dot{\sigma} \frac{\partial v}{\partial \sigma} \right) + \frac{\partial(\eta_\sigma u)}{\partial y} \\ - \frac{\partial(\eta_\sigma v)}{\partial x} + \nabla^2 (\Phi + M) + \sigma \alpha \nabla^2 p_s \\ + \sigma \left(\frac{\partial \alpha}{\partial x} \frac{\partial p_s}{\partial x} + \frac{\partial \alpha}{\partial y} \frac{\partial p_s}{\partial y} \right) = F_\delta. \end{aligned} \quad (4.12)$$

The hydrostatic, continuity, and thermodynamic equations are the same for both formulations:

$$\frac{\partial \Phi}{\partial \sigma} = -p_s \alpha, \quad (4.13)$$

$$\frac{\partial p_s}{\partial t} + \frac{\partial(p_s u)}{\partial x} + \frac{\partial(p_s v)}{\partial y} + \frac{\partial(p_s \dot{\sigma})}{\partial \sigma} = 0, \quad (4.14)$$

$$\frac{D\theta}{Dt} = Q. \quad (4.15)$$

Here, $\eta_\sigma = f + \partial v / \partial x - \partial u / \partial y$ is the absolute vertical vorticity on a σ surface, $\zeta_\sigma = \partial v / \partial x - \partial u / \partial y$ is the relative vertical vorticity on a σ surface, p_s is the surface pressure, $\dot{\sigma}$ is the σ -velocity. With the exception of p_s , all variables are functions of x , y , σ , and t , and all horizontal derivatives are taken on sigma ($\sigma = \text{const.}$) surfaces.

For simplicity, in both formulations only the vertical component of relative vorticity is predicted.

4.3 Horizontal Discretization

Both the sigma and isentropic vertical coordinate models were developed using a periodic shallow water model (PSWM) (Fulton 2007) as a starting point. This model uses

a Fourier spectral representation of the state variables on a two-dimensional periodic f -plane domain. The spectral truncation limits in x and y are denoted M_x and M_y , and the periods are L_x and L_y , respectively. The inverse discrete Fourier transform (IDFT) of $f_\ell(x, y)$ in each layer ℓ is

$$f_\ell(x_j, y_k) = \sum_{m=-M_x}^{M_x} \sum_{n=-M_y}^{M_y} \hat{f}_{m,n} e^{2\pi i j m / N_x} e^{2\pi i k n / N_y}, \quad (4.16)$$

where $x_j = jL_x/N_x$ and $y_k = kL_y/N_y$ for $j = 0, 1, \dots, N_x - 1$ and $k = 0, 1, \dots, N_y - 1$. The corresponding discrete Fourier transform (DFT) is

$$\hat{f}_m(y_k) = \frac{1}{N_x} \sum_{j=0}^{N_x-1} f_\ell(x_j, y_k) e^{-2\pi i j m / N_x}, \quad (4.17)$$

$$\hat{f}_{m,n} = \frac{1}{N_y} \sum_{k=0}^{N_y-1} \hat{f}_m(y_k) e^{-2\pi i k n / N_y}. \quad (4.18)$$

By periodicity, it is also required that $f_\ell(x, y) = f_\ell(x + L_x, y)$, $f_\ell(x, y) = f_\ell(x, y + L_y)$, and $f_\ell(x, y) = f_\ell(x + L_x, y + L_y)$. The DFTs and IDFTs above are computed using the fast Fourier transform (FFT) routine of Temperton (1983c,b,a). In the model, linear terms and derivatives are computed in spectral space, and nonlinear terms and physical features such as the lateral sponge layer are done in physical space. All fields are transformed to physical space when vertical finite differences are taken (section 4.5).

4.4 Temporal discretization

The hydrostatic primitive equation models include a number of options for both explicit and semi-implicit time differencing. The explicit differencing schemes were taken directly from the base shallow water model, and include a simple forward scheme, second and third order Adams-Bashforth schemes, and a leapfrog scheme. The implicit schemes include a backward Euler, multi-step trapezoidal, and Adams-Moulton. The implicit methods have the potential for increased stability and larger time step (at the expense of distorting the fast gravity waves). However, since the advection velocity in hurricanes is large, it is not

clear whether a semi-implicit method would yield a faster simulation considering the added time to solve the implicit equation at each time step. At this point, the models are being run using the third order Adams-Bashforth explicit scheme (for which the time step is set by the CFL condition for the Lamb wave).

4.5 Vertical Discretization

A Charney-Phillips (C-P) grid (Charney and Phillips 1953) is used for both models which carries momentum and temperature at different levels. The Lorenz grid (Lorenz 1960) which carries momentum and potential temperature on the same level is not used because it has an extra degree of freedom in the vertical for potential temperature. Arakawa and Moorthi (1988) showed that a spurious amplification of short waves existed in the Lorenz grid when simulating baroclinic instability of an idealized midlatitude zonal jet.

4.5.1 Isentropic vertical coordinate

The variables are discretized using the conventions of Hsu and Arakawa (1990). Fig. 4.1 shows the staggering of variables on the C-P grid. The vertical grid is defined with a layer index ℓ between two half-layer indices $\ell + 1/2$ and $\ell - 1/2$. The layers and half-layers are indexed from the top of the atmosphere (TOA; $\ell = 1/2$) to the surface ($\ell = L + 1/2$). The half-layer potential temperature values are specified. The layer potential temperature values are computed using $\theta_\ell = \sqrt{\theta_{\ell+1/2}\theta_{\ell-1/2}}$ if $p_{1/2} \neq 0$ and $\theta_\ell = (1 + \kappa)\theta_{\ell+1/2}$ if $p_{1/2} = 0$. In a hydrostatic model the pseudodensity is used to obtain the balanced Montgomery potential by integrating (5). In the continuous model, this is done by the following procedure assuming $m(x, y, \theta)$ is known:

$$p(x, y, \theta) = p_t + \int_{\theta_t}^{\theta} m(x, y, \theta') d\theta', \quad (4.19)$$

$$\Pi(x, y, \theta) = c_p \left(\frac{p(x, y, \theta)}{p_0} \right)^\kappa, \quad (4.20)$$

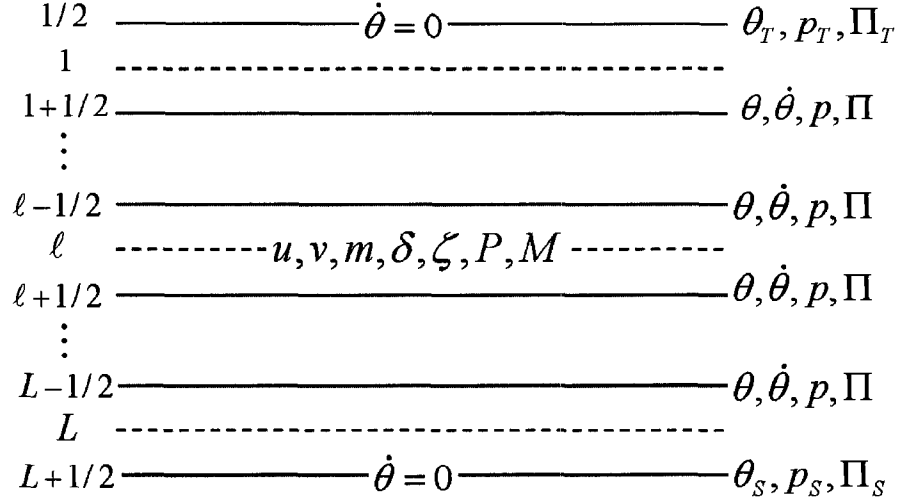


Figure 4.1: The staggering of variables on the Charney-Phillips grid for the isentropic vertical coordinate model.

$$\Phi(x, y, \theta) = \Phi(x, y, \theta_s) - \int_{\Pi_s}^{\Pi(x, y, \theta)} \theta d\Pi', \quad (4.21)$$

$$M(x, y, \theta) = \theta\Pi(x, y, \theta) + \Phi(x, y, \theta), \quad (4.22)$$

where (4.21) is the integral form of the hydrostatic equation ($\partial\Phi/\partial\Pi = -\theta$). The vertically discrete approximation to (4.19)-(4.22) is

$$p_{\ell+1/2} = p_{\ell-1/2} - (\theta_{\ell+1/2} - \theta_{\ell-1/2})\sigma_{\ell}, \quad (4.23)$$

$$\Pi_{\ell+1/2} = c_p \left(\frac{p_{\ell+1/2}}{p_0} \right)^{\kappa}, \quad (4.24)$$

$$p_{\ell} = \frac{1}{1 + \kappa} \frac{p_{\ell+1/2}^{1+\kappa} - p_{\ell-1/2}^{1+\kappa}}{p_{\ell+1/2} - p_{\ell-1/2}}, \quad (4.25)$$

$$\Pi_{\ell} = c_p \left(\frac{p_{\ell}}{p_0} \right)^{\kappa}, \quad (4.26)$$

$$\Phi_L = \Phi_{L+1/2} + \theta_L(\Pi_{L+1/2} - \Pi_L), \quad (4.27)$$

$$\Phi_\ell = \Phi_{\ell+1} + \theta_\ell(\Pi_\ell - \Pi_{\ell+1/2}) + \theta_{\ell+1}(\Pi_{\ell+1} - \Pi_{\ell+1/2}), \quad (4.28)$$

$$\Phi_{\ell-1/2} = \Phi_\ell + \theta_\ell(\Pi_\ell - \Pi_{\ell-1/2}), \quad (4.29)$$

$$M_\ell = \theta_\ell \Pi_\ell + \Phi_\ell, \quad (4.30)$$

where it is assumed that f_ℓ and $f_{\ell+1/2}$ are $f(x, y)$ arrays. Having summarized the hydrostatic calculation, we now summarize the entire vertically discrete model. The horizontal momentum equations are

$$\begin{aligned} \frac{\partial u_\ell}{\partial t} + \frac{1}{m_\ell} \left[(m\dot{\theta})_{\ell-1/2} \frac{u_{\ell-1/2} - u_\ell}{\theta_{\ell-1/2} - \theta_\ell} + (m\dot{\theta})_{\ell+1/2} \frac{u_\ell - u_{\ell+1/2}}{\theta_\ell - \theta_{\ell+1/2}} \right] - m_\ell P_\ell v_\ell \\ + \frac{\partial}{\partial x} (M_\ell + K_\ell) = F_{u\ell}, \end{aligned} \quad (4.31)$$

$$\begin{aligned} \frac{\partial v_\ell}{\partial t} + \frac{1}{m_\ell} \left[(m\dot{\theta})_{\ell-1/2} \frac{v_{\ell-1/2} - v_\ell}{\theta_{\ell-1/2} - \theta_\ell} + (m\dot{\theta})_{\ell+1/2} \frac{v_\ell - v_{\ell+1/2}}{\theta_\ell - \theta_{\ell+1/2}} \right] + m_\ell P_\ell u_\ell \\ + \frac{\partial}{\partial x} (M_\ell + K_\ell) = F_{v\ell}. \end{aligned} \quad (4.32)$$

The isentropic vorticity and divergence prognostic equations are

$$\begin{aligned} \frac{\partial \zeta_{\theta\ell}}{\partial t} + \frac{\partial}{\partial x} \left[\frac{1}{m_\ell} \left((m\dot{\theta})_{\ell-1/2} \frac{v_{\ell-1/2} - v_\ell}{\theta_{\ell-1/2} - \theta_\ell} + (m\dot{\theta})_{\ell+1/2} \frac{v_\ell - v_{\ell+1/2}}{\theta_\ell - \theta_{\ell+1/2}} \right) \right] \\ - \frac{\partial}{\partial y} \left[\frac{1}{m_\ell} \left((m\dot{\theta})_{\ell-1/2} \frac{u_{\ell-1/2} - u_\ell}{\theta_{\ell-1/2} - \theta_\ell} + (m\dot{\theta})_{\ell+1/2} \frac{u_\ell - u_{\ell+1/2}}{\theta_\ell - \theta_{\ell+1/2}} \right) \right] \\ + \frac{\partial(u_\ell m_\ell P_\ell)}{\partial x} + \frac{\partial(v_\ell m_\ell P_\ell)}{\partial y} = F_{\zeta\ell}, \end{aligned} \quad (4.33)$$

$$\begin{aligned} \frac{\partial \delta_{\theta\ell}}{\partial t} + \frac{\partial}{\partial x} \left[\frac{1}{m_\ell} \left((m\dot{\theta})_{\ell-1/2} \frac{u_{\ell-1/2} - u_\ell}{\theta_{\ell-1/2} - \theta_\ell} + (m\dot{\theta})_{\ell+1/2} \frac{u_\ell - u_{\ell+1/2}}{\theta_\ell - \theta_{\ell+1/2}} \right) \right] \\ + \frac{\partial}{\partial y} \left[\frac{1}{m_\ell} \left((m\dot{\theta})_{\ell-1/2} \frac{v_{\ell-1/2} - v_\ell}{\theta_{\ell-1/2} - \theta_\ell} + (m\dot{\theta})_{\ell+1/2} \frac{v_\ell - v_{\ell+1/2}}{\theta_\ell - \theta_{\ell+1/2}} \right) \right] \\ + \frac{\partial(u_\ell m_\ell P_\ell)}{\partial y} + \frac{\partial(v_\ell m_\ell P_\ell)}{\partial x} + \nabla^2 (K_\ell + M_\ell) = F_{\delta\ell}. \end{aligned} \quad (4.34)$$

The hydrostatic equations are

$$M_L - \Phi_s = \theta_L \Pi_{L+1/2}, \quad (4.35)$$

$$\frac{M_\ell - M_{\ell+1}}{\theta_\ell - \theta_{\ell+1}} = \Pi_{\ell+1/2}. \quad (4.36)$$

The continuity and thermodynamic equations are

$$\frac{\partial m_\ell}{\partial t} + \frac{\partial(m_\ell u_\ell)}{\partial x} + \frac{\partial(m_\ell v_\ell)}{\partial y} + \frac{(m\dot{\theta})_{\ell-1/2} - (m\dot{\theta})_{\ell+1/2}}{\theta_{\ell-1/2} - \theta_{\ell+1/2}} = 0, \quad (4.37)$$

$$\dot{\theta}_{\ell+1/2} = \frac{Q_{\ell+1/2}}{\Pi_{\ell+1/2}}. \quad (4.38)$$

Finally, the upper and lower boundary conditions are

$$(m\dot{\theta})_{1/2} = 0, \quad (4.39)$$

$$(m\dot{\theta})_{L+1/2} = 0. \quad (4.40)$$

4.5.2 *Sigma vertical coordinate*

The σ -coordinate model is also discretized on a C-P grid (Fig. 4.2). The vertical grid is defined with a layer index ℓ between two half-layer indices $\ell + 1/2$ and $\ell - 1/2$. The layers and half-layers are indexed from the top of the atmosphere (TOA; $\ell = 1/2$) to the surface ($\ell = L + 1/2$). The potential temperature θ is predicted at the half-layers, while the momentum or vorticity and divergence are predicted at the layers.

In the continuous model, the hydrostatic integration is done by first obtaining the specific volume knowing θ using the ideal gas law,

$$\alpha(x, y, \sigma) = \frac{R\theta(x, y, \sigma)}{p(x, y)} \left(\frac{p(x, y)}{p_0} \right)^\kappa, \quad (4.41)$$

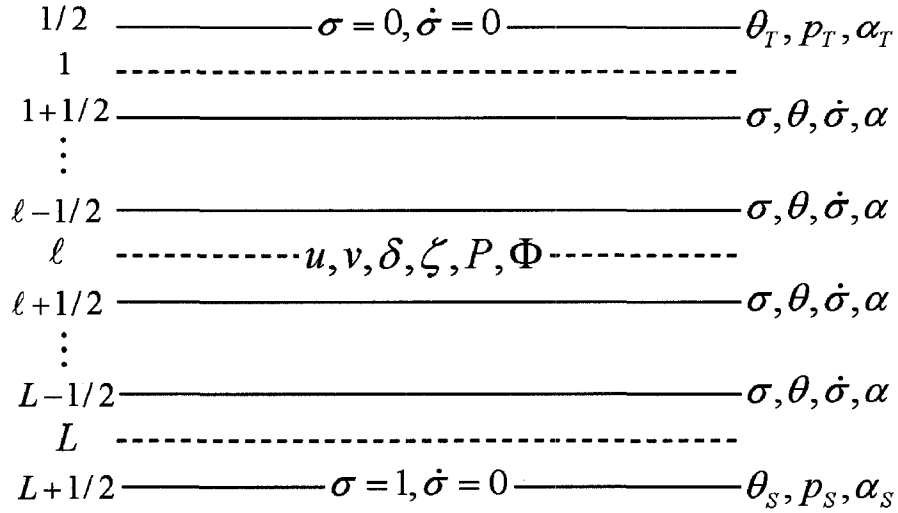


Figure 4.2: The staggering of variables on the Charney-Phillips grid for the sigma vertical coordinate model.

where $p(x, y) = \sigma(p_s(x, y) - p_t) + p_t$, and then integrating the hydrostatic equation,

$$\Phi(x, y, \sigma) - \Phi(x, y, 1) = \int_1^\sigma -p_s(x, y)\alpha(x, y, \sigma) d\sigma. \quad (4.42)$$

The discrete finite difference approximation to (4.41)-(4.42) is

$$\alpha_{\ell+1/2} = \frac{R\theta_{\ell+1/2}}{p_{\ell+1/2}} \left(\frac{p_{\ell+1/2}}{p_0} \right)^\kappa, \quad (4.43)$$

$$\Phi_L = \Phi_{L+1/2} - p_s \alpha_{L+1/2} (\sigma_L - \sigma_{L+1/2}), \quad (4.44)$$

$$\Phi_\ell = \Phi_{\ell+1} - p_s \alpha_{\ell+1/2} (\sigma_\ell - \sigma_{\ell+1}). \quad (4.45)$$

The surface pressure $p_s(x, y)$ changes according to

$$\frac{\partial p_s}{\partial t} = - \int_0^1 \left(\frac{\partial(p_s u)}{\partial x} + \frac{\partial(p_s v)}{\partial y} \right) d\sigma, \quad (4.46)$$

from which $\dot{\sigma}(x, y, \sigma)$ is determined by

$$p_s \dot{\sigma} = \sigma \frac{\partial p_s}{\partial t} - \int_0^\sigma \left(\frac{\partial(p_s u)}{\partial x} + \frac{\partial(p_s v)}{\partial y} \right) d\sigma'. \quad (4.47)$$

The discrete approximation to (4.46)-(4.47) is

$$\frac{\partial p_s}{\partial t} = \sum_{\ell=1}^L \left(- \left[\frac{\partial(p_s u_\ell)}{\partial x} + \frac{\partial(p_s v_\ell)}{\partial y} \right] (\sigma_{\ell+1/2} - \sigma_{\ell-1/2}) \right), \quad (4.48)$$

$$\dot{\sigma}_{\ell+1/2} = \sigma_{\ell+1/2} \frac{\partial p_s}{\partial t} - \left[\frac{\partial(p_s u_\ell)}{\partial x} + \frac{\partial(p_s v_\ell)}{\partial y} \right] (\sigma_{\ell+1/2} - \sigma_{\ell-1/2}). \quad (4.49)$$

Having summarized the hydrostatic integration, the entire vertically discrete model is shown. The horizontal momentum equations are

$$\frac{\partial u_\ell}{\partial t} + \dot{\sigma}_\ell \frac{u_{\ell-1/2} - u_{\ell+1/2}}{\sigma_{\ell-1/2} - \sigma_{\ell+1/2}} - \eta_\ell v_\ell + \frac{\partial}{\partial x} (\Phi_\ell + K_\ell) + \sigma_\ell \alpha_\ell \frac{\partial p_s}{\partial x} = F_{u\ell}, \quad (4.50)$$

$$\frac{\partial v_\ell}{\partial t} + \dot{\sigma}_\ell \frac{v_{\ell-1/2} - v_{\ell+1/2}}{\sigma_{\ell-1/2} - \sigma_{\ell+1/2}} + \eta_\ell u_\ell + \frac{\partial}{\partial y} (\Phi_\ell + K_\ell) + \sigma_\ell \alpha_\ell \frac{\partial p_s}{\partial y} = F_{v\ell}. \quad (4.51)$$

The vorticity-divergence equations are

$$\begin{aligned} \frac{\partial \zeta_{\sigma\ell}}{\partial t} + \frac{\partial}{\partial x} \left(\dot{\sigma}_\ell \frac{v_{\ell-1/2} - v_{\ell+1/2}}{\sigma_{\ell-1/2} - \sigma_{\ell+1/2}} \right) - \frac{\partial}{\partial y} \left(\dot{\sigma}_\ell \frac{u_{\ell-1/2} - u_{\ell+1/2}}{\sigma_{\ell-1/2} - \sigma_{\ell+1/2}} \right) + \frac{\partial(\eta_{\sigma\ell} u_\ell)}{\partial x} \\ + \frac{\partial(\eta_{\sigma\ell} v_\ell)}{\partial y} + \sigma \left(\frac{\partial \alpha_\ell}{\partial x} \frac{\partial p_s}{\partial y} - \frac{\partial \alpha_\ell}{\partial y} \frac{\partial p_s}{\partial x} \right) = F_{\zeta\ell}, \end{aligned} \quad (4.52)$$

$$\begin{aligned} \frac{\partial \delta_{\sigma\ell}}{\partial t} + \frac{\partial}{\partial x} \left(\dot{\sigma}_\ell \frac{u_{\ell-1/2} - u_{\ell+1/2}}{\sigma_{\ell-1/2} - \sigma_{\ell+1/2}} \right) + \frac{\partial}{\partial y} \left(\dot{\sigma}_\ell \frac{v_{\ell-1/2} - v_{\ell+1/2}}{\sigma_{\ell-1/2} - \sigma_{\ell+1/2}} \right) + \frac{\partial(\eta_{\sigma\ell} u_\ell)}{\partial y} \\ - \frac{\partial(\eta_{\sigma\ell} v_\ell)}{\partial x} + \nabla^2 (\Phi_\ell + K_\ell) + \sigma \alpha \nabla^2 p_s \\ + \sigma_\ell \left(\frac{\partial \alpha_\ell}{\partial x} \frac{\partial p_s}{\partial x} + \frac{\partial \alpha_\ell}{\partial y} \frac{\partial p_s}{\partial y} \right) = F_{\delta\ell}. \end{aligned} \quad (4.53)$$

The hydrostatic equations are

$$\frac{\Phi_L - \Phi_{L+1/2}}{\sigma_L - \sigma_{L+1/2}} = -p_s \alpha_{L+1/2}, \quad (4.54)$$

$$\frac{\Phi_\ell - \Phi_{\ell+1}}{\sigma_\ell - \sigma_{\ell+1}} = -p_s \alpha_{\ell+1/2}, \quad (4.55)$$

and the continuity and thermodynamic equations are

$$\frac{\partial p_s}{\partial t} + \frac{\partial(p_s u_\ell)}{\partial x} + \frac{\partial(p_s v_\ell)}{\partial y} + \frac{(p_s \dot{\sigma}_{\ell-1/2} - p_s \dot{\sigma}_{\ell+1/2})}{\sigma_{\ell-1/2} - \sigma_{\ell+1/2}} = 0, \quad (4.56)$$

$$\frac{\partial \theta_{\ell+1/2}}{\partial t} + u_{\ell+1/2} \frac{\partial \theta_{\ell+1/2}}{\partial x} + v_{\ell+1/2} \frac{\partial \theta_{\ell+1/2}}{\partial y} + \dot{\sigma}_{\ell+1/2} \frac{\theta_\ell - \theta_{\ell+1}}{\sigma_\ell - \sigma_{\ell+1}} = Q_{\ell+1/2}. \quad (4.57)$$

Finally, the upper and lower boundary conditions are

$$(p_s \dot{\sigma})_{1/2} = 0, \quad (4.58)$$

$$(p_s \dot{\sigma})_{L+1/2} = 0. \quad (4.59)$$

4.6 Additional Features of the Models

4.6.1 Mass restoration

The isentropic vertical coordinate model includes a mass restoration routine that is exactly mass conserving when time is continuous. The user specifies a minimum layer pressure. If the model tends to produce a pressure lower than this threshold, the layer pressure is set to the user-specified value and mass is evenly redistributed in a vertical column at the horizontal grid point.

4.6.2 Damping

Both models include both explicit diffusion ∇^{2m} damping and a sponge layer at the lateral boundaries. There are multiple options for the sponge shape function and either Rayleigh ($-\beta(f - f^*)$, where f^* is specified) or Laplacian ∇^{2m} damping may be used. The sponge layer is necessary to damp outward propagating internal gravity waves excited in

the domain interior, especially in light of the periodic boundary conditions. The damping terms are included in the F terms in (4.1)-(4.4), and (4.9)-(4.12).

4.6.3 *Surface friction*

The isentropic coordinate model includes surface friction in the form of a bulk drag formula (Hsu and Arakawa 1990). A pressure depth of the boundary layer is specified and the friction force is set constant in each isentropic layer within the boundary layer. Surface friction has not yet been added to σ -coordinate model.

4.7 Initialization

4.7.1 *Isentropic vertical coordinate model*

In momentum form, the model is initialized by specifying $u(x, y, \theta)$, $v(x, y, \theta)$, and $m(x, y, \theta)$. In vorticity-divergence form, the model is initialized by specifying $\zeta(x, y, \theta)$, $\delta(x, y, \theta)$, and $m(x, y, \theta)$. A particularly useful initialization is using the nonlinear balance equation in conjunction with the hydrostatic equation. By using this method one can specify the wind field (either through ζ or a nondivergent u and v) and obtain the balanced mass field. In isentropic coordinates, the nonlinear balance and hydrostatic equations are

$$2 \left[\frac{\partial^2 \psi}{\partial x^2} \frac{\partial^2 \psi}{\partial y^2} - \left(\frac{\partial^2 \psi}{\partial x \partial y} \right)^2 \right] + f \left(\frac{\partial^2 \psi}{\partial x^2} + \frac{\partial^2 \psi}{\partial y^2} \right) = \nabla^2 M', \quad (4.60)$$

$$\frac{\partial M}{\partial \theta} = \Pi, \quad (4.61)$$

where $u = -\partial\psi/\partial y$, $v = \partial\psi/\partial x$ and $\zeta_\theta = \nabla^2\psi$. Equations (4.60) and (4.61) can be solved to obtain the balanced Montgomery potential deviation, $M'(x, y, \theta)$, for a given three dimensional nondivergent flow. The total Montgomery potential is then $M(x, y, \theta) = \bar{M}(\theta) + M'(x, y, \theta)$, where $\bar{M}(\theta)$ is the background potential. Knowing $M(x, y, \theta)$, the corresponding balanced mass field, $m(x, y, \theta)$, is obtained by

$$m = -\frac{p}{\kappa\Pi} \frac{\partial^2 M}{\partial\theta^2}. \quad (4.62)$$

In the numerical procedure, first ζ_ℓ is specified. Second, $\nabla^2\psi_\ell = \zeta_\ell$ is solved to obtain ψ_ℓ . Third, the nonlinear balance equation $\nabla^2 M'_\ell = C$ is solved, where C is known. Fourth, M'_ℓ is added to the background Montgomery potential to obtain M_ℓ . Finally, the new pseudodensity is calculated by the following sequential procedure:

$$\Pi_{1/2} = c_p \left(\frac{p_t}{p_s} \right)^\kappa, \quad (4.63)$$

$$\Pi_{\ell+1/2} = \frac{M_\ell - M_{\ell+1}}{\theta_\ell - \theta_{\ell+1}}, \quad (4.64)$$

$$\Pi_{L+1/2} = \frac{M_L - \Phi_s}{\theta_L}, \quad (4.65)$$

$$p_{\ell+1/2} = p_0 \left(\frac{\Pi_{\ell+1/2}}{c_p} \right)^{\frac{1}{\kappa}}, \quad (4.66)$$

$$p_\ell = \frac{1}{1 + \kappa} \frac{p_{\ell+1/2}^{1+\kappa} - p_{\ell-1/2}^{1+\kappa}}{p_{\ell+1/2} - p_{\ell-1/2}}, \quad (4.67)$$

$$\Pi_\ell = c_p \left(\frac{p_\ell}{p_0} \right)^\kappa, \quad (4.68)$$

$$\left(\frac{\partial\Pi}{\partial\theta} \right)_\ell = \frac{\Pi_{\ell+1/2} - \Pi_{\ell-1/2}}{\theta_{\ell+1/2} - \theta_{\ell-1/2}}, \quad (4.69)$$

$$\sigma_\ell = - \left(\frac{\partial\Pi}{\partial\theta} \right)_\ell \frac{p_\ell}{\kappa\Pi_\ell}. \quad (4.70)$$

4.7.2 *Sigma vertical coordinate model*

In momentum form, the sigma coordinate model is initialized by specifying $u(x, y, \sigma)$, $v(x, y, \sigma)$, $\theta(x, y, \sigma)$, and $p_s(x, y)$. In vorticity-divergence form, the model is initialized by specifying $\zeta(x, y, \theta)$, $\delta(x, y, \theta)$, $\theta(x, y, \sigma)$, and $p_s(x, y)$. A balance initialization is also included in the σ -coordinate model based from Sundqvist (1975) and Kurihara and Bender (1980) that determines $\theta(x, y, \sigma)$ and $p_s(x, y)$ from known nondivergent $u(x, y, \sigma)$ and $v(x, y, \sigma)$, or $\zeta(x, y, \sigma)$.

The nonlinear balance equation

$$2 \left[\frac{\partial^2 \psi}{\partial x^2} \frac{\partial^2 \psi}{\partial y^2} - \left(\frac{\partial^2 \psi}{\partial x \partial y} \right)^2 \right] + f \nabla^2 \psi = \nabla^2 \Phi + \nabla \cdot (\sigma \alpha \nabla p_s). \quad (4.71)$$

is obtained by setting $\partial \delta_\sigma / \partial t$ and $\dot{\sigma}$ to zero in (4.53). Since p_s is only a function of the x and y , this equation can be solved using

$$2 \left[\frac{\partial^2 \psi}{\partial x^2} \frac{\partial^2 \psi}{\partial y^2} - \left(\frac{\partial^2 \psi}{\partial x \partial y} \right)^2 \right] + f \nabla^2 \psi = \begin{cases} \nabla \cdot (\sigma \alpha_s \nabla p_s) & \sigma = 1 \\ \nabla^2 \Phi + \nabla \cdot (\sigma \alpha \nabla p_s) & \sigma < 1. \end{cases} \quad (4.72)$$

Generally speaking, (4.72) is solved by an overrelaxation method. Zhu et al. (2001) recommends that the equation be first solved for p_s at $\sigma = 1$ assuming a surface temperature field, and then solved for Φ and α at $\sigma < 1$. The balance initialization in the current model is as follows: (a) hold $\alpha_s(x, y)$ fixed, and solve (4.72) for $p_s(x, y)$ at $\sigma = 1$, (b) use a horizontally homogenous background $\alpha(x, y, \sigma)$ profile and solve (4.72) for $\Phi(x, y, \sigma)$ for $\sigma < 1$, (c) enforce the hydrostatic condition, $\partial \Phi / \partial \sigma = -p_s \alpha$, to obtain an updated $\alpha(x, y, \sigma)$, (d) obtain an updated $\Phi(x, y, \sigma)$ using the new $\alpha(x, y, \sigma)$ in (4.72) for $\sigma < 1$, and (e) repeat steps (c) and (d) until convergence, i.e., $\Phi(x, y, \sigma)$ and $\alpha(x, y, \sigma)$ are not changing. Once this is done $\theta(x, y, \sigma)$ may be obtained using the ideal gas law, completing the initialization for the prognostic variables. This balance initialization has been incorporated into the model, but it has not yet been fully tested.

4.8 Evaluation Tests: Isentropic Vertical Coordinate Model

The results of some verification and validation tests are presented in this section. We define verification as ensuring that various parts of the model accomplish their designed purpose. On the other hand, scientific validation would be the evaluation of the model predictions against observations and other models; this is accomplished over long time periods as the model is used to simulate a variety of different meteorological phenomena. The evaluation tests are broadly consistent with those recommended by Pielke (2002) for verification and validation of mesoscale models.

4.8.1 Initialization: comparison to analytic solution

The first task is to ensure that the balance initialization works correctly for a three dimensional vortex. This is done by comparing the analytical solution for the pseudodensity of a simple axisymmetric vortex in gradient and hydrostatic balance to the output of the model nonlinear balance routine. Consider the axisymmetric vorticity and tangential winds for a Rankine vortex which decays vertically with structure $f(\theta) = \exp(-a(\theta - \theta_s)/(\theta_t - \theta_s))$ (where a is a decay constant, θ_s is the surface potential temperature and θ_t is the TOA potential temperature):

$$\bar{\zeta}(r, \theta) = \begin{cases} \zeta_0 f(\theta) & 0 \leq r \leq r_m \\ 0 & r_m \leq r \leq \infty, \end{cases} \quad (4.73)$$

$$r\bar{v}(r, \theta) = \begin{cases} \zeta_0 r^2 f(\theta)/2 & 0 \leq r \leq r_m \\ \zeta_0 r_m^2 f(\theta)/2 & r_m \leq r \leq \infty, \end{cases} \quad (4.74)$$

Solving the gradient wind equation ($v^2/r + fv = \partial M'/\partial r$) for the analytic Montgomery potential deviation, we obtain

$$M'(r, \theta) = \begin{cases} \frac{\zeta_0 r^2}{8} f(\theta) (2f + \zeta_0 f(\theta)) & 0 \leq r \leq r_m \\ \frac{\zeta_0 r_m^2}{8} f(\theta) (4f \ln r - \frac{\zeta_0 r_m^2}{r^2} f(\theta)) + C_0 & r_m \leq r \leq \infty, \end{cases} \quad (4.75)$$

where the constant of integration $C_0 = (\zeta_0 r_m^2 / 4) f(\theta) [f(1 - 2 \ln r_m) + \zeta_0 f(\theta)]$.

In Fig. 4.3, a side-by-side comparison of the azimuthal mean analytic $\bar{v}(r, \theta)$ and $M'(r, \theta)$ and the numerical model nonlinear balance initialization is shown. The initial parameters in the model are $n_x = n_y = 100$, $n_l = 10$ over a 600 km square domain with $\theta_s = 300$ K, $\theta_t = 360$ K, $a = 2.5$, $f = 0.00005$ s⁻¹, $\zeta_0 = 0.0005$ s⁻¹, and $r_m = 50$ km. The Montgomery potential deviation from the numerical balance initialization is nearly identical to the analytic solution. Thus, the balance initialization is verified to work correctly.

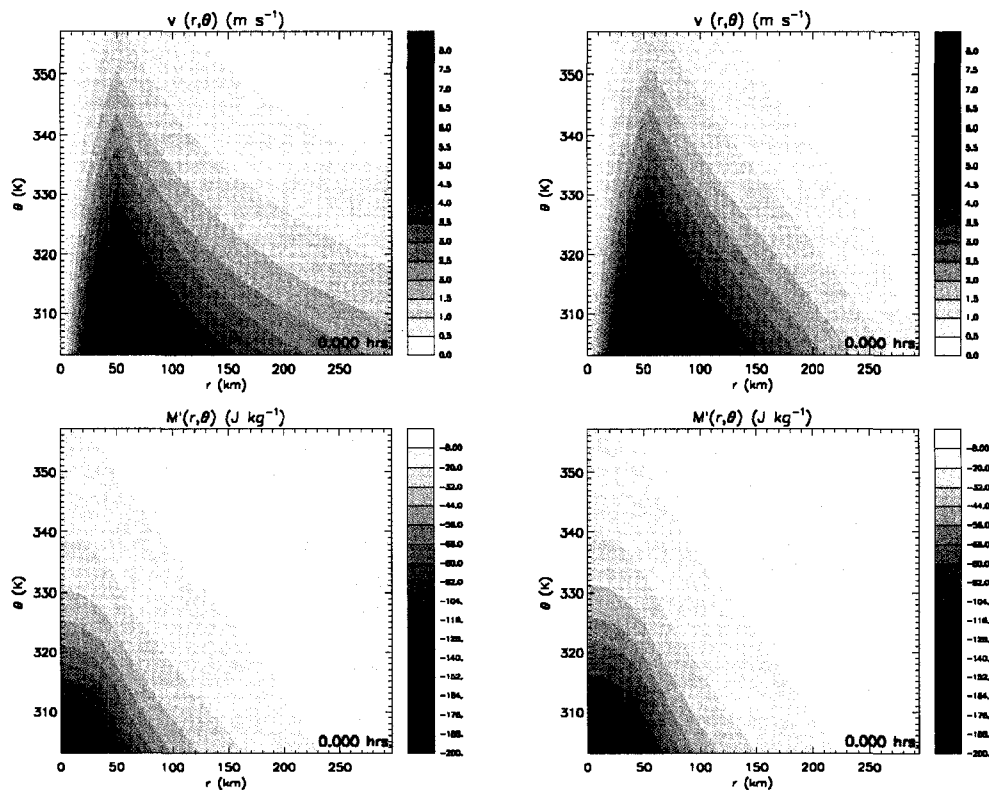


Figure 4.3: [top panels] The initial wind field $v(r, \theta)$ for the analytic Rankine vortex (left) and the initial condition of the model (right). [bottom panels] Comparison of the analytic $M'(r, \theta)$ (left) to the nonlinear balance initialization of the model (right)

4.8.2 Gradient adjustment of an axisymmetric vortex

An important physical process that any primitive equation model should simulate is balance adjustment. This is often called geostrophic adjustment, but does not necessarily have to be a linear balance adjustment. Here we provide evidence that the present model can simulate the gradient adjustment process for some ideal three-dimensional baroclinic vortices with unbalanced mass fields.

Gradient adjustment in axisymmetric vortices has previously been studied by Schubert et al. (1980), who examined conditions in which cloud-cluster heating energy is partitioned into the balanced flow and inertia-gravity waves. In a simpler context, using a linearized system of the shallow water equations (W. H. Schubert dynamics notes and Holton 1992), the conditions for which an initially unbalanced flow adjusts into geostrophic balance were determined. Let b be the horizontal scale of the disturbance, and c/f be the Rossby radius of deformation. If $b \gg c/f$ (the scale of the initial disturbance is much larger than the Rossby radius) the pressure hardly changes and the *wind adjusts to the pressure*. On the other hand, if $b \ll c/f$, the wind hardly changes and the *pressure adjusts to the wind*. Since the adiabatic isentropic model is the natural extension to the shallow water equations, we expect that these conditions may hold true for gradient adjustment of a baroclinic vortex in the isentropic model. However, for the case of gradient adjustment for a rapidly rotating vortex, f must be replaced by vortex inertial stability parameter $I = [(f + \bar{\zeta})(f + 2\bar{v}/r)]^{1/2}$ (Shapiro and Willoughby 1982; Shapiro and Montgomery 1993). Therefore, the vortex Rossby radius of deformation is c/I , and as we will see, f is insignificant in this quantity for realistic rapidly rotating hurricanes.

The initial vortex is the same Rankine vortex defined in (4.75) with $\zeta_0 = 0.0005 \text{ s}^{-1}$ and $r_m = 50 \text{ km}$. A smooth transition zone is included in the initial condition so that the relative vorticity decays smoothly to zero between $r = 50$ and $r = 60 \text{ km}$. The background pseudodensity field is initialized using $m(\theta) = m_0 \exp(-a(\theta - \theta_s)/(\theta_t - \theta_s))$, where $a = 2.5$, $\theta_s = 300 \text{ K}$, $\theta_t = 360 \text{ K}$, and $m_0 = 4000 \text{ Pa K}^{-1}$. Using $\bar{\zeta} = \zeta_0 = 0.0005 \text{ s}^{-1}$ and estimating

$2\bar{v}/r = 0.00032 \text{ s}^{-1}$ (note that in reality this quantity should be averaged over the entire storm, but we have estimated it as the mean velocity over the whole atmosphere at the radius of maximum wind, i.e., $\bar{v} = 4 \text{ m s}^{-1}$ at $r = 50 \text{ km}$), we obtain $I = 0.000297 \text{ s}^{-1}$. Hence for this vortex, $I \gg f$. The vortex Rossby radius of deformation is then $c/I \approx 169 \text{ km}$ (using a typical internal gravity wave phase speed $c = 50 \text{ m s}^{-1}$). The vortex scale is $b = 50 \text{ km}$, so $b < c/I$ and it is expected that the wind would hardly change and the mass would adjust to the wind.

In Fig. 4.4, side-by-side plots of the azimuthal mean $\bar{v}(r, \theta)$ and $M'(r, \theta)$ are shown in early phases of the gradient adjustment simulation. Note that the wind field is hardly changing, and the Montgomery potential (mass field) is adjusting to the wind.

4.8.3 Unstable baroclinic vortex evolution

The model was run with an initial condition of an unstable baroclinic vortex, which shall be referred to as a potential vorticity (PV) hollow tower. The radial reversal of PV satisfies the Charney-Stern necessary condition for combined barotropic-baroclinic instability (see Montgomery and Shapiro (1995) for a discussion of this theorem as it relates to rapidly rotating vortices). Here we simulate the dry, adiabatic rearrangement PV due to dynamic instability of a hurricane-like PV hollow tower. The initial condition for relative vorticity is separable: $\bar{\zeta}(r, 0, \theta) = \bar{\zeta}(r, 0)f(\theta)$, where

$$\bar{\zeta}(r, 0) = \begin{cases} \zeta_1 & 0 \leq r \leq r_1 \\ \zeta_1 S\left(\frac{r-r_1}{r_2-r_1}\right) + \zeta_2 S\left(\frac{r_2-r}{r_2-r_1}\right) & r_1 \leq r \leq r_2 \\ \zeta_2 & r_2 \leq r \leq r_3, \\ \zeta_2 S\left(\frac{r-r_3}{r_4-r_3}\right) + \zeta_3 S\left(\frac{r_4-r}{r_4-r_3}\right) & r_3 \leq r \leq r_4 \\ \zeta_3 & r_4 \leq r \leq \infty \end{cases} \quad (4.76)$$

and $f(\theta) = \exp[(\theta - \theta_{\text{ref}})^2/(2\sigma)]$. Here, $\zeta_1 = 0.0$ and $\zeta = 0.001 \text{ s}^{-1}$, $r_1, r_2, r_3, r_4 = 30, 40, 50, 60 \text{ km}$, $S(s) = 1 - 3s^2 + 2s^3$ is a cubic Hermite shape function that provides

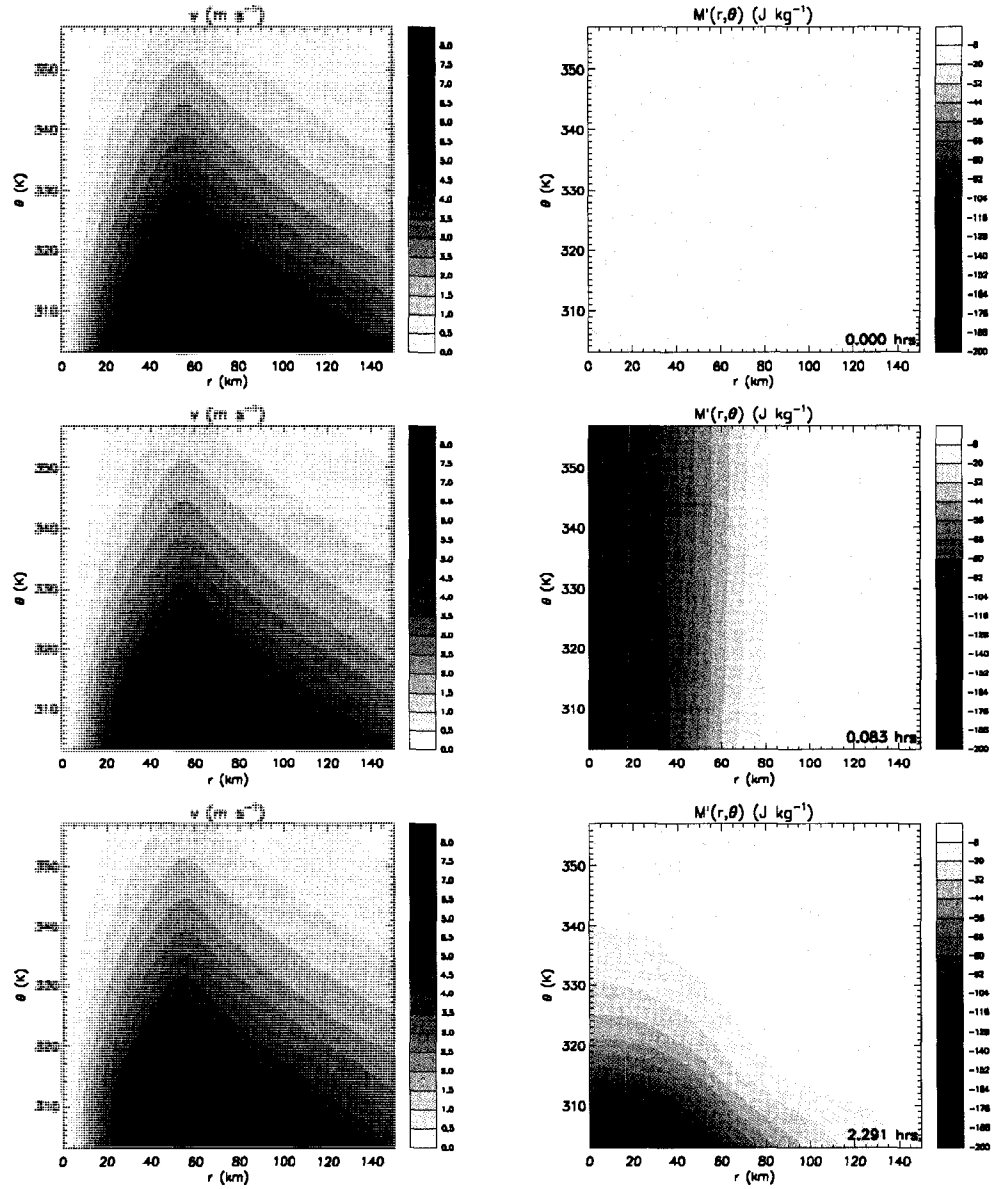


Figure 4.4: [left panels] The evolution of the azimuthal mean wind field $\bar{v}(r, \theta)$ and [right panels] the evolution of the azimuthal mean montgomery potential deviation $M'(r, \theta)$ for the gradient adjustment simulation.

smooth transition zones, $\theta_{\text{ref}} = 305$ K, and $\sigma = 5$ K below θ_{ref} and $\sigma = 15$ K above θ_{ref} . The background pseudodensity $m(\theta) = m_0 \exp(-a(\theta - \theta_s)/(\theta_t - \theta_s))$, with $m_0 = 4000$ Pa K^{-1} and $a = 2.5$. The balance initialization is used to determined the balanced mass field due

to the baroclinic vortex. The solution is obtained numerically using the vorticity-divergence formulation with $\zeta(x, y, \theta, 0)$ and $m(x, y, \theta, 0)$ defined above, and $\delta(x, y, \theta, 0)$ equal to zero. An unbalanced, weak perturbation is added the basic state vorticity at each isentropic layer of the form $\zeta'(r, \phi, \theta) = \zeta'(r, \phi)f(\theta)$ where

$$\zeta'(r, \phi, 0) = \zeta_{amp} \sum_{m=1}^{12} \cos(m\phi + \phi_m) \times \begin{cases} 0 & 0 \leq r \leq r_1, \\ S\left(\frac{r_2-r}{r_2-r_1}\right) & r_1 \leq r \leq r_2, \\ 1 & r_2 \leq r \leq r_3, \\ S\left(\frac{r-r_3}{r_4-r_3}\right) & r_3 \leq r \leq r_4, \\ 0 & r_4 \leq r < \infty, \end{cases} \quad (4.77)$$

where $\zeta_{amp} = 1.0 \times 10^{-5} \text{ s}^{-1}$ and $f(\theta)$ is defined as above. The impulse is expected to arise from a wide spectrum of background convection. The simulation was done on an f -plane with $f = 5 \times 10^{-5} \text{ s}^{-1}$.

The solution is obtained on a double periodic domain in the horizontal with 250×250 points, and 8 isentropic layers between $\theta = 300, 307.5, 315, \dots, 360$ K. Ordinary diffusion was used with $\nu = 50 \text{ m}^2 \text{ s}^{-1}$ on ζ , δ and m primarily for numerical damping associated with the grid resolution. Since internal gravity waves may be generated during PV mixing, the sponge layer was active near the lateral boundaries with Laplacian damping and e -folding time of 0.5 h for the shortest wave. The top and bottom boundaries were rigid. The purpose of this experiment was to isolate the advective dynamics of PV mixing; as such the evolution is nearly conservative (aside from numerical diffusion) and adiabatic. Surface friction was not used.

The adiabatic evolution the PV hollow tower is shown in Figs. 4.5–4.8 progressing from $t = 0 - 48$ h. In each plot, 4 panels are shown. The top panels depict the azimuthal mean PV and tangential velocity, and the bottom panels depict θ slices of PV near the surface and at upper levels. In Fig. 4.5 (top left panel), note the initially vertical erect PV hollow tower due to the baroclinic vortex. Also note the background PV that increases due

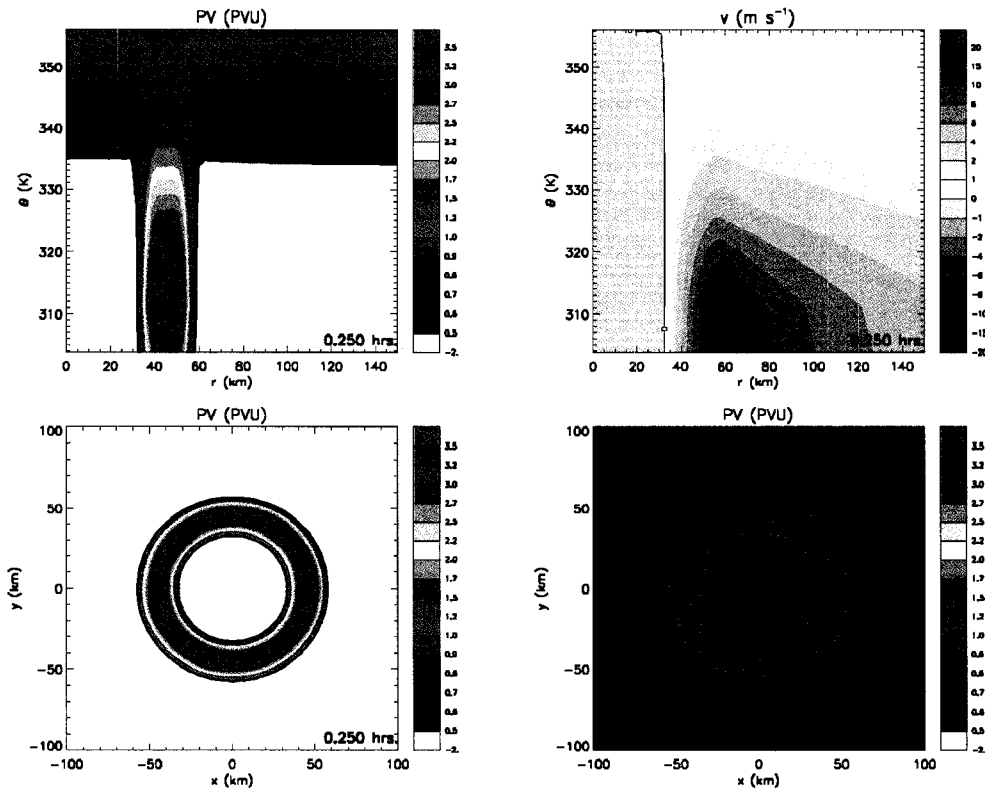


Figure 4.5: The azimuthal mean PV (PVU) [top left panel], the azimuthal mean tangential velocity (m s^{-1}) [top right panel], PV (PVU) on the $\theta = 304$ K surface [bottom left panel], and PV (PVU) on the $\theta = 341$ K surface [bottom right panel]. All fields are shown at $t = 0.25$ h.

to greater static stability near the tropopause in the presence of background rotation.

Progressing to $t = 12$ h in Fig. 4.6, note that the PV ring on of the $\theta = 304$ K surface has become dynamically unstable and is breaking down at azimuthal wavenumber $m = 3$. The upper level PV ring has not changed. The ring breakdown at lower levels has cause the PV tower to tilt inward slightly (top left panel). Moving forward to $t = 24$ h in Fig. 4.7, the low level PV ring has broken down completely and PV is being mixed into the eye, while the upper level PV ring is still unchanged. The PV hollow tower is now tilting more significantly below $\theta = 325$ K, but is vertically erect above it. The PV mixing at low levels causes the tangential velocity to increase at lower radii, changing the radial profiles from U-shaped to V-shaped. Finally, at $t = 48$ h (Fig. 4.8), the low level PV ring has mixed

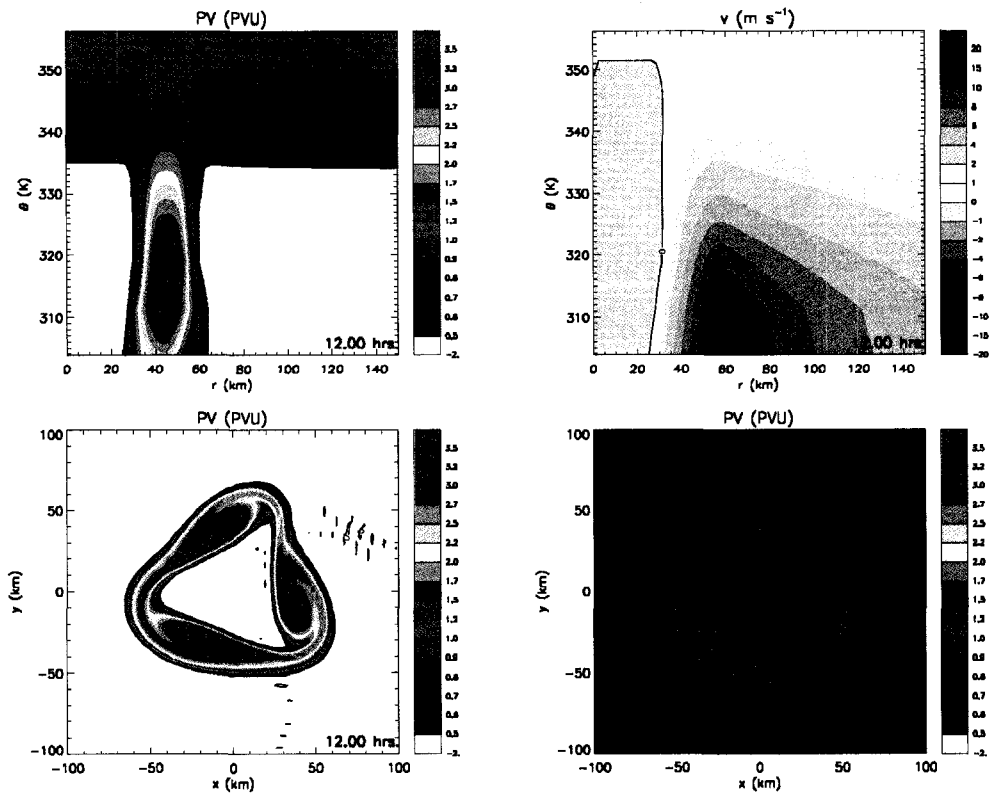


Figure 4.6: The azimuthal mean PV (PVU) [top left panel], the azimuthal mean tangential velocity (m s^{-1}) [top right panel], PV (PVU) on the $\theta = 304$ K surface [bottom left panel], and PV (PVU) on the $\theta = 341$ K surface [bottom right panel]. All fields are shown at $t = 12$ h.

from an annulus into a near monopole. The upper level PV ring is still similar to the initial condition. The PV hollow tower now slopes outward with height, at approximately 50 km per 30 K, or 1.67 km K^{-1} . The tower is now hollow above $\theta = 317$ K and monopolar below $\theta = 317$ K. A “PV bridge” exists at $\theta = 310$ K across the eye. The PV bridge has previously been simulated in a high resolution (2 km), full-physics nonhydrostatic model simulation of Hurricane Andrew (1992) using the PSU-NCAR MM5 model (Yau et al. 2004). We have simulated a similar structure in an idealized model with no physics, adiabatic, and nearly conservative dynamics. A side-by-side comparison of the azimuthal mean PV in our simulation and the Yau et al. (2004) azimuthal mean PV simulated in Hurricane Andrew (1992) are shown in Fig 4.9.

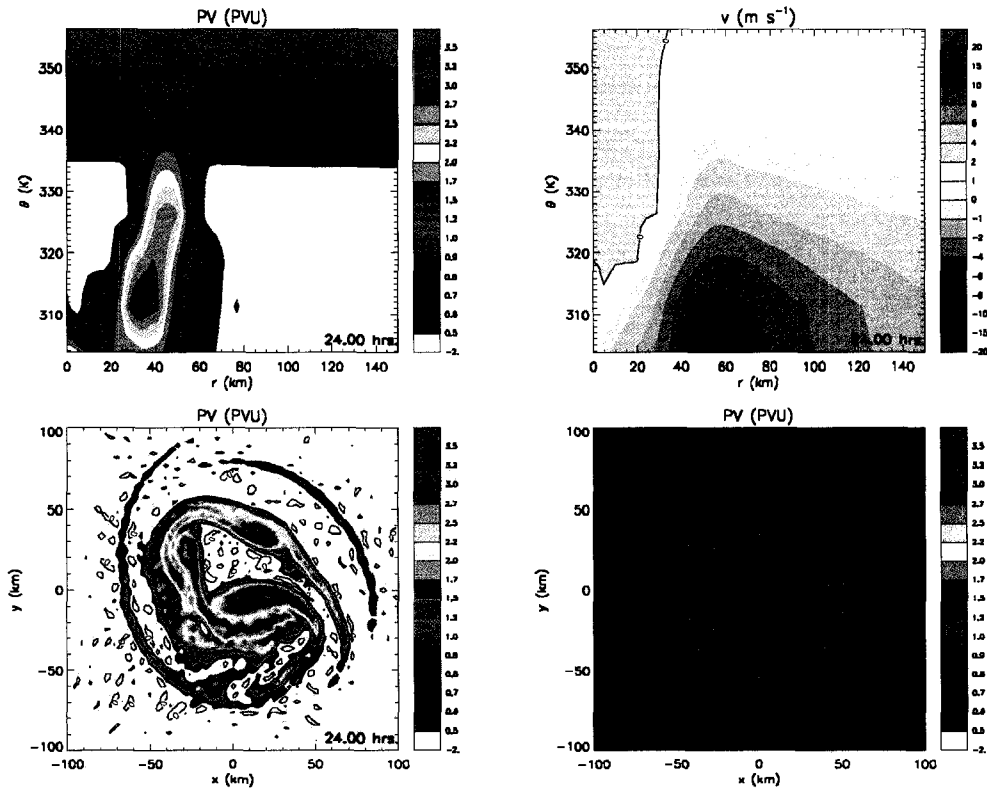


Figure 4.7: The azimuthal mean PV (PVU) [top left panel], the azimuthal mean tangential velocity (m s^{-1}) [top right panel], PV (PVU) on the $\theta = 304$ K surface [bottom left panel], and PV (PVU) on the $\theta = 341$ K surface [bottom right panel]. All fields are shown at $t = 24$ h.

Willoughby (1998) has shown that there are two distinct eye regimes separated by a low level inversion. The inversion is typically near 800 hPa. The air above the inversion has been in the eye since it formed and is characterized by very weak descent. Below the inversion, the air is moist due to sea surface fluxes, moist frictional inflow, and evaporation of downdrafts. A schematic of the flow regimes in the eye is shown in Fig. 4.10. Willoughby (1998) has hypothesized that the eye inversion is caused by subsidence warming. An interesting question is whether it is possible that this inversion is caused dynamically (not thermodynamically) by PV mixing. To illustrate this point, it is useful to go back to the PV conservation equation,

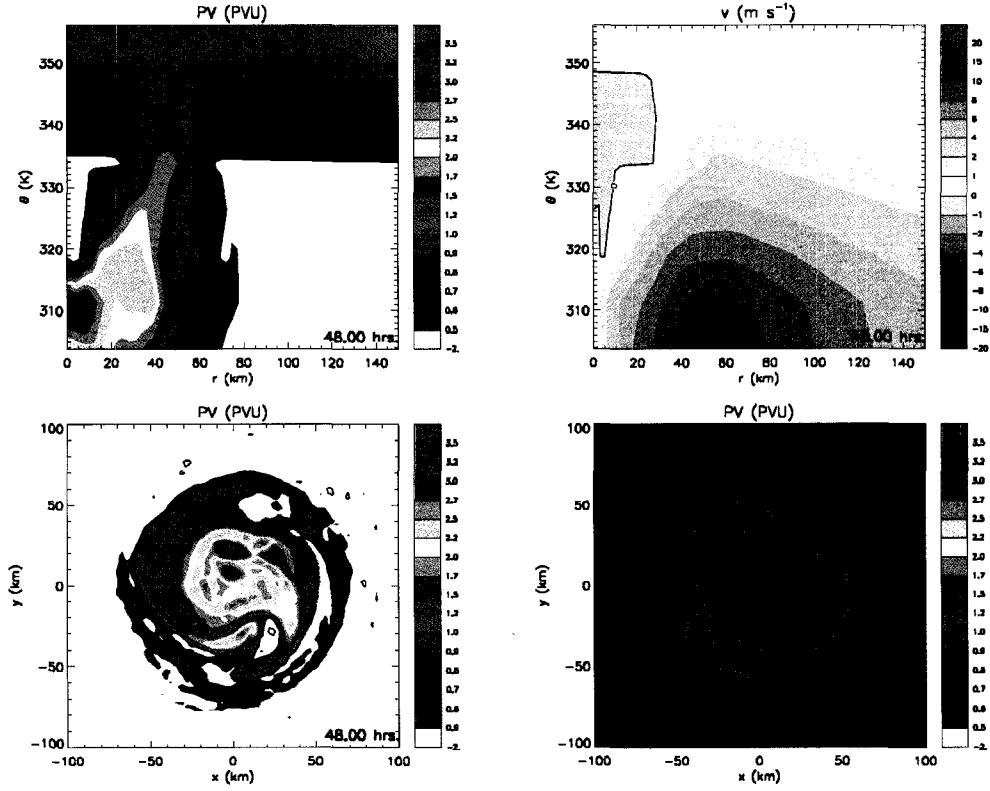


Figure 4.8: The azimuthal mean PV (PVU) [top left panel], the azimuthal mean tangential velocity (m s^{-1}) [top right panel], PV (PVU) on the $\theta = 304$ K surface [bottom left panel], and PV (PVU) on the $\theta = 341$ K surface [bottom right panel]. All fields are shown at $t = 48$ h.

$$\frac{DP}{Dt} = \frac{1}{m} \left[P \frac{\partial(m\dot{\theta})}{\partial\theta} - \frac{\partial}{\partial x} \left(\dot{\theta} \frac{\partial v}{\partial\theta} \right) + \frac{\partial}{\partial y} \left(\dot{\theta} \frac{\partial u}{\partial\theta} \right) + F_{\zeta} \right]. \quad (4.78)$$

In our simulation the diabatic term is zero and F_{ζ} is weak, and therefore PV is nearly materially conserved. The hydrostatic PV in isentropic coordinates on an f -plane is $P = (f + \zeta)/m$, or written another way, $P = -(f + \zeta)\partial\theta/\partial p$ (where g has been removed for simplicity). Thus P can be viewed as “absolute vorticity” ($f + \zeta$) multiplied by “static stability” ($-\partial\theta/\partial p$). Assuming the evolution proceeds in quasi-balance, by inversion, a given PV map can be partitioned into each of these components. Since the large PV that exists in the “PV bridge” across the eye was mixed from the eyewall, *it is possible that the hurricane eye inversion is dynamically controlled*. If this were the case, it may be one of

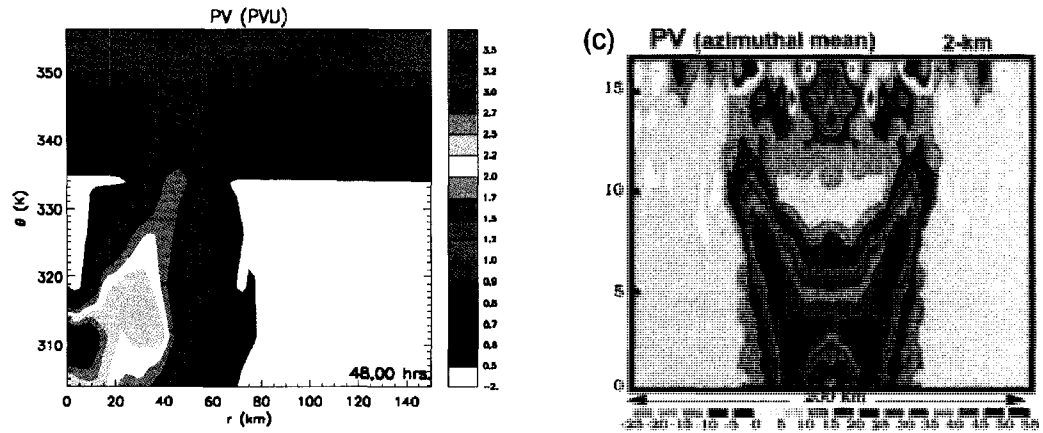


Figure 4.9: The azimuthal mean PV (PVU) in our ideal model [left panel] and in the (Yau et al. 2004) full-physics nonhydrostatic model simulation [right panel]. In the right panel, the ordinate is height above sea level in km.

the only inversions on Earth that forms dynamically, rather than by subsidence warming or warm air advection over a cool layer.

Another interesting aspect of this simulation is that initially vertically erect PV hollow tower evolved to a tilted structure. Is it possible the PV mixing in three-dimensions is one mechanism by which the eyewall slope initially forms? This will be explored in future work.

4.8.4 Integral quantities conservation

A verification test was presented to show that integral quantities are conserved. The total mass is defined as

$$R = \iiint \frac{m}{g} dx dy d\theta, \quad (4.79)$$

the kinetic energy is defined by

$$K = \iiint \frac{1}{2} (u^2 + v^2) dx dy d\theta, \quad (4.80)$$

the total energy is defined by

$$T = \iiint \left[\frac{1}{2} (u^2 + v^2) + \theta \Pi \right] dx dy d\theta, \quad (4.81)$$

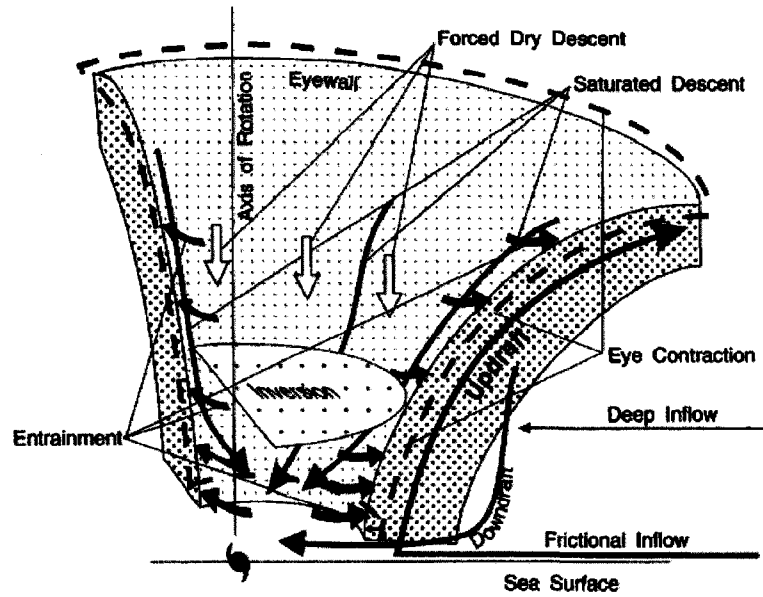


Figure 4.10: Schematic of the secondary flow in the hurricane eye and eyewall (taken from Willoughby (1998)).

and the potential enstrophy is defined by

$$\mathcal{Z} = \iiint \frac{1}{2} P^2 m \, dx \, dy \, d\theta. \quad (4.82)$$

In the absence of diabatic heating and friction, it can be shown that total energy is conserved (however kinetic and potential energy can vary). Total mass should be conserved under any circumstance. In the presence of diffusion, potential enstrophy will decay, but it is exactly conserved if there is no diffusion.

The integral quantities of total mass, total energy (potential plus kinetic), kinetic energy, and potential enstrophy are shown for the unstable baroclinic vortex evolution in Fig. 4.11. Note that the total mass and total energy are almost exactly conserved. The potential enstrophy decays from its initial value due to the PV mixing (analogous to the two-dimensional results in Hendricks et al. (2008) (chapter 3).

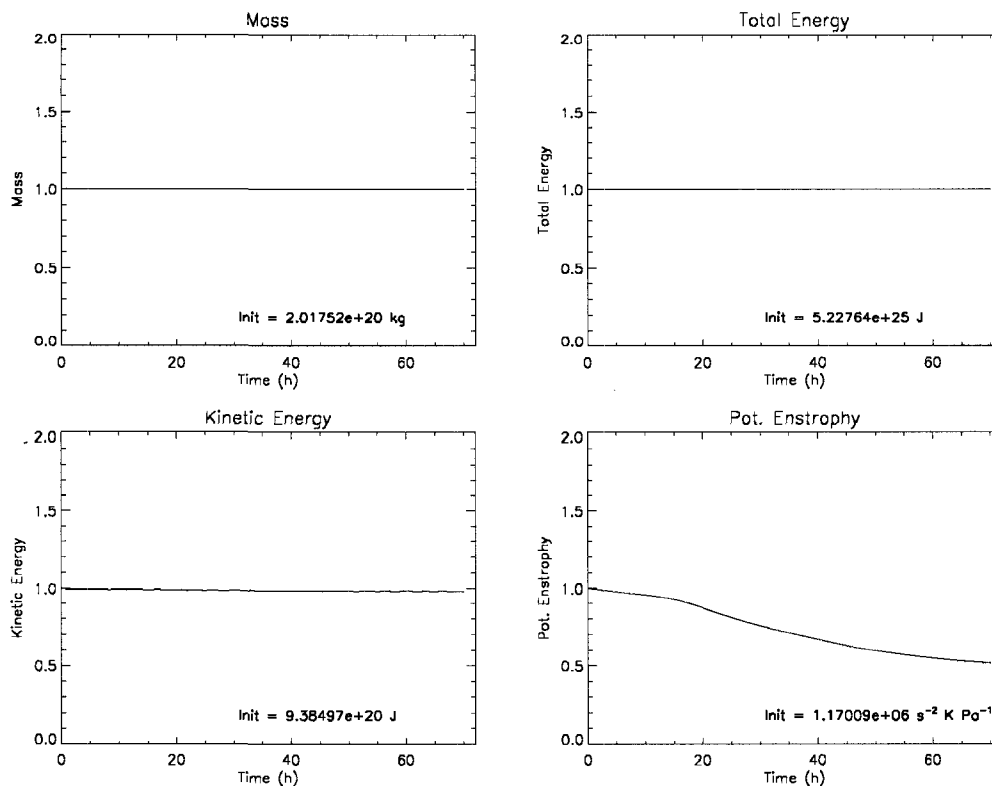


Figure 4.11: Temporal evolution of the domain integral quantities for the unstable baroclinic vortex simulation. In each panel the values are normalized by the initial value which is shown in the bottom right portion of the plot.

4.9 Conclusions

Two vertically discrete idealized hydrostatic primitive equation mesoscale models were developed using a periodic spectral shallow water model as a starting point. The first model uses an isentropic vertical coordinate and the second model uses a sigma (terrain following) vertical coordinate. Vertical staggering was done on a Charney-Phillips grid. The models can be run using either the momentum or vertical vorticity-divergence prognostic formulations. The models are simple at this point, dry and limited physics, and are designed primarily for studying the dynamics of simple flows, in particular potential vorticity (PV) and gravity wave dynamics in geophysical vortices. The major advantage of these models is the horizontal spectral representation which is ideal for simulating the intricate details of

PV mixing in resulting the from the dynamic breakdown of unstable vortices. The models include a balance initialization that computes the balanced mass field given a specified wind field. The nonlinear balance equation is solved in the horizontal and the hydrostatic equation is enforced in the vertical. The models are written in FORTRAN-90 and compile easily with the free GNU g95 compiler.

Evaluation tests were presented for the isentropic vertical coordinate model. First, verification tests were performed that the balance initialization works correctly and that the integral quantities of mass and total energy were conserved. Two validation tests were also performed. In the first test, the primitive equation model was shown to simulate the gradient adjustment of axisymmetric vortex. Realistic internal gravity waves were produced as the mass field adjusted to the vortex winds. The mass field adjusted to a steady final state which was similar to that obtained from the model's balance initialization. Secondly, the evolution of an unstable hurricane-like PV hollow tower was simulated. The unstable baroclinic vortex broke down at lower levels causing PV to be mixed from the eyewall to the eye. A "PV bridge" formed across the eye which has been previously simulated in moist full-physics models. It is interesting that our ideal model simulated this feature. By inversion, a portion of this "PV bridge" is static stability, and thus it is possible that the hurricane eye inversion is *dynamically controlled*, and as such, it may be one of the only inversions of this sort on Earth. Another interesting aspect of this simulation was that an initially vertically erect PV hollow tower became tilted due to adiabatic PV mixing preferentially at lower levels. Thus it is possible that one mechanism for the formation of the eyewall slope in hurricanes is PV mixing resulting from dynamic instability. This will be explored further in future work.

At present, the isentropic coordinate model has difficulty simulating the evolution of strong vortices ($v_{\max} > 30 \text{ m s}^{-1}$). In these cases, the balanced mass field has massless layers due to θ surfaces bending into the ground. The model's mass restoration routine corrects this however, at each time step the mass tries to become negative due to the Rossby radius

regime of mass adjusting to the wind. In light of this fact, the sigma coordinate model is recommended for stronger vortices. The results of the isentropic model are very encouraging, and this model presents a great way to view the hurricane evolution in a dynamically clean manner, i.e., making PV maps on isentropic surfaces similar to Hoskins et al. (1985) for global data.

Further verification tests need to be conducted on the sigma coordinate model. Future work will be focused on improving the sigma coordinate model, as well as add as well as adding addition physics (such as surface fluxes and moisture) to both models so they can simulate the evolution of more realistic tropical cyclones.

Chapter 5

SHALLOW WATER SIMULATION OF A SPONTANEOUSLY RADIATING HURRICANE-LIKE VORTEX

5.1 Introduction

Gravity waves are ubiquitous features in the stably stratified atmosphere. They may be produced by flow over topography (mountain waves), latent heat release from moist convection, and by an adjustment of an unbalanced flow into a state of balance. The latter is usually referred to as geostrophic adjustment, however balance adjustment is a more appropriate term for a general flow. In the special case when a flow evolves at sufficient rapidity to fall out of balance, the term *spontaneous radiation* has been used to describe the unforced inertia-gravity wave radiation that ensues. The slow manifold (Leith 1980) is an atmospheric invariant completely devoid of such gravity wave activity. The flow is balanced, and it, along with the geopotential, may be obtained at any instant by potential vorticity (PV) inversion. The existence (Lorenz 1986) or nonexistence (Lorenz and Krishnamurthy 1987) of such a strict slow manifold in the real atmosphere has been debated for decades.

In a pioneering paper, Lighthill (1952) explicitly defined the concept of spontaneous adjustment emission of sound waves from vortical flow through multiscale frequency matching. These ideas were extended to spontaneous inertia-gravity wave radiation from vortical flows in the atmosphere using the shallow water equations (Ford 1994a,b; Ford et al. 2000). The question that arises is whether or not spontaneous inertia-gravity wave (hereafter IGW) emission is of meteorological significance from an energy and angular momentum budget perspective, which ultimately lies at the heart of the validity of the balance approximation

and potential vorticity inversion. While it is generally regarded that the strict slow manifold rarely, if ever, exists, the level of fuzziness is not well understood. Saujani and Shepherd (2002) argued that the fuzziness is exponentially small for quasigeostrophic flow. Moreover, the characteristics of a given balanced flow that favor its potential to spontaneously radiate are not well understood (Viudez and Dritschel 2006).

Spontaneous IGW radiation has recently been studied for both atmospheric jets (e.g., O'Sullivan and Dunkerton 1995, Zhang 2004) and vortices (e.g., Ford et al. 2000, Schecter and Montgomery 2006, Viudez 2006). Schecter and Montgomery (2006) examined conditions that favor spontaneous radiation from intense mesocyclones such as tornadoes and hurricanes. One interesting result from their study was that under certain conditions PV edge waves on monotonic cyclones can grow due to a positive feedback from the spontaneous IGW emission. IGWs have been hypothesized to create the moving spiral cloud bands in tropical cyclones that are often visible in satellite imagery (Kurihara 1979; Chow et al. 2002). This is in contrast to theories ascribing their existence to breaking PV waves (Guinn and Schubert 1993; Montgomery and Kallenbach 1997). Chow and Chan (2004) argued that this emission may be an important sink of angular momentum from the hurricane.

In this paper, spontaneous adjustment emission from TC cores is explored further. An unforced dynamically active, spontaneously radiating, hurricane-like vortex has been simulated using a shallow water model. The initial condition is balanced, and motivated by observations of hurricanes that have elliptically shaped eyewalls. An analysis of this case study is given lending new insight into the growing body of literature on spontaneous radiation from intense vortices. In section 5.2, solutions to the linearized shallow water equations about a resting basic state are obtained to use as a guideline for interpreting the nonlinear numerical simulation. A description of the numerical simulation, observational justification, and results are given in section 5.3. An analysis of the results is given in section 5.4. Finally, a summary of the relevant findings of this case study is presented in section 5.5.

5.2 Linearized Shallow Water Equations

The linearized shallow water equations governing small amplitude motions about a resting basic state in polar coordinates are

$$\frac{\partial u'}{\partial t} - f v' + g \frac{\partial h'}{\partial r} = 0, \quad (5.1)$$

$$\frac{\partial v'}{\partial t} + f u' + g \frac{\partial h'}{r \partial \phi} = 0, \quad (5.2)$$

$$\frac{\partial h'}{\partial t} + \bar{h} \left(\frac{\partial(r u')}{r \partial r} + \frac{\partial v'}{r \partial \phi} \right) = 0, \quad (5.3)$$

where u' is the perturbation radial velocity, v' is the perturbation tangential velocity, h' is the perturbation fluid depth, and \bar{h} is the mean depth. These equations may be expressed in vorticity-divergence form as

$$\frac{\partial \zeta'}{\partial t} + f \delta' = 0, \quad (5.4)$$

$$\frac{\partial \delta'}{\partial t} - f \zeta' + g \nabla^2 h' = 0, \quad (5.5)$$

$$\frac{\partial h'}{\partial t} + \bar{h} \delta' = 0, \quad (5.6)$$

where δ' is the divergence and ζ' is the perturbation relative vorticity. Seeking separable modal solutions of the form $g'(r, \phi, t) = \hat{g}(r) \exp(i(m\phi - \nu t))$ for each prognostic variable, we obtain

$$-i\nu \hat{\zeta} + f \hat{\delta} = 0, \quad (5.7)$$

$$-i\nu \hat{\delta} - f \hat{\zeta} + g \left[\frac{d}{r dr} \left(r \frac{d\hat{h}}{dr} \right) - \frac{m^2}{r^2} \hat{h} \right] = 0, \quad (5.8)$$

$$-i\nu\hat{h} + \bar{h}\hat{\delta} = 0. \quad (5.9)$$

The combination of $f \times (5.9)$ and $\bar{h} \times (5.7)$ yields

$$-i\nu \left(\hat{\zeta} - \frac{f}{\bar{h}} \hat{h} \right) = 0. \quad (5.10)$$

Substituting (5.9) and (5.10) for nonzero ν into (5.8), we obtain

$$(\nu^2 - f^2) \hat{h} + g\bar{h} \left[\frac{d}{rdr} \left(r \frac{d\hat{h}}{dr} \right) - \frac{m^2}{r^2} \hat{h} \right] = 0 \quad (5.11)$$

Rewriting (5.11) using $\nu^2 = f^2 + g\bar{h}k^2$, we obtain Bessel's equation

$$r^2 \frac{d^2 \hat{h}}{dr^2} + r \frac{d\hat{h}}{dr} + (k^2 r^2 - m^2) \hat{h} = 0. \quad (5.12)$$

One solution to (5.12) are Hankel functions (linear combinations of first $J_m(kr)$ and second $Y_m(kr)$ order Bessel functions)

$$H_m^{(1)}(kr) = J_m(kr) + iY_m(kr), \quad (5.13)$$

$$H_m^{(2)}(kr) = J_m(kr) - iY_m(kr). \quad (5.14)$$

The $H^{(1)}$ Hankel function represents outward propagating cylindrical waves while the $H^{(2)}$ Hankel function represents inward propagating waves. The nonlinear simulation exhibits outward radiation, therefore the $H^{(1)}$ function is chosen. The final linear solutions for the perturbation quantities are thus

$$\zeta'(r, \phi, t) = (fh_0/\bar{h}) H_m^{(1)}(kr) \exp[i(m\phi - \nu t)], \quad (5.15)$$

$$\delta'(r, \phi, t) = (i\nu h_0/\bar{h}) H_m^{(1)}(kr) \exp[i(m\phi - \nu t)], \quad (5.16)$$

$$h'(r, \phi, t) = h_0 H_m^{(1)}(kr) \exp[i(m\phi - \nu t)], \quad (5.17)$$

where h_0 is specified. In Fig. 5.1, polar plots of the linear solution are shown for varying azimuthal wavenumbers $m = 1, 2, 3, 4$ while holding the radial wavenumber $k = 0.04 \text{ km}^{-1}$

and $f = 0.000037 \text{ s}^{-1}$ fixed. Similarly, the dependence of the solution on varying radial wavenumber $k = 0.01, 0.025, 0.05, 0.1 \text{ km}^{-1}$ is shown in Fig. 5.2, while holding the azimuthal wavenumber $m = 2$, and $f = 0.000037 \text{ s}^{-1}$ fixed. The linear solutions will be used as a guideline to interpret portions of the nonlinear model simulation (next section).

By defining the potential vorticity of the fluid as

$$P = \bar{h} \frac{f + \zeta}{h} = \bar{h} \frac{f + \bar{\zeta} + \zeta'}{\bar{h} + h'} \quad (5.18)$$

it can easily be shown that the P field does not see propagating inertia-gravity waves. Note that in Figs. 5.1 and 5.2, h' and ζ' always have the same sign in the same regions, thus the two fields change such that P does not change. To illustrate this, a contour plot of P is shown in Fig. 5.3 for $m = 2$, $k = 0.01 \text{ km}^{-1}$, $f = 0.000037 \text{ s}^{-1}$, and $\bar{h} = 4285 \text{ m}$. Also note in Figs. 5.1 and 5.2 that the divergence δ is $\pi/2$ radians out of phase from h' and ζ' .

5.3 Numerical Simulation

A periodic Fourier spectral shallow water model (Fulton 2007) is used for the numerical simulation. In the shallow water model, there are options for both momentum and vorticity-divergence prognostic formulations. Instead of predicting the fluid depth, the model predicts $p := g(h - \bar{h})/c$, where $c^2 = g\bar{h}$ is the square of the pure gravity wave phase speed. Note that p has units of m s^{-1} . Since p is the geopotential deviation divided by the constant gravity wave phase speed, p may be converted to h and vice-versa. The momentum equations in rotational momentum form are

$$\frac{\partial u}{\partial t} - fv + \frac{\partial}{\partial x}(cp + K) = F_u, \quad (5.19)$$

$$\frac{\partial v}{\partial t} + fu + \frac{\partial}{\partial y}(cp + K) = F_v, \quad (5.20)$$

where $K = (u^2 + v^2)/2$ is the kinetic energy. By taking the curl ($\mathbf{k} \cdot \nabla \times$) and divergence ($\nabla \cdot$) of $\partial \mathbf{u} / \partial t$, the equations in vorticity-divergence form are

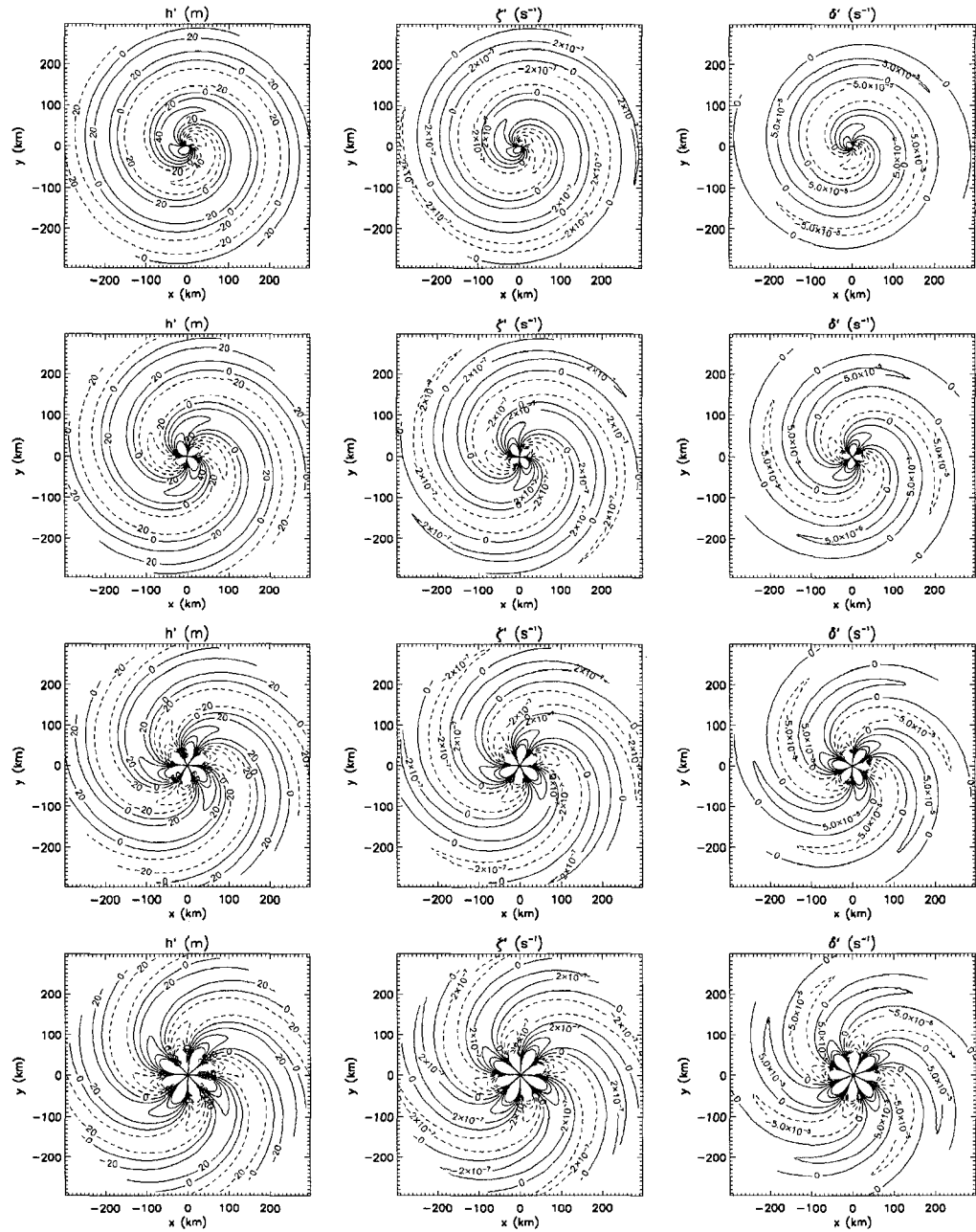


Figure 5.1: Linear solution to the shallow water equations in cylindrical polar space for varying azimuthal wavenumber: $m = 1$ (top left), $m = 2$ (top right), $m = 3$ (bottom left), $m = 4$ (bottom right). The radial wavenumber $k = 0.04 \text{ km}^{-1}$ is held fixed. The contour intervals for h' , ζ' and δ' are 20 m, $2 \times 10^{-7} \text{ s}^{-1}$, and $5 \times 10^{-5} \text{ s}^{-1}$, respectively. The perturbation height h' is set to a maximum amplitude of 100 m, and all other variables are determined from this value.

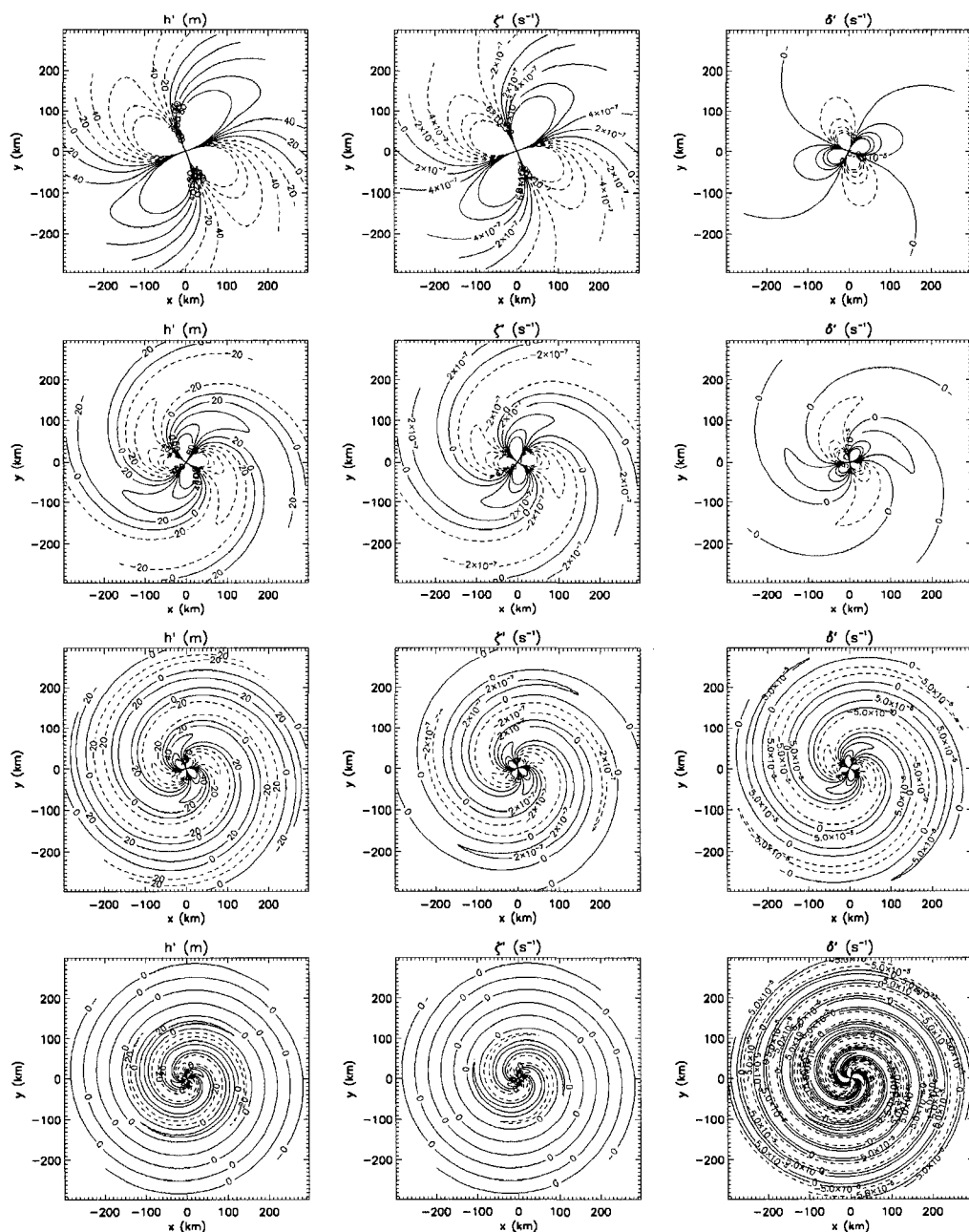


Figure 5.2: Linear solution to the shallow water equations in cylindrical polar space for varying radial wavenumber: $k = 0.01$ (top left), $k = 0.025$ (top right), $k = 0.05$ (bottom left), $k = 0.10$ (bottom right) km^{-1} . The azimuthal wavenumber $m = 2$ is held fixed. The contour intervals for h' , ζ' and δ' are 20 m, $2 \times 10^{-7} \text{ s}^{-1}$, and $5 \times 10^{-5} \text{ s}^{-1}$, respectively. The perturbation height h' is set to a maximum amplitude of 100 m, and all other variables are determined from this value.

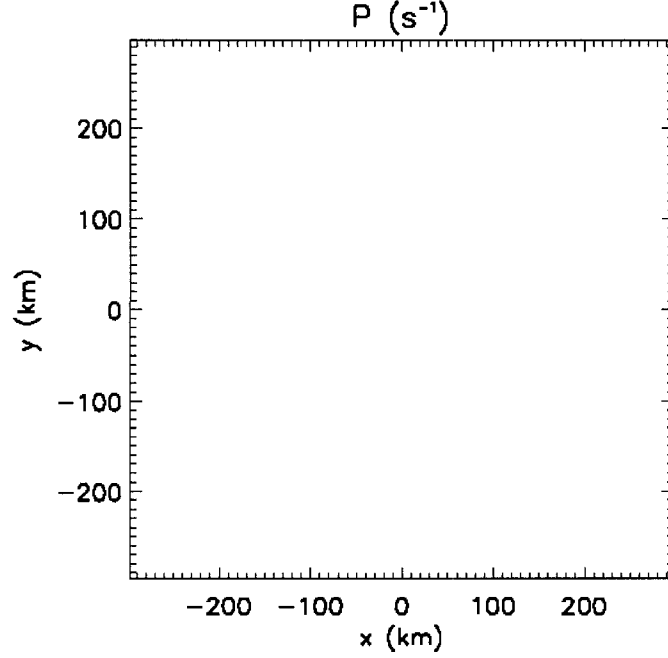


Figure 5.3: The potential vorticity P for $m = 2$, $k = 0.01 \text{ km}^{-1}$, $f = 0.000037 \text{ s}^{-1}$, and $\bar{h} = 4285 \text{ m}$. The contour plot was made with 100 contour levels of P to illustrate that P is invariant as IGWs propagate.

$$\frac{\partial \zeta}{\partial t} + \frac{\partial(\zeta u)}{\partial x} + \frac{\partial(\zeta v)}{\partial y} = F_\zeta, \quad (5.21)$$

$$\frac{\partial \delta}{\partial t} + \frac{\partial(\zeta u)}{\partial y} - \frac{\partial(\zeta v)}{\partial x} + \nabla^2(cp + K) = F_\delta. \quad (5.22)$$

The continuity equation,

$$\frac{\partial p}{\partial t} + c \left(\frac{\partial u}{\partial x} + \frac{\partial v}{\partial y} \right) + \left(\frac{\partial(pu)}{\partial x} + \frac{\partial(pv)}{\partial y} \right) = F_p, \quad (5.23)$$

is the same for both formulations. By introducing a streamfunction ψ and a velocity potential χ , the vector velocity may be expressed as $\mathbf{u} = \nabla\chi + \mathbf{k} \times \nabla\psi$, implying that $\nabla^2\psi = \zeta$ and $\nabla^2\chi = \delta$.

The initial condition is an offset monopole in a hollow ellipse (Fig. 5.4 left panel). This initial condition was motivated by observations of Hurricane Ivan (2004) (Fig. 5.5).

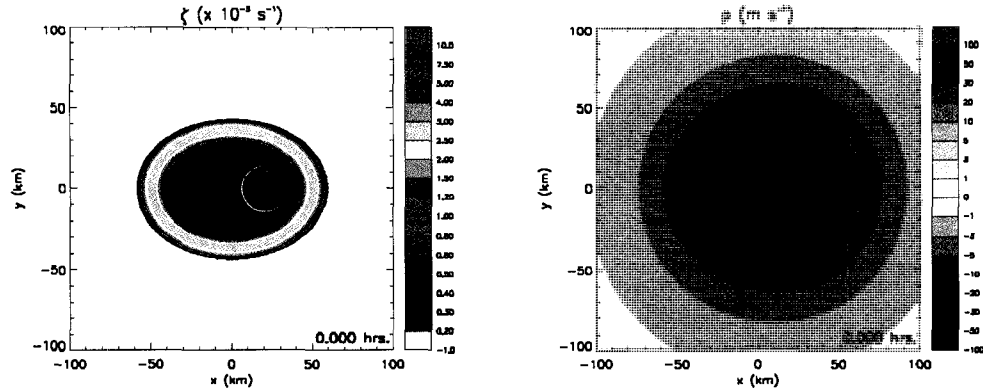


Figure 5.4: The relative vorticity ζ (left panel) and pressure p (right panel) at $t = 0$ h. The divergence δ (not shown) is initially zero.

At this time Ivan had concentric eyewalls, and the outer eyewall was distinctly elliptically shaped. To simplify the initial condition, in our experiment the inner eyewall was modeled as a monopole.

The vorticity-divergence prognostic formulation was used for the simulation. The solution was obtained on a doubly periodic f -plane domain with $L = 600$ km. The resolution is 1024×1024 points. After dealiasing of the quadratic advection term, 370 Fourier modes were kept, yielding an effective resolution of 1.8 km. Diffusion was set to $25 \text{ m}^2 \text{ s}^{-1}$, yielding an e -folding time of 0.19 h for all modes having total wavenumber 370. Time differencing was accomplished using a standard third order semi-implicit scheme¹ with a time step of 1 s. The simulation was executed for 48 h and output was obtained at 180 s intervals. A sponge layer was used near the lateral boundaries to damp the outwardly propagating IGWs. The lateral extent was 60 km, a smoothly transitioning sponge function was used, and Rayleigh damping was used with a coefficient $\beta = 0.00278 \text{ s}^{-1}$. This corresponds to an e -folding time of 0.10 h for the shortest wave.

¹ Although implicit methods are known to distort gravity waves, recent work has shown that only the high frequency, low energy containing waves are distorted significantly (Thomas and Browning 2001). Spontaneous adjustment emission is by nature low frequency since it is forced by Rossby wave dynamics. This, combined with the fact that the time step used satisfied the Courant condition for shallow water gravity waves, indicates that the waves are likely not distorted.

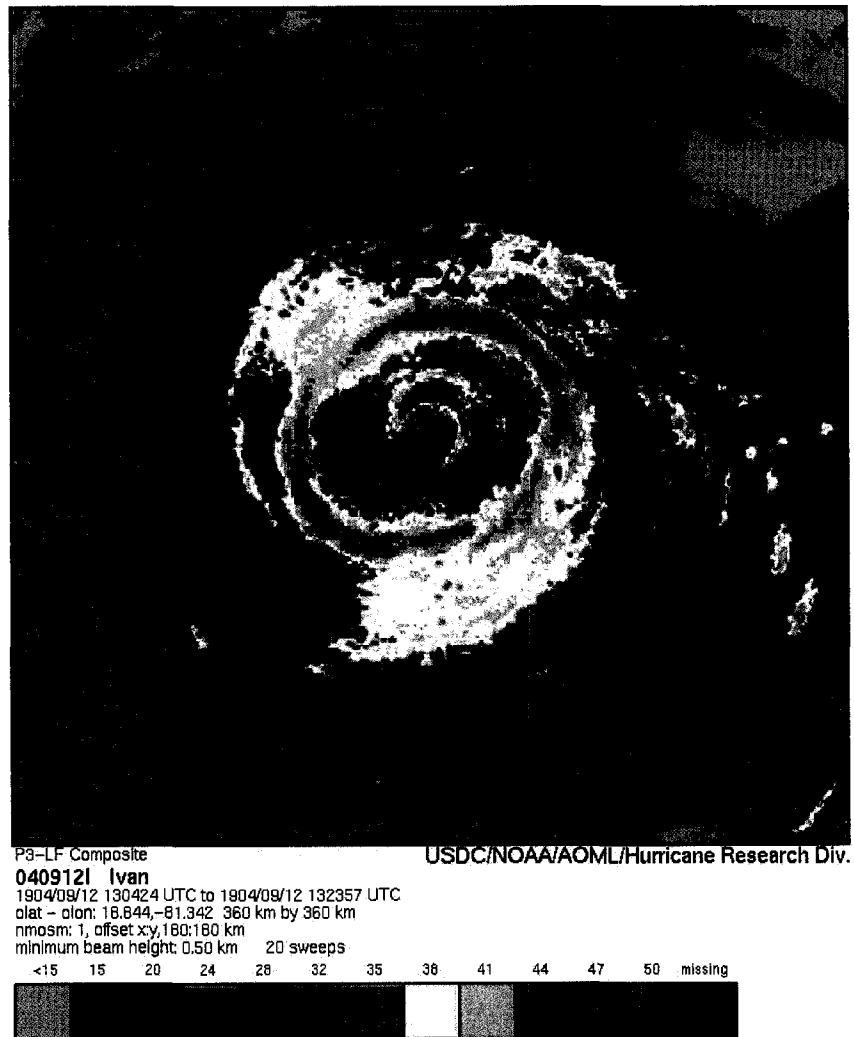


Figure 5.5: Composite radar reflectivity (dBz) of Hurricane Ivan from NOAA P-3 aircraft. [credit: NCDC/NOAA/AOML/Hurricane Research Division].

5.4 Discussion of results

Side-by-side plots of the relative vorticity and divergence are shown in Fig. 5.6 at various times during the unforced evolution in the innermost part of the domain: $[-100,100]$ km. The vorticity field evolves as follows. At $t = 0.5$ h, the differential rotation associated with the central monopole deforms the outer ring. The initial deformation of the outer ring is quite similar to the contour dynamics experiment of Oda et al. (2006). By $t = 2.5$ h, the low vorticity region has been separated into two pieces: an axisymmetric inner region outside the central monopole, and an outer region. By $t = 10.0$ h, very low vorticity environmental air has been enclosed near $(x, y) = (-30, 0)$ km. At this time, the vortex can be characterized as a tripole (high-low-high vorticity) in the y -direction and a pentapole (high-low-high-low-high) in the x -direction through the origin. Examining the divergence (right panels), a persistent wavenumber-2 feature is present. This is the response of the mass field to the propagating wavenumber-2 vortex Rossby wave, or elliptical deformation of the central monopole. Outward propagating IGWs are being emitted from the vortex core and the vortex can be considered to be spontaneously radiating very early.

In Fig. 5.7, the evolution of the vortex is shown at later times: $t = 20.0, 30.0, 45.0$ h. The central monopole now has a stronger elliptical signature, and the eccentricity becomes larger with time. The pentapole structure is evident, and the ellipse and outer low vorticity regions are rotating at different frequencies, causing them to align in and out of phase. In the divergence plots, outward propagating IGWs are evident and the amplitude has increased significantly from earlier times. This simulation was run to $t = 48.0$ h, and there was no apparent reduction in IGW activity at this time.

In Fig. 5.8, Hovmöller plots of the evolution of relative vorticity and divergence are shown from $t = 24$ – 25 h. The plots were made by taking a y cross section through the vortex center at each time. In the top panel, the important features to note are the semimajor axis a and semiminor axis b of the rotating elliptical vorticity core. The period of the ellipse oscillation is $L_e = 0.25$ h (or 900 s), corresponding to a frequency $\nu_e = 0.00698$ s $^{-1}$. The

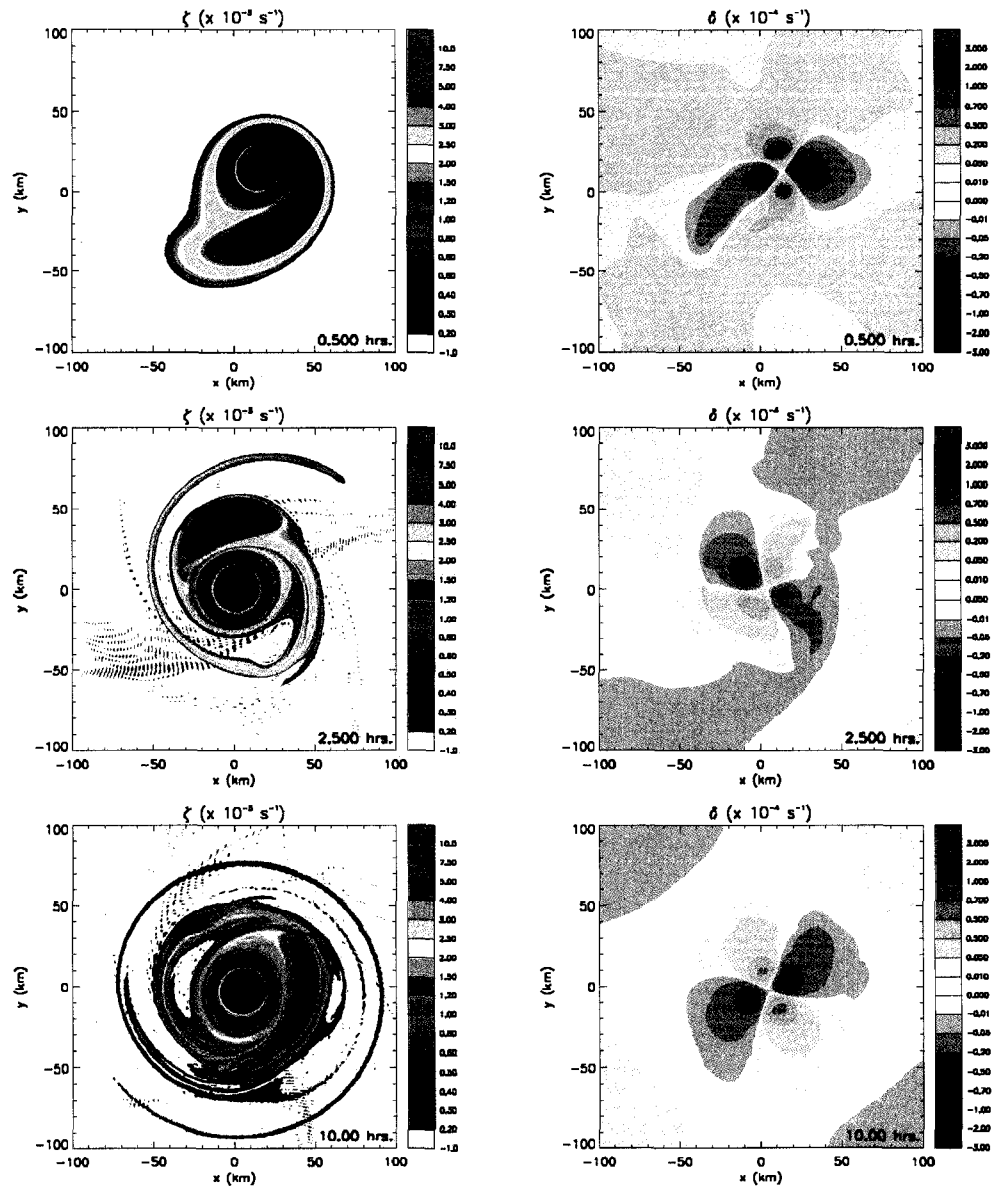


Figure 5.6: Early evolution of relative vorticity (left panels) and divergence (right panels) in the shallow water simulation.

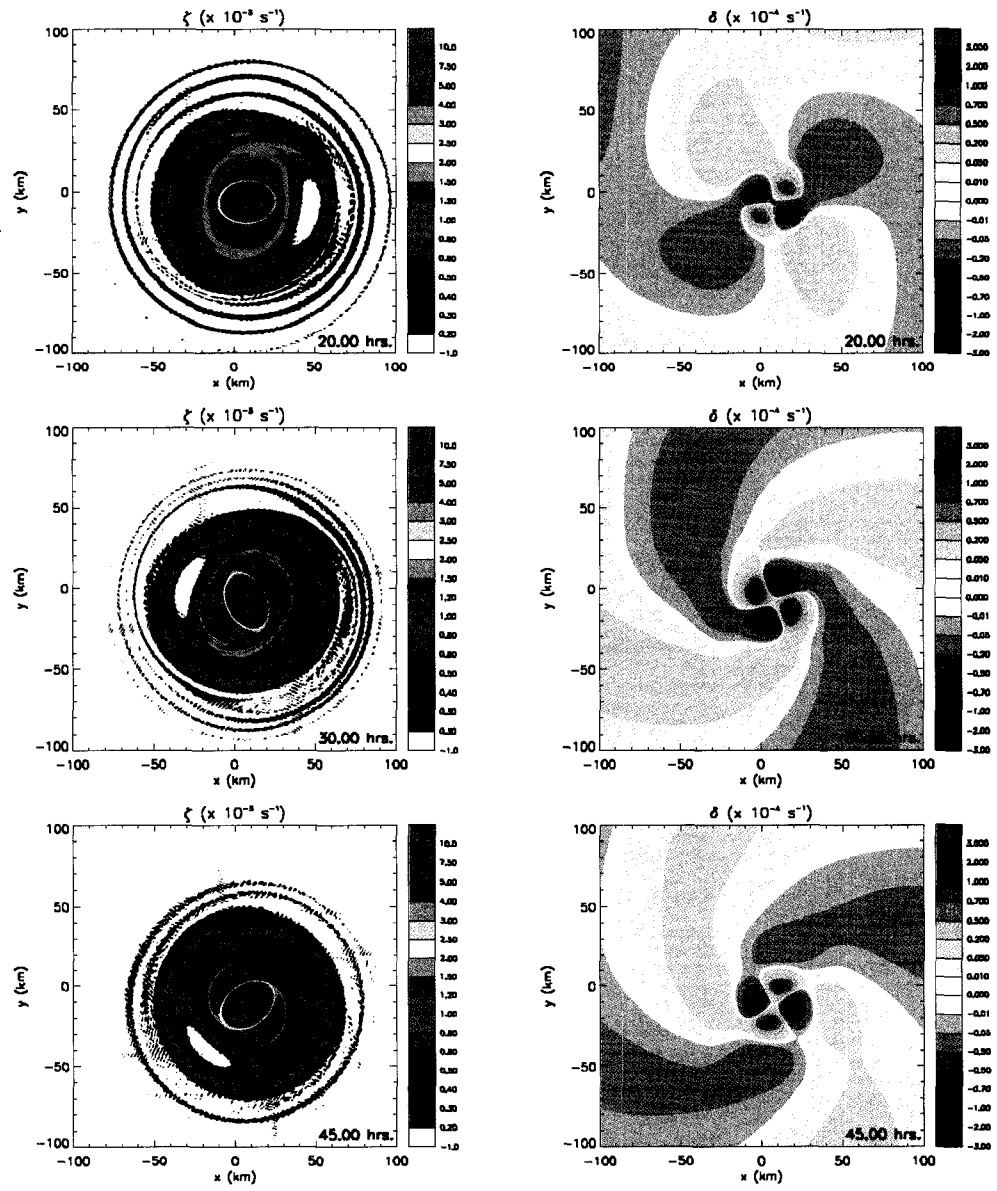


Figure 5.7: Later evolution of relative vorticity (left panels) and divergence (right panels) in the shallow water simulation.

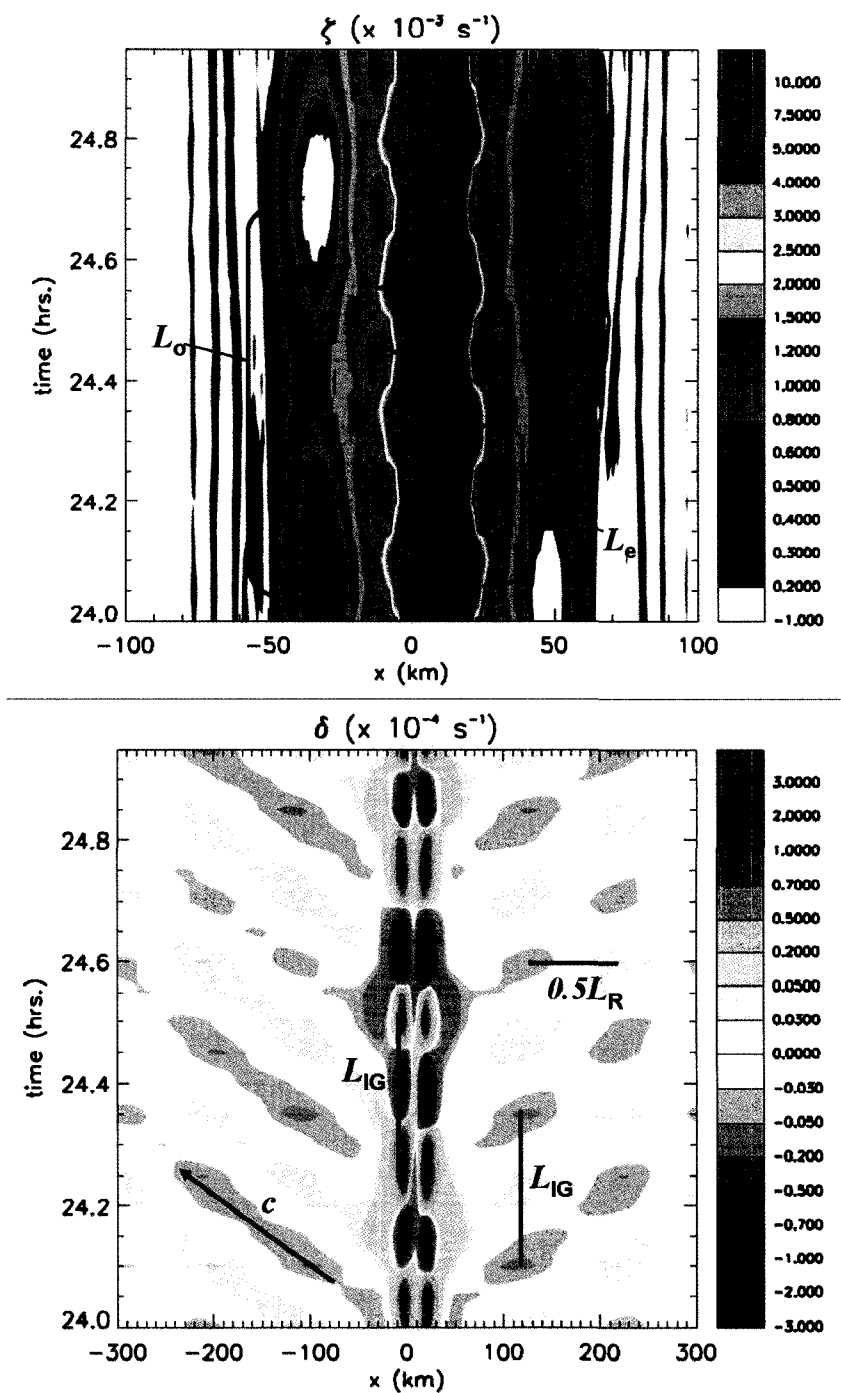


Figure 5.8: Hovmöller plots of relative vorticity (top panel) and divergence (bottom panel) in the shallow water simulation from $t = 24$ – 25 h. Plots were made by holding the y -coordinate of the vortex center (largest vorticity) fixed at each output time level. In the top panel, a and b denote the semi-major and semi-minor axes of the central ellipse, L_e denotes the oscillation period of the central ellipse, and L_σ is the oscillation period of the outer low vorticity regions. In the bottom panel, c is the pure gravity wave phase speed, L_{IG} is the IGW period and L_R is the radial wavelength.

period of the outer low vorticity patch is longer, $L_o = 0.65$ h (or 2340 s), corresponding to a frequency $\nu_o = 0.00269$ s⁻¹. During the simulation, the outer structures and inner structures move in and out of phase, possibly contributing to non-axisymmetrization. In the bottom panel, the important features are the outward propagating IGWs. The phase speed of the observed IGWs appears to be constant, and can be estimated from the figure. For example, the area of convergence with the arrow over it propagates approximately $\Delta d = 110$ km in a time period of $\Delta t = 0.15$ h. The phase speed associated with this is $c = (100000 \text{ m}) / (540 \text{ s}) = 203.7$ m s⁻¹, which is very close to the phase speed $c = 205$ m s⁻¹ supported by the resting model fluid depth of $\bar{h} = 4284$ m. The period of the IGWs can be ascertained from two places: near the ellipse and in the outer domain. Both locations give the same $L_{IG} = 0.25$ h (or 900 s), corresponding to a frequency $\nu_{IG} = 0.00698$ s⁻¹. Lastly, the radial wavelength of the waves is determined from the diagram: $L_R = 200$ km (or a half wavelength of 100 km). This corresponds to a radial wavenumber $k = 0.034$ km⁻¹. One can verify that the parameters above satisfy $\nu_{IG}^2 = f^2 + c^2 k^2$.

Note that $\nu_e = \nu_{IG} = 0.00698$ s⁻¹ indicating that frequency matching has occurred between the rapidly oscillating ellipse and an intrinsic IGW frequency. Plotting the relationship $\nu_{IG} = (f^2 + c^2 k^2)^{1/2}$ in Fig. 5.9, note the frequency matched radial wavenumber $k = 0.034$ km⁻¹. To summarize, a rapidly oscillating, non-axisymmetrizing, ellipse evolves out of the unforced initial condition of the experiment. The oscillation frequency of the ellipse matches an intrinsic IGW frequency, causing outward IGW radiation to the environment of a preferred radial wavenumber.

Why does the rapidly oscillating ellipse not axisymmetrize? Dritschel (1998) has shown that the ability of a non-axisymmetric vorticity core to axisymmetrize via inviscid nondivergent dynamics is dependent on the sharpness of its edge. Rankine-like vortices (i.e., possessing a sharp edge) are not as likely to axisymmetrize as Gaussian vortices because they cannot generate filaments as easily. The filamentation process is a sign of axisymmetrization. Examining Fig. 5.8, the ellipse in the experiment has a very sharp edge, with

the relative vorticity ζ dropping an order of magnitude (from $10 \times 10^{-3} \text{ s}^{-1}$ to $1 \times 10^{-3} \text{ s}^{-1}$) in approximately 3-5 km. Also note that in Fig. 5.7, strong vorticity filaments are not being created. At $t = 45 \text{ h}$, two thin weak filaments are evident, but at other times it is hard to find filaments. Thus it is likely that the ellipse's sharp edge is contributing to non-axisymmetrization. A second reason for non-axisymmetrization are the vorticity structures outside of the central ellipse. A pentapole structure formed with the outer low vorticity structures (with period L_o ; see Fig. 5.8) rotating with a lower angular velocity than the ellipse. This causes alternating tripole and pentapole patterns to exist. While the main reason for non-axisymmetrization is the central ellipse with a sharp edge, it is possible that the flow associated with the outer vorticity structures is also contributing. Vorticity structures with sharp edges are often numerically simulated in full-physics models (Corbosiero et al. 2006) and observed (Kossin and Eastin 2001) in hurricanes. Thus persistent non-axisymmetric structures likely exist in tropical cyclone cores, promoting prolonged episodes of spontaneous adjustment emission.

Can the central ellipse oscillation frequency be explained in a simpler context? It is well known that in a nondivergent framework an elliptical vortex patch (the Kirchhoff vortex) will rotate with a certain angular velocity owing to the magnitude of the vorticity patch and the semi-major and semi-minor axis, i.e.,

$$\omega_{\text{KI}} = \zeta \frac{ab}{(a+b)^2}, \quad (5.24)$$

where ω_{KI} is the angular velocity of the Kirchhoff elliptical vortex. This occurs because when the Poisson equation is solved to obtain the streamfunction, it is less eccentric than the vorticity ellipse leading to vorticity advection (see Fig. 5.10). Larger vorticity indicates larger winds leading to an increased rotation rate ω_{KI} .

In the numerical simulation, the central ellipse is nearly a constant vorticity patch with magnitude $\zeta = 0.016 \text{ s}^{-1}$. In the 24-25 h period, the semi-major axis $a = 33 \text{ km}$ and the semi-minor axis $b = 22 \text{ km}$. Substituting these values into (5.23), we obtain $\omega_{\text{KI}} = 0.00384 \text{ rad s}^{-1}$. Since the signal is repeated twice for every ellipse rotation, the Kirchhoff ellipse

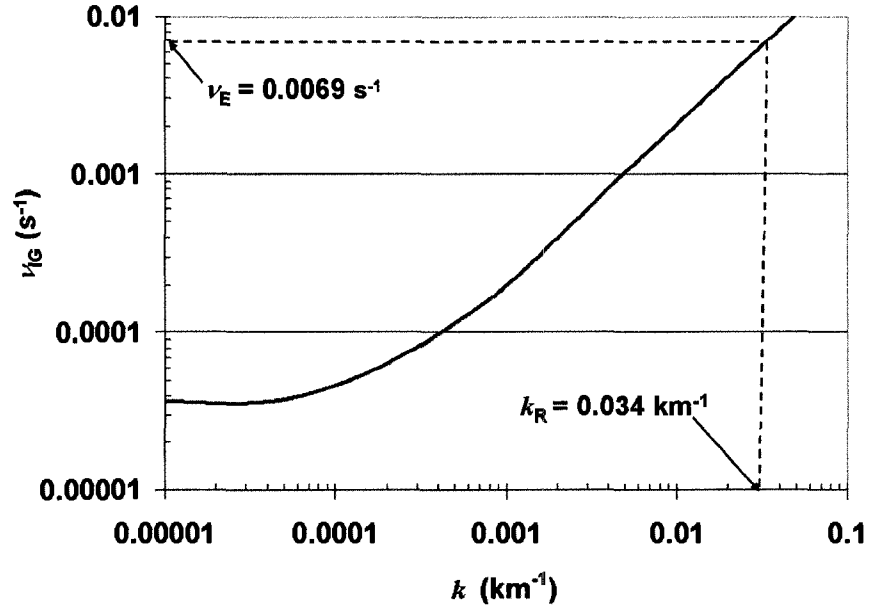


Figure 5.9: IGW frequency versus radial wavenumber for $c = 205 \text{ m s}^{-1}$ and $f = 0.000037 \text{ s}^{-1}$.

frequency $\nu_{\text{KI}} = 2\omega_{\text{KI}} = 0.00768 \text{ s}^{-1}$. Hence, the frequency of a Kirchoff ellipse is nearly the same as (but slightly greater) the observed frequency, i.e., $\nu_{\text{KI}} \approx \nu_e$. Therefore, the rotation rate of the simulated central ellipse can largely be explained by a simple Kirchoff vortex, and because it is slightly larger than the observed rotation rate, the outer wind field is actually slowing the elliptical vortex down slightly.

In Fig. 5.11, the linear solution is compared to the numerical experiment for the divergence for three successive times (each 3 minutes apart). At small radii, the linear solution is not valid, however note that the azimuthal cyclonic propagation of the IGW spiral bands nearly match the spiral bands in the numerical experiment. This is evidence that the just outside the central ellipse the dynamics are mostly linear – freely propagating IGWs on a weak basic state flow.

In Fig. 5.12, the azimuthal mean velocity and pressure are shown for the spontaneously radiating vortex at $t = 0 \text{ h}$ and $t = 48 \text{ h}$. The vortex center was defined by the

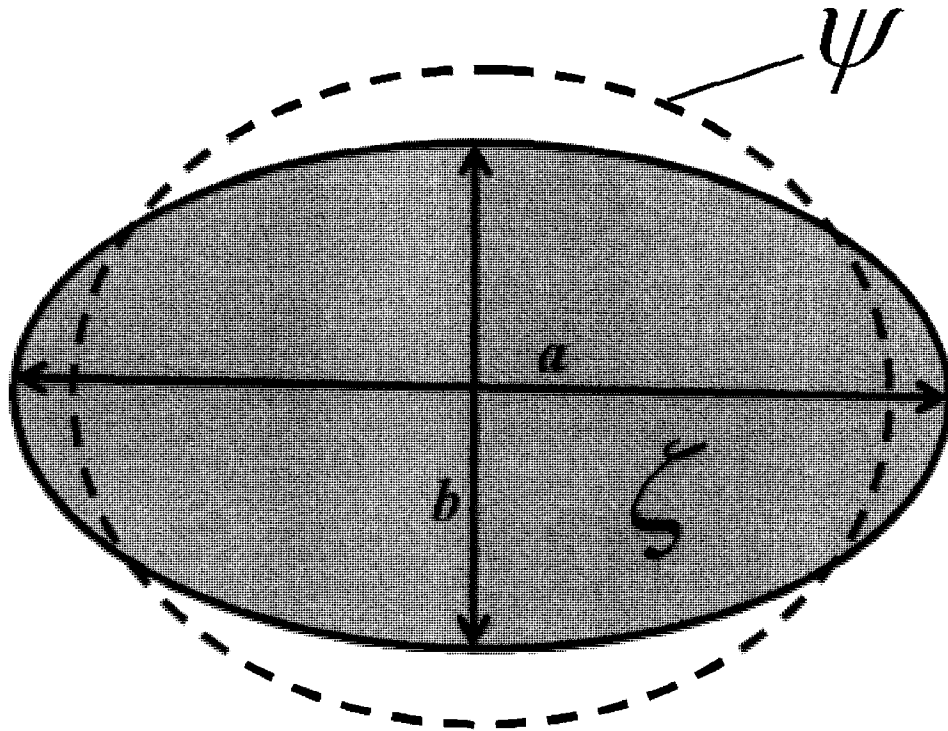


Figure 5.10: Conceptual diagram of the Kirchhoff vorticity ellipse and associated streamfunction that would be obtained by solving Poisson's equation (i.e., $\nabla^2\psi = \zeta$) for a non-divergent flow. The ellipse rotates cyclonically (for positive ζ) because the streamfunction is slightly less elliptical than the vorticity patch. This occurs because solving the Poisson equation is a smoothing operation.

maximum vorticity in the domain. This was obtained by moving a square with a dimension of 23 km over the entire domain, averaging the vorticity in that square, and then determining the grid point in the square center where for which the average vorticity was a maximum. Over the course of the simulation the peak mean tangential winds fell from 100.8 m s^{-1} to 86.6 m s^{-1} and the minimum central pressure rose from -67.5 m s^{-1} to -63.5 m s^{-1} . Thus, the outward radiation of spiral IGWs is a sink of tangential (and angular) momentum (consistent with Chow and Chan 2004).

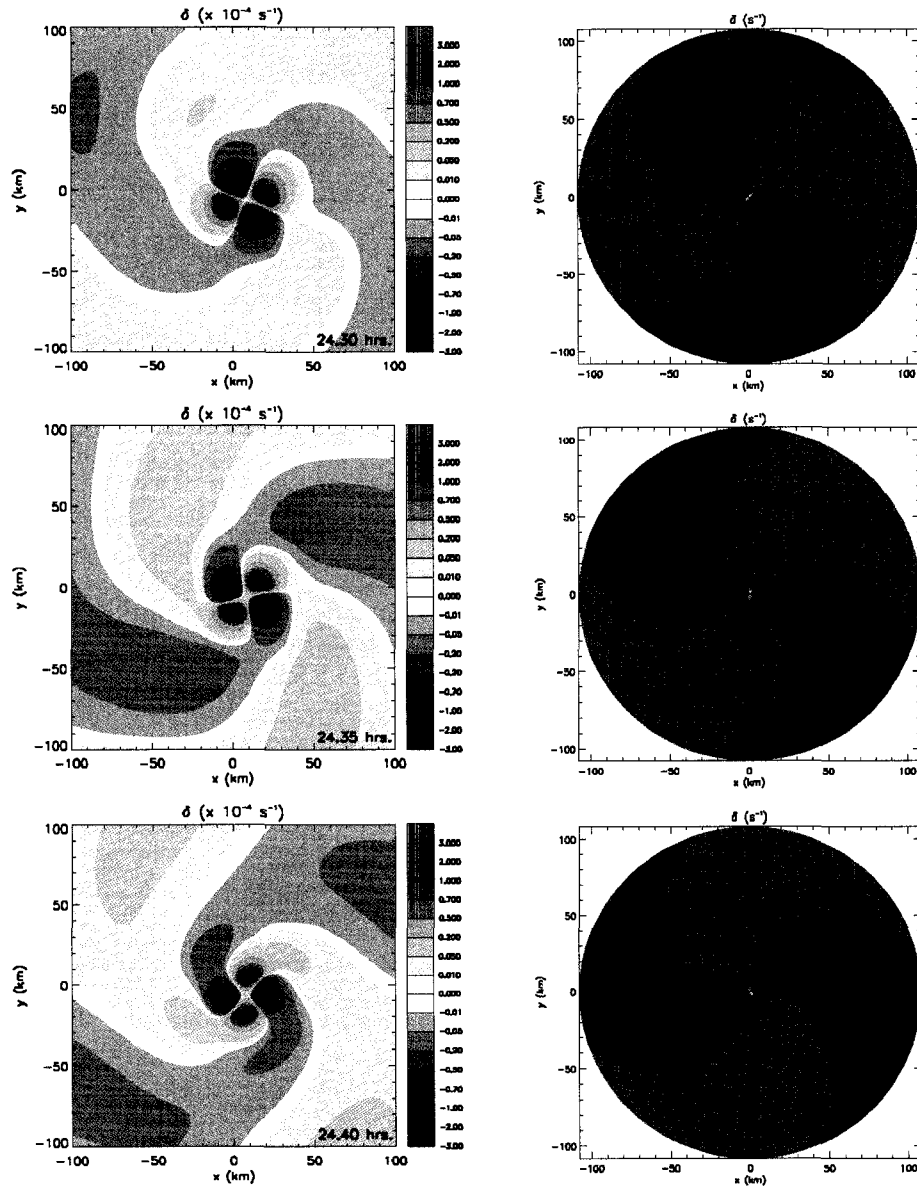


Figure 5.11: Comparison of the outward propagating IGWs in the numerical model simulation (left panels) and according to the linear wave theory (right panels). The linear solution was obtained with $k_R = 0.034 \text{ km}^{-1}$, as determined by frequency matching by ν_e , and azimuthal wavenumber $m = 2$. Moving down, each plot is 3 minutes apart.

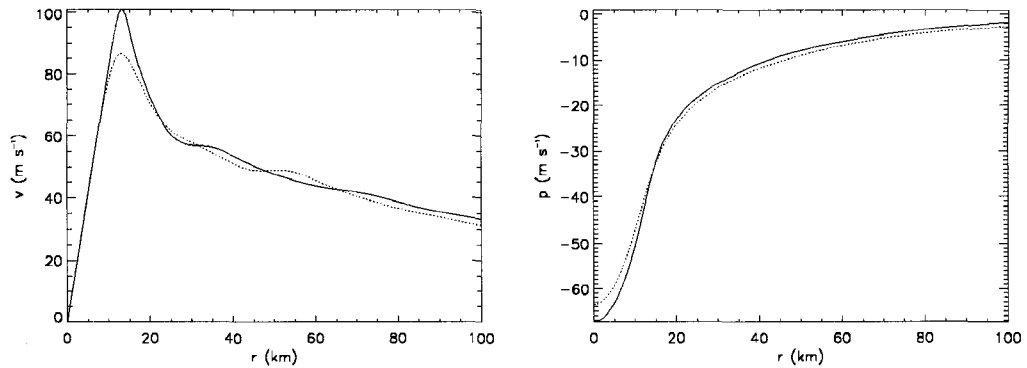


Figure 5.12: The change in the vortex azimuthal mean velocity (left panel) and pressure (right panel) over the 48 h numerical simulation. The solid line denotes $t = 0$ h and the dotted line denotes $t = 48$ h.

5.5 Conclusions

A shallow water primitive equation model simulation of a dynamically active, non-axisymmetrizing hurricane-like vortical core was analyzed. The initial condition for the simulation was an offset monopole in an elliptical vorticity ring, and was motivated by observations of elliptically shaped eyewalls in hurricanes. The initially balanced flow evolved quickly into an unbalanced state, and freely propagating IGWs radiated from the central core, which slowly became more elliptical as the simulation progressed. Spontaneous radiation was sustained for the entire length of the simulation (until $t = 48$ h), and there was no indication that it would cease shortly. The radiation was sustained because frequency matching occurred between the rapidly oscillating vorticity ellipse (or propagating wavenumber-2 vortex Rossby wave) and an intrinsic IGW. From a more pragmatic view, the mass field could not adjust to a rapidly changing wind field leading to prolonged radiation.

Simpler models were used to diagnose and explain the numerical simulation. Outside the central core, the freely propagating IGWs were explained by the linear solution to the shallow water equations about a resting basic state. The oscillation frequency of the central ellipse was nearly identical to the frequency of a simple Kirchhoff ellipse. This is strong evidence that non-axisymmetrization was largely caused by the fact that the simulated

ellipse had a sharp edge (cf. Dritschel 1998). During the simulation, the PV edge wave and IGWs grew in amplitude likely due to the positive feedback mechanism described by Schechter and Montgomery (2006). The spontaneous radiation was shown to be a sink of tangential momentum: the peak azimuthal mean swirling wind decreased 14% (from 100.8 m s^{-1} to 86.6 m s^{-1}) over 48 hours. Based on this simulation, it is possible that the sustained emission of spiral IGWs into the environment from a spontaneously radiating hurricane core is not that significant for short term intensity change. However, this result needs to be explored further through the use of total energy budgets and wave activity diagnostics.

Chapter 6

RAPID-SCAN VIEWS OF CONVECTIVELY GENERATED MESOVORTICES IN SHEARED TROPICAL CYCLONE GUSTAV (2002)

6.1 Abstract

On September 9-10, 2002, multiple mesovortices were captured in great detail by rapid-scan visible satellite imagery in Subtropical, then later, Tropical Storm Gustav. These mesovortices were observed as low-level cloud swirls while the low-level structure of the storm was exposed due to vertical shearing. They are shown to form most plausibly via vortex tube stretching associated with deep convection; they become decoupled from the convective towers by vertical shear; they are advected with the low-level circulation; finally they initiate new hot towers on their boundaries. Partial evidence of an axisymmetrizing mesovortex and its hypothesized role in the parent vortex spin up is presented.

Observations from the mesoscale and synoptic-scale are synthesized to provide a multi-scale perspective of the intensification of Gustav that occurred on September 10. The most important large scale factors were the concurrent relaxation of the 850-200 hPa deep layer vertical wind shear from 10-15 m s^{-1} to 5-10 m s^{-1} and movement over pockets of very warm sea surface temperatures (approximately 29.5°C- 30.5°C). The mesoscale observations are not sufficient alone to determine the precise role of the deep convection and mesovortices in the intensification. However, qualitative comparisons are made between the mesoscale processes observed in Gustav and recent full-physics and idealized numerical simulations to obtain additional insight.

6.2 Introduction

Two major forecasting difficulties with tropical cyclones are genesis and intensification. Forecast skill for these processes has consistently lagged forecast skill for track over the years (e.g., Sheets 1990). While general favorable (sea surface temperatures greater than 26°C, moist mid-troposphere, and presence of a pre-existing disturbance) and unfavorable (particularly strong vertical wind shear) synoptic-scale conditions affecting these processes have been well-known for some time (Gray 1968), significantly less is known about the intrinsic storm-scale dynamical and convective processes that affect genesis and intensification.

Recent studies of near cloud resolving numerical simulations run at a horizontal grid spacing of 2-3 km have added new clarity to these processes. Montgomery et al. (2006b) (hereafter MNCS) demonstrated that the incipient surface vortex could be built by small-scale cores of rotating deep convection (so-called vortical hot towers; hereafter VHTs) via the coalescence and system-scale concentration of their convectively-generated cyclonic vorticity anomalies in an idealized framework. Hendricks et al. (2004) (hereafter HMD) demonstrated a similar pathway to the genesis of a real storm, Hurricane Diana (in 1984). However, the lack of dense in-situ measurements combined with cirrus cloud canopies that tend to obscure the low-level storm structure have limited the ability to assess these and other numerical model simulations.

Tropical cyclone Gustav presented a unique opportunity to look into a developing tropical system and observe the low-level structure. The eastern portion of the storm was exposed on September 9 due to moderate easterly vertical shear, uncovering multiple mesovortices that were present. Areas of the storm were also exposed on September 10, and more of these mesovortices were visible. The evolution of these mesovortices was captured with the rapid scan visible satellite imagery. An observational analysis of this storm is presented during this period using the rapid scan imagery in conjunction with scatterometer-derived ocean surface winds and an analysis of the synoptic scale fields.

Gustav was of the class of storms that made a transition from an ordinary baroclinic cyclone to a warm-core tropical storm (tropical transition (TT); Davis and Bosart 2003, 2004; hereafter DB03, DB04, respectively) . This is in contrast to the well-known extra-tropical transition that occurs sometimes when tropical cyclones move into the higher latitudes (typically greater than 30°N). TT is physically defined as the morphing of a cold-core cyclone with baroclinic origins into a warm-core surface-based tropical cyclone (DB04). In the TT classification system of DB04, Gustav was considered initially to be a strong extratropical cyclone. In such cases, the frontal cyclone is strong enough to trigger a wind-induced surface heat exchange amplification process (WISHE; Emanuel et al. 1994). According to DB04, the TT happens via diabatic convective processes that tend to erode the pre-existing vertical wind shear and produce a warm core (cf. Montgomery and Farrell 1993).

While the main focus of this note will be a detailed illustration of the structure and evolution of the mesovortices, the observational data and QuikSCAT near-surface winds will be used to provide a multi-scale perspective of the TT that occurred. Insights into potential mechanisms of the TT will be discussed in light of this observational study.

6.3 Synoptic History: September 8-12, 2002

A detailed synoptic history of Tropical Storm Gustav is provided by the National Hurricane Center (NHC) in Miami, FL (Beven 2003). A brief summary of that report is provided here. The incipient storm formed from an area of disturbed weather between the Bahamas and Bermuda on September 6, 2002, in association with a trough. Late on September 7, 2002, a broad surface low formed in the area of disturbed weather. By 1200 UTC (Coordinated Universal Time) on September 8, the surface low was classified as a subtropical depression and was located approximately 815 km south-southeast of Cape Hatteras, North Carolina. Later that day, an Air Force Reserve Hurricane Hunter aircraft investigated the cyclone and found it had become Subtropical Storm Gustav.

On September 9, Gustav moved erratically west northwestward and slowly intensified. Gustav turned north early on September 10 and the convection became better organized near the center. The system was classified as a tropical storm by the NHC at 1200 UTC on September 10 based on the development of strong winds close to its center. As the center of Gustav reached Cape Hatteras, the maximum sustained winds increased to 28 m s^{-1} . The storm continued to intensify after interacting with the non-tropical low-pressure system and became the first hurricane of the 2002 Atlantic hurricane season at 1200 UTC on September 11. Gustav made landfall as a hurricane in Nova Scotia at 0430 UTC on September 12. After this, observations indicated that the storm was beginning to lose its tropical characteristics. Gustav lost all tropical characteristics by approximately 1200 UTC on September 12 near Newfoundland.

6.4 Data and analysis procedures

The observational products used are rapid-scan visible satellite imagery, National Center for Atmospheric Research-National Centers for Environmental Prediction (NCAR-NCEP) reanalysis data (Kalnay et al. 1996; Kistler et al. 2001), and microwave scatterometer data.

The visible imagery (Channel 1; $\lambda = 0.65 \text{ }\mu\text{m}$) is obtained from the GOES-8 storm floater on September 9-10, 2002. The approximate horizontal resolution is 1 km. The satellite was scanning in the Rapid Scan Operating (RSO) mode, with satellite images produced in 7.5-minute intervals. Gridded data is obtained from the NASA Seawinds scatterometer on board the QuikSCAT satellite during 9-10 September 2002. (More detail on the scatterometer can be found in Appendix B). The data set contains scatterometer-derived zonal and meridional vector components of the near-surface winds for a morning ascending pass and evening descending pass of the satellite over the region where Gustav developed. The NCAR-NCEP reanalysis six-hourly composite data are used for analysis of the larger-scale environment; namely vertical wind shear, thermodynamic profiles and atmospheric

moisture. The reanalysis data resolution is 2.5° by 2.5° (latitude by longitude). While this resolution is somewhat coarse, it is sufficient to broadly capture the evolution of the large-scale fields in the vicinity of Gustav.

6.5 Synoptic-scale analysis

6.5.1 *Thickness, vertical wind shear and moisture advection*

The evolution of the 850-200 hPa thickness, the 850-200 hPa vertical wind shear and the 1000 hPa horizontal moisture advection are shown in Fig. 6.1 at 1200 UTC and 0000 UTC on September 9-10. The fields are calculated from six-hourly NCAR-NCEP reanalysis data composites. The thickness is calculated by the difference between geopotential heights of the 200 hPa and 850 hPa pressure levels. The vertical wind shear is expressed by the magnitude of the difference between the horizontal velocity vectors at the 200 hPa level and 850 hPa level. The moisture advection is calculated from the specific humidity (q) and horizontal velocity vector (\mathbf{V}) from the reanalysis data, $-\mathbf{V} \cdot \nabla \mathbf{q}$, at the surface, and displayed in 12 h tendencies.

At 1200 UTC on September 9 (Fig. 6.1a), the storm was in a region of deep layer shear between $10\text{--}15 \text{ m s}^{-1}$. The low level center (marked by the “TS”) was southwest of the warm thickness center. The geostrophic vertical wind shear was approximately from the east-southeast (using thermal wind) as shown by the thickness field associated with the warm thickness center north of the storm. The strongest moisture advection was northwest of the storm at this time. Progressing to 0000 UTC on September 11 (Fig. 6.1d), the main changes in the synoptic environment were as follows: (1) the warm thickness ridge became stronger, (2) the shear weakened to less than 10 m s^{-1} and (3) the low level center became more aligned with the warm thickness center. At 1200 UTC on September 10 (12 h earlier), the synoptic environment appeared to be even more favorable, with total shear of less than 5 m s^{-1} over the storm.

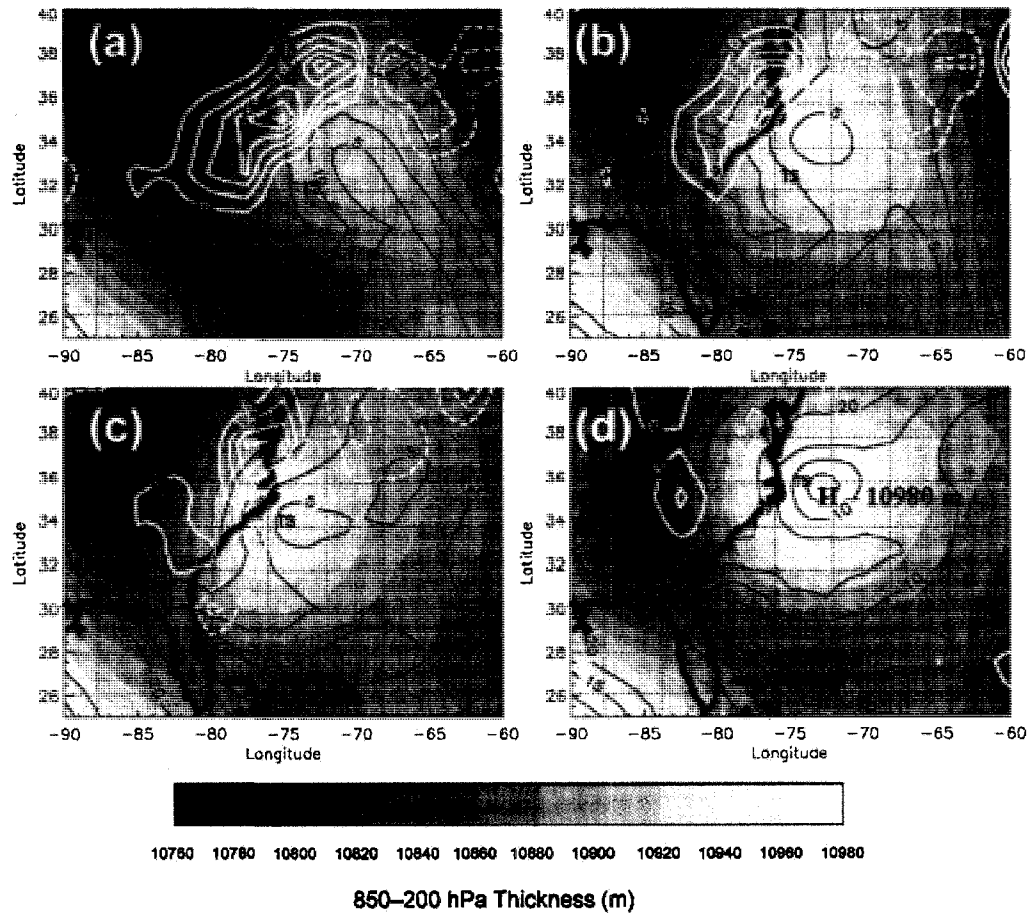


Figure 6.1: Evolution of low-level moisture advection, deep layer vertical wind shear and thickness. Moisture advection is calculated at 1000 hPa and displayed with white contours ($\text{g kg}^{-1} 12 \text{ h}^{-1}$), the 200 hPa-850 hPa vertical wind shear is plotted in the solid black lines (m s^{-1}), and the 850 hPa-200 hPa thickness is shaded, with increasing heights as lighter shades (interval is 20 m, peak is 10980 m (white), and minimum is 10750 m (black)). Panels: (a) 1200 UTC September 9, (b) 0000 UTC September 10, (c) 1200 UTC September 10, and (d) 0000 UTC September 11. The NHC best track position of Gustav is marked with a “TS” symbol

6.5.2 *Sea surface temperature*

A detailed composite of sea surface temperatures (SST) from the Advanced High Resolution Radiometer (AVHRR) on the NOAA polar-orbiting satellites in the region of Gustav is shown in Fig. 6.2 at 2215 UTC on September 8, 2002. The SSTs were shown at

this time since the storm had not yet moved over the region, and are therefore indicative of the environment into which the storm was heading (nor were the waters cooled by any previous system before Gustav). SSTs ranged from 28°C to 29°C in the storm vicinity, although small areas of higher temperatures (up to approximately 29.5-30.5°C) were seen as well.

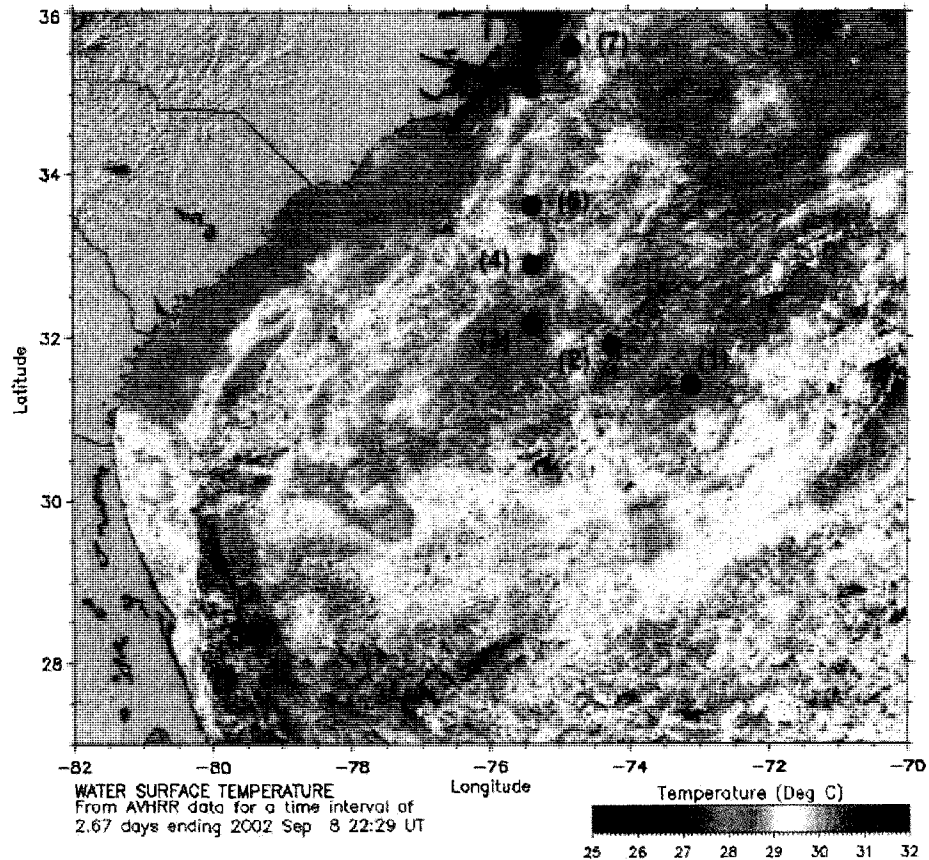


Figure 6.2: Sea surface temperatures in the region where Gustav formed (C) from the AVHRR on board the NOAA polar orbiting satellites. The NHC best track position of the storm is marked by black circles: (1) 09/1200 UTC [31.6°N, 73.6°W], (2) 09/1800 UTC [31.9°N, 74.5°W], (3) 10/0000 UTC [32.1°N, 75.5°W], (4) 10/0600 UTC [33.0°N, 75.5°W], (5) 10/1200 UTC [33.7°N, 75.4°W], (6) 10/1800 UTC [35.0°N, 75.4°W], and (7) 11/0000 UTC [35.5°N, 74.7°W] (Figure is courtesy of the Johns Hopkins University Applied Physics Laboratory.)

From 1200 UTC on September 9 to 0000 UTC on September 10 (positions 1, 2 and 3), the storm was over waters of approximately 28-29°C. From 0600 UTC on September

10 to 0000 UTC on September 11 (positions 4, 5, 6, and 7), the storm moved over the warmer pockets (29.5-30.5°C) associated with the Gulf Stream. Excluding other factors, these higher SSTs would have promoted further intensification.

6.5.3 *Near-surface winds and vorticity derived from QuikSCAT*

Four passes of QuikSCAT occurred on September 9-10. The passes were approximately twelve hours apart and include a morning ascending pass and evening descending pass on each day. The scatterometer-derived near-surface wind barbs and absolute vertical vorticity for each pass are shown in Fig. 6.3. The direction of satellite movement and the time of the pass are also shown on each plot. Absolute vertical vorticity was calculated with the zonal (u) and meridional (v) QuikSCAT wind components and the planetary vorticity, i.e., $f + dv/dx - du/dy$, with $dx = dy = 25$ km. In precipitating regions in TC cores, QuikSCAT is known to be less reliable. At certain times the shape of the TC vortex appears elliptical in Fig. 6.3. It is not known whether this shape is real or if it is caused by some erroneous QuikSCAT winds in the precipitating regions of the storm.

At 0950 UTC on September 9, a cyclonic circulation existed with wind speeds generally between 10-15 m s⁻¹. By 2351 UTC, some moderate strengthening was seen on the western side of the center (Fig. 6.3b, marked by the "TS") (winds approximately 15-20 m s⁻¹), while winds were more or less steady elsewhere. At 1106 UTC on September 10, the area of stronger winds was gone, and generally, maximum winds were approximately 10-15 m s⁻¹. In the final pass, significant strengthening of the storm was observed; low-level winds increased to approximately 15-25 m s⁻¹. The QuikSCAT data indicate that Gustav was not changing significantly in intensity on 9 September, and then it began to intensify on September 10, particularly after 1200 UTC. The peak absolute vertical vorticity was approximately 60×10^{-5} s⁻¹ on September 9 (both passes; Figs. 6.3a and 6.3b). The 1107 UTC pass (Fig. 6.3c) on September 10 yielded the largest peak absolute vorticity, 80×10^{-5} s⁻¹. The peak values on the final pass on that day were smaller, 40×10^{-5} s⁻¹. QuikSCAT

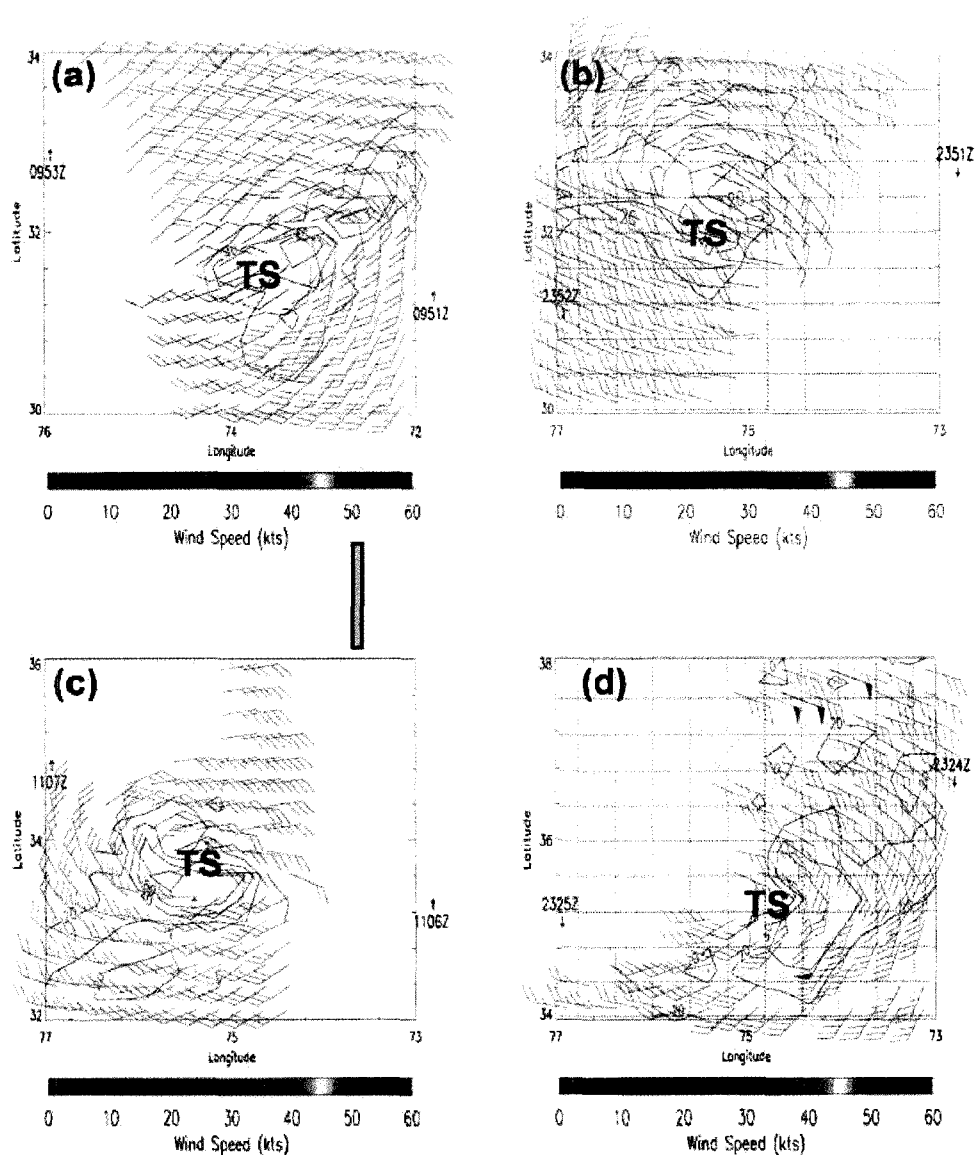


Figure 6.3: Near-surface wind barbs and absolute vertical vorticity (in units of 10^{-5} s^{-1}) derived from the QuikSCAT scatterometer during 9-10 September 2002. Each contour represents an interval of $20 \times 10^{-5} \text{ s}^{-1}$. Panels: (a) ascending pass at 0950 UTC September 9, (b) descending pass at 2350 UTC September 9 (c) ascending pass at 1106 UTC September 10, and (d) descending pass at 2325 UTC September 10. The NHC best track storm center fix is marked by the “TS” symbol. The direction of satellite movement and the UTC time of the eastern and western edge of the pass are also marked on the plot.

winds (and vorticity) were not available on the western portion of the storm at this time since this area was over land (North Carolina). The larger values on Fig. 6.3c may be a

signature of one of the mesovortices on September 10 (see section 6.3). However, due to the coarse QuikSCAT resolution of 25 km, the mesovortex vorticity is not resolved. In comparison to the NHC best track intensity estimate, QuikSCAT near-surface winds were slightly lower throughout this period. The NHC best track intensities were: 21 m s⁻¹ (1200 UTC on September 9), 23 m s⁻¹ (0000 UTC September 10), 26 m s⁻¹ (1200 UTC September 10), and 28 m s⁻¹ (0000 UTC September 11).

6.5.4 Discussion

Based on the analysis above, it is concluded that the synoptic environment became more favorable on September 10. The main favorable changes were the concurrent relaxing of the 850-200 hPa vertical wind shear from 10-15 m s⁻¹ to 5-10 m s⁻¹ combined with storm movement over very warm waters. The moisture advection was maximized northwest of the storm center, and was likely the primary contributor to the sustained deep convective activity in that area. According to DB04, the environmental vertical wind shear can be reduced in subtropical storms such as Gustav by diabatic processes in sustained deep convection. It is possible that the vertical wind shear reduction that occurred in Gustav may have proceeded via this pathway. However, we also cannot rule out the shear reduction being caused by the evolving large-scale environment.

The relatively high 850-200 hPa thickness values over the storm indicate that the cold-core system had already eroded substantially by September 9. However, the movement of the surface low beneath the warm thickness center did not occur until approximately 1200 UTC on September 10 (Fig. 6.1c). The QuikSCAT data indicates that the strongest low-level wind increase occurred between approximately 1200 UTC on September 10 and 0000 UTC on September 11 (Figs. 6.3c and Figs. 6.3d). The timing of the tropical transition cannot be determined explicitly because of the lack of temperature time history in the storm core and also spatial uncertainty in the reanalysis fields. However, a warm-core had probably formed by 1200 UTC on September 10, since this was the time of the most

significant low-level wind spin-up.

6.6 Mesoscale analysis

6.6.1 *Observed convection*

Having now summarized the synoptic scale conditions, we turn our focus to the mesoscale and convective scale conditions. Multiple hot towers were observed in Gustav on September 9-10, 2002. They are evident as overshooting tops in Fig. 6.4, along with two exposed mesovortices (discussed in section 6.2). The hot towers are found to grow and die with lifetimes of approximately 0.5-1.0 h. The rapid-scan imagery was used to obtain vertical velocity estimates in these towers, and vertically-averaged (through the troposphere) updrafts of approximately 10 m s^{-1} were found. These were spatially and temporally averaged updrafts, therefore velocities in excess of this value are expected to peak in the middle and upper troposphere (e.g., Zipser and Gautier 1978; Zipser 2003) and in more localized regions. The deep convection initiated from an unstable moist air mass. The most indicative sounding is the MHX (Newport, NC) sounding at 1200 UTC on September 10, shown in Fig. 6.5. Surface-based CAPE (based on pseudo-adiabatic parcel ascent) from this sounding is approximately 1000 J kg^{-1} .

6.6.2 *Structure and evolution of mesovortices*

Close-up images of Gustav are shown on September 9 in Fig. 6.6 at 1815 UTC and 1945 UTC. Two distinct mesovortices are visible at each time, and a third one emerges just before dark (not shown). While there is no easy method for determining the horizontal scale of the mesovortices, they appear to be approximately 25-45 km in horizontal scale from their velocity signatures (low-level cloud swirls) in Fig. 6.6. The vorticity signatures of these mesovortices (or the horizontal extent of an isolated region of elevated vorticity) are likely smaller. For example, Reasor et al. (2005) (hereafter RMB) found near-hurricane-strength low-level vorticity regions in pre-storm Hurricane Dolly (1996) at very small scales

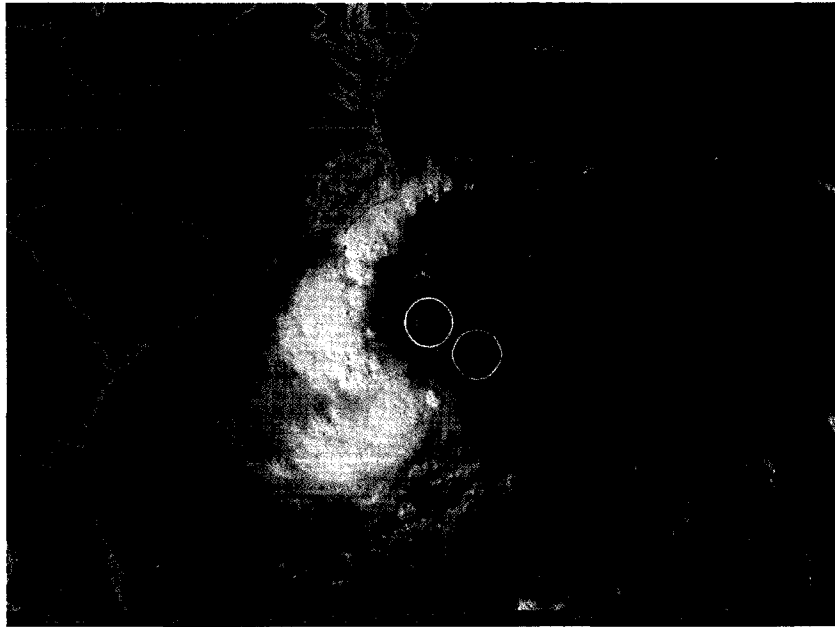


Figure 6.4: Large-scale visible satellite image of Gustav at 1945 UTC on Sept 9. Multiple hot towers and two exposed mesovortices are evident

(10-20 km) using airborne Doppler radar. The scales of the deep convective regions (defined by the width of the cloud shield just prior to the anvil stage) are approximately at the MV scale (25-45 km; see Fig. 6.6). These mesovortices are found to emerge from underneath the deep convection and move with the low level winds (Fig. 6.6, white arrows). For example, at 1815 UTC, MV2 has just emerged from the sustained deep convective activity to the west. The exposure of the mesovortices from the convective towers is due to the moderate vertical shear at this time.

In summary, since, (1) the mesovortices are close to the same scale of the deep convective areas (Fig. 6.6), (2) there are no islands in the vicinity, (3) they emerge as low-level circulations immediately after and from underneath the deep convective bursts, it is most likely that the mesovortices were generated via vortex stretching by updrafts in the deep convective cores. This convective coupling is observed more clearly in the animation of the 7.5-minute rapid-scan imagery on 9 September on the Internet website, <http://wx.met.nps.navy.mil/mtmontgo/GustavAnimations/>. The QuikSCAT data in-

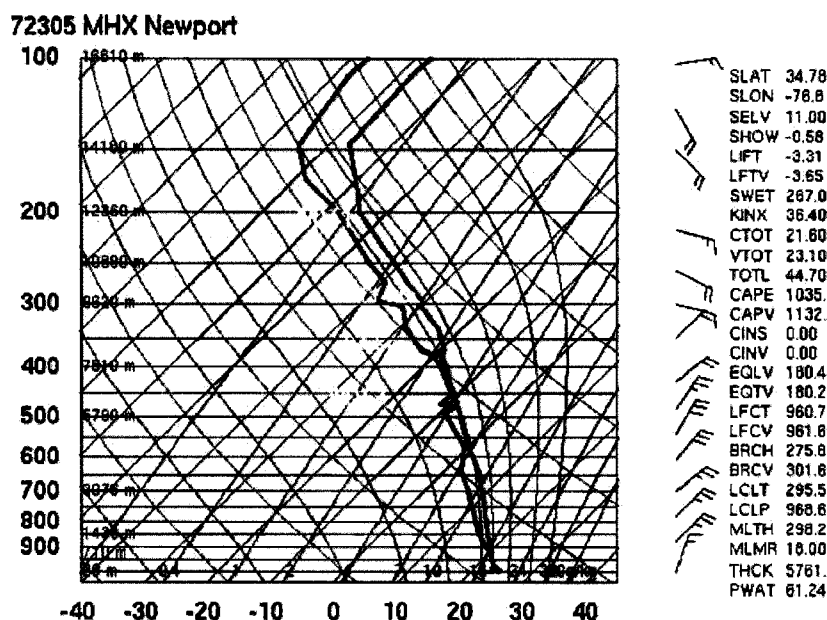


Figure 6.5: Representative sounding from of inflow air into Gustav on September 10 (courtesy of the University of Wyoming)

indicates that Gustav formed in a vorticity-rich environment, with a large area of near-surface absolute vertical vorticity greater than $2 \times 10^{-4} \text{ s}^{-1}$. This reservoir was likely utilized by the convective towers.

When Gustav became a tropical storm on September 10, two more mesovortices were strikingly visible (Fig. 6.7, marked MV4 and MV5). The satellite imagery indicates that these mesovortices were rotating around one another from at least 1445 UTC until 1900 UTC. At 1925 UTC, MV5 is no longer visible and MV4 appears to become the dominant vortex. A gigantic convective burst was initiated by MV4 with a circular exhaust cloud (Gentry et al. 1970) of horizontal scale of approximately 50-70 km (the early stages are shown at 1925 UTC in Fig. 6.7b). After this, sustained deep convection was present over the center of Gustav and the next day it was classified as a hurricane by the NHC. Due to the onset of darkness and increasing cloud cover, it is not known whether MV5 was expelled from the storm, merged into MV4, or dissipated. Subsequent to this, MV4 appeared to become the new circulation center, as has been shown in previous cases (Stossmeister and

Barnes 1992).

The convective generation of mesovortices is well documented in the literature (Marks et al. 1992; Stossmeister and Barnes 1992; Fritsch et al. 1994; Reasor et al. 2005). Fritsch et al. (1994) demonstrated the formation of a mesovortex (with an initial scale of approximately 100 km in diameter) over land via CAPE, without heat and moisture fluxes from the sea surface. Stossmeister and Barnes (1992) linked the formation of a second circulation center in Tropical Storm Isabel (1985) to intensifying deep convection in a rain band spiraling from the original center. RMB also demonstrated that the formation of circulations in the pre-Hurricane Dolly (1996) disturbance likely proceeded via vortex tube stretching in association with hot tower convection.

These mesovortices form from a different process than in mature hurricane eyewalls (Kossin and Schubert 2004). The latter are believed to form principally from a barotropic instability that necessarily requires a sign reversal of the local radial gradient of absolute vertical vorticity (Schubert et al. 1999). The Gustav mesovortices formed in an area where the vorticity distribution was approximately monotonic with radius from the circulation center, and thus formation by barotropic instability is not plausible.

6.6.3 Partial evidence of system-scale axisymmetrization

The visible imagery provided partial evidence of the axisymmetrization of one mesovortex into the larger scale vortex circulation (Fig. 6.8). As night began at 2125 UTC on September 9, MV1 appeared to be strained and elongated from its earlier circular structure (see Fig. 6.6). The straining and elongating of MV1 is consistent with the early phase of the axisymmetrization process of convectively generated vorticity anomalies leading to strengthening of the larger-scale (parent) vortex (Montgomery and Kallenbach 1997; Montgomery and Enagonio 1998; Melander et al. 1988; Dritschel and Waugh 1992). Based on available data, however, it is impossible to determine conclusively whether axisymmetrization of this anomaly occurred, since night fell and it moved underneath the convection. Shortly after

MV1 moved underneath the convection, a large convective burst occurred over it, possibly indicating an intensification trend. MV1 was the only mesovortex that was observed to have strained and elongated.

6.7 Summary

Mesoscale and synoptic scale observations of tropical storm Gustav were synthesized to provide a multi-scale perspective of the tropical transition (TT) that occurred on September 9-10, 2002. On the mesoscale, rapid scan visible satellite imagery from GOES-8 was used to illustrate and examine multiple mesovortices that existed in the storm on both of these days. The origin of these mesovortices was strongly suggested to be from vortex tube stretching due to their emergence from underneath deep convective regions soon after convective events. They became visible as low-level cloud swirls on September 9 due to easterly/southeasterly deep layer shear of approximately $10\text{-}15\text{ m s}^{-1}$. Partial evidence of the axisymmetrization of one mesovortex into the parent vortex circulation was suggested with the rapid scan visible satellite imagery in the evening of September 9. Two more mesovortices were visible on September 10, while Gustav was a strong tropical storm. On both days, new hot towers were observed to form on the boundaries of existing mesovortices (MV1 on September 9 and MV4 on September 10).

The synoptic-scale analysis of vertical wind shear, sea surface temperature and moisture indicated that the environment was unfavorable for tropical cyclone formation on September 9, but became favorable on September 10. This was due to the concurrent relaxation of the 850-200 hPa vertical wind shear from $10\text{-}15\text{ m s}^{-1}$ to $5\text{-}10\text{ m s}^{-1}$ combined with storm movement over very warm SSTs ($29.5\text{ }^{\circ}\text{C}$ - $30.5\text{ }^{\circ}\text{C}$) associated with the Gulf Stream. The spin-up of near surface winds from $10\text{-}15\text{ m s}^{-1}$ to $20\text{-}30\text{ m s}^{-1}$ from 1200 UTC on September 10 to 0000 UTC on September 11 (observed by QuikSCAT) indicates that the TT of Gustav probably had completed by this time. QuikSCAT background absolute vertical vorticity was found to be approximately $1\text{-}2 \times 10^{-4}\text{ s}^{-1}$ with peak values of

approximately $5-8 \times 10^{-4} \text{ s}^{-1}$. An accurate representation of the mesovortex vorticity was not possible since the QuikSCAT resolution was too coarse (25 km).

The observations presented herein are not sufficient to determine the precise role of the convective mesovortices in the TT of Gustav. However, recent numerical simulations link warm core formation and tangential momentum spin-up tendencies to these asymmetric eddy processes (MNCS, HMD and Montgomery and Enagonio (1998)). Perhaps the most interesting aspect of this study is the illustration of the low level complex flow patterns in a developing tropical cyclone, as well as the likelihood that convectively generated mesovortices exist in many tropical cyclones. Denser in-situ observations and airborne Doppler radar will be necessary to observationally determine the relative importance of convective-scale eddy processes versus storm-scale mean processes in the genesis and intensification of tropical cyclones.

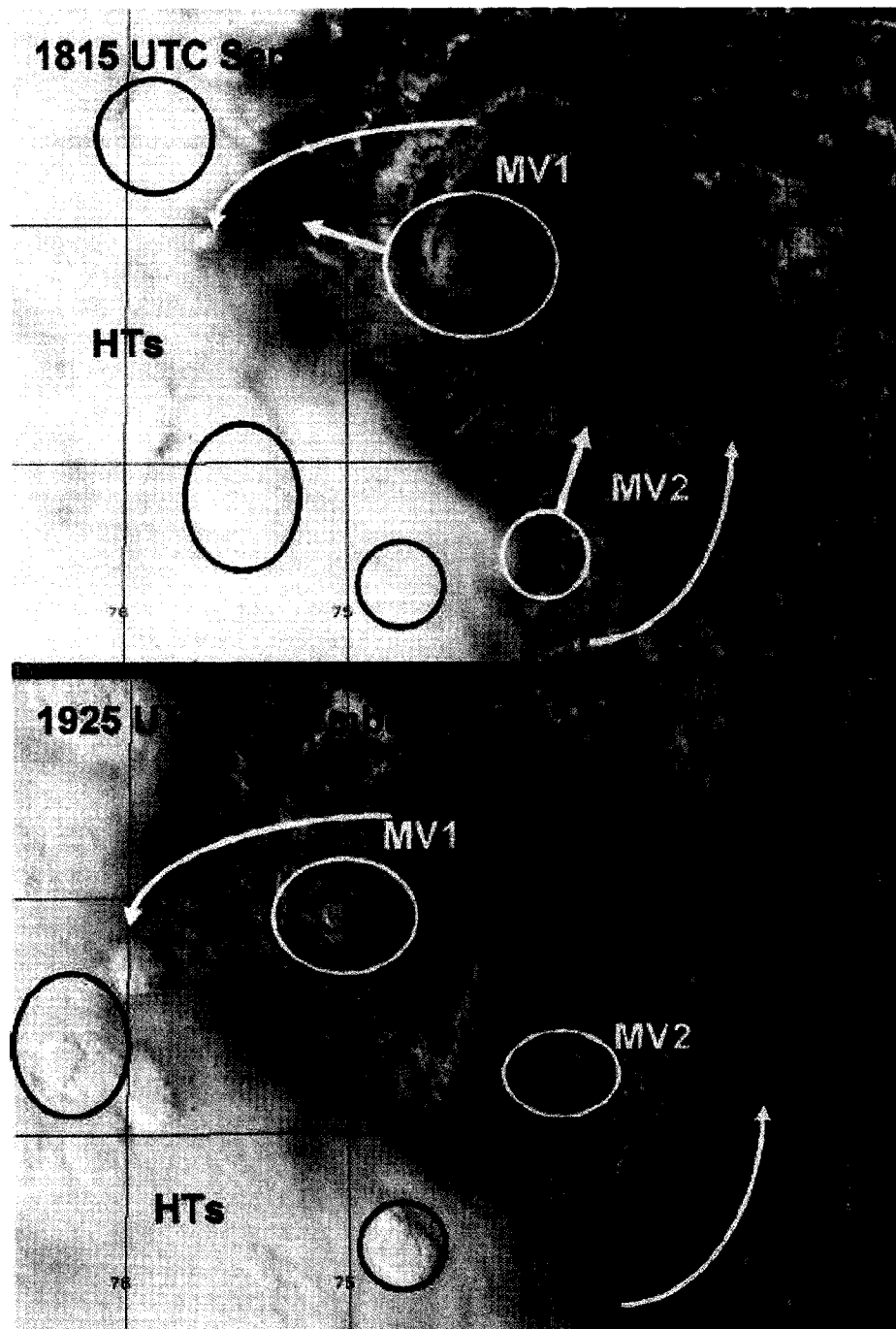


Figure 6.6: GOES-8 visible close-up depiction of mesovortices in Gustav at 1815 and 1945 UTC on September 9. The overshooting convective tops associated with multiple hot towers are circled in black and marked “HTs”. The low level exposed mesovortices are circled in white and marked with “MV”. The low level motion of the MVs is shown by the white arrows. The approximate scales of the structures can be discerned from the scale of the latitude-longitude box: 32-33° N (110 km) by 74-75° E (94 km). The system-scale low-level circulation is shown by the white arrows.



Figure 6.7: Mesovortices in T.S. Gustav on September 10. Panels: (a) 1615 UTC September 10, (b) 1925 UTC September 10

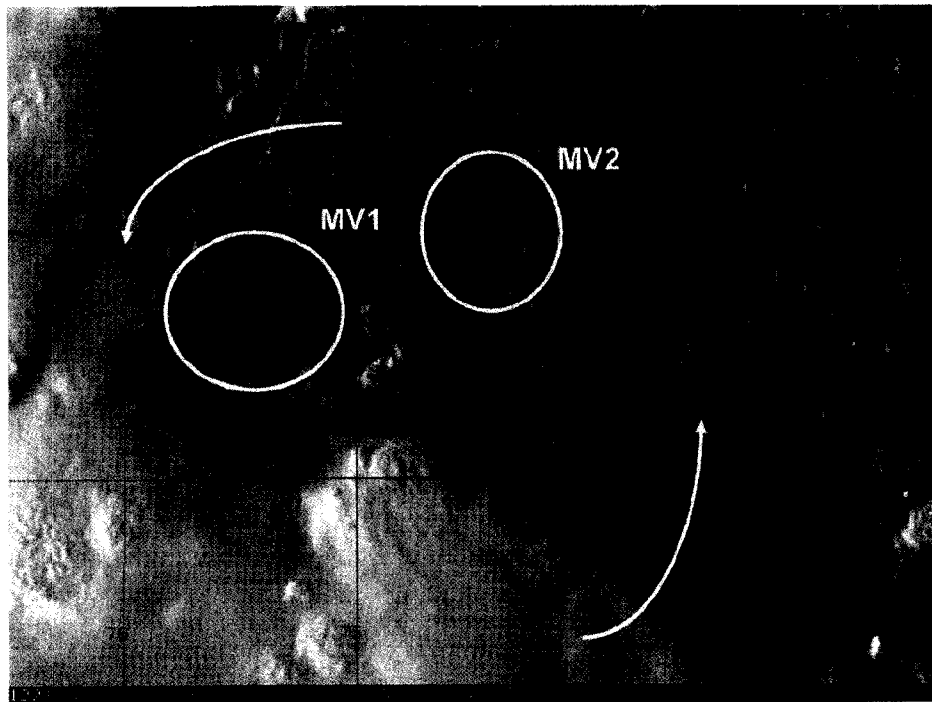


Figure 6.8: Partial evidence of the axisymmetrization of a low level mesovortex. At 2125 UTC 9 Sept 2002, MV1 appears to be strained and elongated from its earlier circular structure. The broader low level circulation is shown by the white arrows.

Chapter 7

CONCLUSIONS

Tropical cyclones (TCs) may change in structure and intensity due to environmental factors, ocean surface fluxes, and internal dynamics. In this dissertation, aspects of the evolution of TCs solely due to internal dynamical processes has been assessed. The first part of the dissertation focused on idealized studies of transport and mixing in the hurricane inner-core, and the second part was devoted to understanding some specific asymmetric dynamics of TC evolution: spontaneous radiation from active TC cores and vortical hot towers in TC genesis and intensity change. A hierarchical modeling approach (from the nondivergent barotropic model to the hydrostatic primitive equation model) was undertaken, and diagnostics and observations were also used. The principle finding is that internal dynamics are as significant as environmental factors and ocean surface fluxes in governing short term intensity change of hurricanes.

In chapter 2, the effective diffusivity diagnostic was used to map out the transport and mixing properties of idealized barotropic hurricane-like vortices. Complementing its previous use in simple time-periodic flows and stratospheric dynamics, effective diffusivity was found to be a useful tool to diagnose two-dimensional mixing in hurricanes. Potential vorticity (PV) wave breaking events occur often in hurricanes, either due to barotropic instability or during axisymmetrization of anomalies on monotonic vortices. These breaking PV waves create finite radial length chaotic mixing regions (surf zones) in the vortex. For monotonic vortices, the surf zone outside the radius of maximum wind is analogous to the surf zone outside the wintertime stratospheric polar vortex. During PV wave breaking

events, passive tracers can be easily mixed over large horizontal distances in the hurricane. An interesting result for unstable PV rings is that the hurricane tangential jet appears to be a robust transport barrier in certain instances, even though the inner and outer PV waves are breaking. The inner, breaking PV wave is quite effective at mixing passive tracers between the outer edge of the eye and the eyewall. Assuming a monotonically decreasing equivalent potential temperature profile with radius at low levels, these results support the hurricane superintensity mechanism.

In chapter 3, a systematic study of structural and intensity change of all possible dynamically unstable hurricane-like vortices (i.e., PV rings) was performed. A sequence of 170 numerical simulations was executed covering a parameter space with the first parameter being the thickness of the ring (i.e., the ratio of the inner and outer radii) and the second parameter being the hollowness of the ring (i.e., the ratio of the eye vorticity to the average inner-core vorticity). In approximately one-half the cases, the ring became dynamically unstable and a vigorous PV mixing episode occurred between the eyewall and eye. The observed most unstable mode in the numerical model was compared to linear theory, and resultant end states after the nonlinear advection and mixing were assessed. During all PV mixing events, both the central pressure and maximum mean tangential velocity simultaneously decreased. Thus empirical pressure-wind relationships are invalid during PV mixing events. Rapid pressure falls were found to occur for the barotropic breakdown of very thin rings; thus PV mixing can be a factor in rapid intensification. Based on these results, the use of maximum sustained wind as a metric for hurricane intensity is strongly discouraged. Rather, minimum central pressure or integrated kinetic energy should be used. Additionally, rapid intensification of hurricanes should be assessed in terms of pressure, not winds, and should be referred to as rapid deepening.

In chapter 4, two idealized hydrostatic primitive equation mesoscale models were described and some evaluation tests were presented. The vertically discrete models were created from a preexisting periodic spectral shallow water model. The first model used an

isentropic vertical coordinate and the second model used a sigma (terrain following) vertical coordinate. Both models were extended on a Charney-Phillips grid, and include options for horizontal momentum and vorticity-divergence prognostic formulations. Evaluation tests were presented for the isentropic model: gradient adjustment in an axisymmetric baroclinic hurricane-like vortex and the quasi-balanced evolution of a dynamically unstable hurricane-like vortex (i.e., a PV hollow tower). A “PV bridge” formed across the eye at low levels due to PV mixing preferentially at lower levels. This was an interesting result because the bridge had previously been simulated in a moist full-physics model. Since a portion of the PV in the bridge is static stability, it is possible that the hurricane eye inversion is *dynamically controlled*, making it potentially the only such inversion on Earth of this nature. In addition, an initially erect PV hollow tower evolved into a tilted structure, suggesting one mechanism by which the eyewall slope forms is adiabatic PV mixing. The sigma coordinate model is not yet complete, but it will ameliorate some problems found in the isentropic model, namely the bending of theta surfaces into the ground for strong hurricane-like vortices.

In chapter 5, spontaneous inertia-gravity wave (IGW) radiation from atmospheric vortices was advanced by examining a case study of an active hurricane-like core in a shallow water model. An initially balanced state of an offset monopole in an elliptically shaped eyewall evolved into a unbalanced (or quasi-balanced) spontaneous radiative state. The central monopole was deformed into an ellipse, and it began to rapidly rotate. The mass field could not adjust to the rapidly oscillating wind field, and spontaneous adjustment emission ensued. Frequency matching occurred between a PV edge wave and a intrinsic IGW (analogous to Lighthill radiation), causing radiation to the environment at a preferred radial wavenumber. The radiation was sustained because the central ellipse would not axisymmetrize, due almost entirely to the fact that it had a sharp edge. The multitude of low wavenumber vorticity structures that are observed and simulated in numerical models suggest that spontaneous radiation is likely often occurring in hurricanes (even in the absence of gravity wave generation by moist convection), affecting its own intensity and disrupting

the local environment. Future work will be devoted to understanding whether spontaneous radiation is a significant for hurricane intensity change.

In chapter 6, an observational case study of vortical hot towers (VHTs) in tropical cyclone Gustav (2002) was examined, building on previous full-physics numerical modeling work linking VHTs as fundamental building blocks of seedling TC vortices. Multiple convectively generated mesovortices were observed as low level cloud swirls after being decoupled from the VHTs due to moderate vertical shear. The exposure, we feel, uncovered an inherent eddy-driven intensification mechanism by VHTs that is likely occurring in many, if not all, hurricanes. The observed evolution of the mesovortices was compared to full-physics numerical simulations suggesting the multiple mergers and axisymmetrization of these anomalies can create a seedling TC vortex, with a secondary circulation enhancement from the aggregate diabatic heating from all the VHTs.

In this dissertation, the role of barotropic dynamics in TC evolution has been emphasized. Outside localized deep convective regions, the combined effects of stratification and rotation tend to make the hurricane behave as a two-dimensional, layered, quasi-balanced system. The important modes of variability in such flows are the low frequency vortex Rossby waves, which we have shown to be significant in affecting hurricane structure and intensity change on short time scales (less than 48 h). Much insight into hurricane dynamics in this dissertation has been obtained by simple, idealized models. In closing, we note the quote from Ian James: “Comprehensive complexity is no virtue in modeling, but rather, an admission of failure.”

APPENDIX A

Volume Coordinate Transformation for Effective Diffusivity

The effective diffusivity area-based coordinate becomes a volume-based coordinate for a three dimensional nondivergent flow. To illustrate this, consider the Bousinessq equations on an f -plane:

$$\frac{\partial u}{\partial t} + \mathbf{u} \cdot \nabla u - fv = \nu \nabla^2 u - \frac{1}{\rho} \frac{\partial p}{\partial x}, \quad (\text{A.1})$$

$$\frac{\partial v}{\partial t} + \mathbf{u} \cdot \nabla v + fu = \nu \nabla^2 v - \frac{1}{\rho} \frac{\partial p}{\partial y}, \quad (\text{A.2})$$

$$\frac{\partial w}{\partial t} + \mathbf{u} \cdot \nabla w = \nu \nabla^2 w - \frac{1}{\rho_0} \frac{\partial p}{\partial z} + g \frac{\rho'}{\rho_0} \quad (\text{A.3})$$

$$\nabla \cdot \mathbf{u} = 0, \quad (\text{A.4})$$

where u is zonal momentum, v is the meridional momentum, p is the pressure, ν is the momentum diffusivity, and ∇ is a three dimensional operator. A passive tracer $c(x, y, z, t)$ in this flow must satisfy

$$\frac{\partial c}{\partial t} + \mathbf{u} \cdot \nabla c = \nabla \cdot (\kappa \nabla c), \quad (\text{A.5})$$

where κ is the tracer diffusivity.

Let C denote a particular surface of the $c(x, y, z, t)$ field and $V(C, t)$ denote the volume of the region in which the tracer concentration satisfies $c(x, y, z, t) \geq C$, i.e.,

$$V(C, t) = \iiint_{c \geq C} dx dy dz. \quad (\text{A.6})$$

Let $\gamma(C, t)$ denote the bounding surface of this volume. Note that $V(C, t)$ is a monotonically decreasing function of C and that $V(C_{\max}, t) = 0$. Now define \mathbf{u}^C as the velocity of the bounding surface C , so that

$$\frac{\partial c}{\partial t} + \mathbf{u}^C \cdot \nabla c = 0. \quad (\text{A.7})$$

Let dA be an area element on the surface C . Noting that $\nabla c/|\nabla c|$ is the unit vector normal to the contour, we can use (A.6) and (A.7) to write

$$\begin{aligned}\frac{\partial V(C, t)}{\partial t} &= \frac{\partial}{\partial t} \iiint_{c \geq C} dx dy dz \\ &= - \iint_{\gamma(C, t)} \mathbf{u}^C \cdot \frac{\nabla c}{|\nabla c|} dA \\ &= \iint_{\gamma(C, t)} \frac{\partial c}{\partial t} \frac{dA}{|\nabla c|},\end{aligned}\tag{A.8}$$

where dA is an area element on the bounding surface. Using (A.5) in the last equality of (A.8) we obtain

$$\begin{aligned}\frac{\partial V(C, t)}{\partial t} &= \iint_{\gamma(C, t)} \nabla \cdot (\kappa \nabla c) \frac{dA}{|\nabla c|} \\ &\quad - \iint_{\gamma(C, t)} \mathbf{u} \cdot \nabla c \frac{dA}{|\nabla c|}.\end{aligned}\tag{A.9}$$

We now note that (since $dx dy, dz = dA dC' / |\nabla c|$)

$$\begin{aligned}\frac{\partial}{\partial C} \iiint_{c \geq C} () dx dy dz &= \frac{\partial}{\partial C} \iiint_{c \geq C} () \frac{dA dC'}{|\nabla c|} \\ &= - \iint_{\gamma(C, t)} () \frac{dA}{|\nabla c|}.\end{aligned}\tag{A.10}$$

Using (A.10) in (A.9) while noting that $\mathbf{u} \cdot \nabla c = \nabla \cdot (c\mathbf{u})$ because \mathbf{u} is nondivergent, we obtain

$$\begin{aligned}\frac{\partial V(C, t)}{\partial t} &= - \frac{\partial}{\partial C} \iiint_{c \geq C} \nabla \cdot (\kappa \nabla c) \frac{dA dC'}{|\nabla c|} \\ &\quad + \frac{\partial}{\partial C} \iiint_{c \geq C} \nabla \cdot (c\mathbf{u}) \frac{dA dC'}{|\nabla c|} \\ &= - \frac{\partial}{\partial C} \iint_{\gamma(C, t)} \kappa |\nabla c| dA \\ &\quad + \frac{\partial}{\partial C} \iint_{\gamma(C, t)} c\mathbf{u} \cdot \frac{\nabla c}{|\nabla c|} dA.\end{aligned}\tag{A.11}$$

The third and fourth lines of (A.11) are obtained using the divergence theorem. The fourth line of (A.11) vanishes because the factor c in the integrand can come outside the integral, leaving $\iint_{\gamma(C, t)} \mathbf{u} \cdot (\nabla c/|\nabla c|) dA$, which vanishes because \mathbf{u} is nondivergent.

Since $V(C, t)$ is a monotonic function of C , there exists a unique inverse function $C(V, t)$. We now transform (A.11) from a predictive equation for $V(C, t)$ to a predictive

equation for $C(V, t)$. This transformation is aided by

$$\frac{\partial V(C, t)}{\partial t} \frac{\partial C(V, t)}{\partial V} = - \frac{\partial C(V, t)}{\partial t}, \quad (\text{A.12})$$

which, when used in (A.11), yields

$$\begin{aligned} \frac{\partial C(V, t)}{\partial t} &= \frac{\partial C(V, t)}{\partial V} \frac{\partial}{\partial C} \iint_{\gamma(C, t)} \kappa |\nabla c| dA \\ &= \frac{\partial}{\partial V} \iint_{\gamma(C, t)} \kappa |\nabla c| dA. \end{aligned} \quad (\text{A.13})$$

Because of (A.10), the integral $\iint_{\gamma(C, t)} \kappa |\nabla c| dA$ on the right hand side of (A.13) can be replaced by $(\partial/\partial C) \iiint_{c \geq C} \kappa |\nabla c|^2 dx dy dz$. Then, (A.13) can be written in the form

$$\frac{\partial C(V, t)}{\partial t} = \frac{\partial}{\partial V} \left(K_{\text{eff}}(V, t) \frac{\partial C(V, t)}{\partial V} \right), \quad (\text{A.14})$$

where

$$K_{\text{eff}}(V, t) = \left(\frac{\partial C}{\partial V} \right)^{-2} \frac{\partial}{\partial V} \iiint_{c \geq C} \kappa |\nabla c|^2 dx dy dz. \quad (\text{A.15})$$

APPENDIX B

NASA SeaWinds Scatterometer

The SeaWinds scatterometer is a microwave radar sensor used to measure the reflection or scattering effect produced while scanning the surface of oceans and gives an estimate of the near-surface winds. The instrument provides measurements over a 1,800 km swath during each orbit and covers 90 percent of the Earth's oceans every day. Surface wind speeds are measured in the range of 3 to 20 m s⁻¹ with an accuracy of 2 m s⁻¹ for magnitude and 20 degrees for direction. The horizontal resolution of the retrieved wind vectors is 25-km. More information on the Seawinds scatterometer can be found on the internet website: <http://winds.jpl.nasa.gov/> and more information on the level 3 gridded data set from QuikSCAT can be found on the internet website:

<http://podaac.jpl.nasa.gov/products/product109.html/>.

BIBLIOGRAPHY

- Aberson, S. D., M. Montgomery, M. Bell, and M. Black, 2006: Hurricane Isabel (2003). new insights into the physics of intense storms. Part II: Extreme localized wind. *Bull. Amer. Meteor. Soc.*, **1349**–1354.
- Allen, D. R. and N. Nakamura, 2001: A seasonal climatology of effective diffusivity in the stratosphere. *J. Geophys. Res.*, **106**, 7917–7935.
- Arakawa, A. and S. Moorthi, 1988: Baroclinic instability in vertically discrete systems. *J. Atmos. Sci.*, **45**, 1688–1707.
- Aref, H., 1984: Stirring by chaotic advection. *J. Fluid Mech.*, **143**, 1–21.
- Beven, J. L., 2003: Tropical cyclone report: Hurricane Gustav. National Hurricane Center archives. <http://www.nhc.noaa.gov/2002gustav.shtml>.
- Bowman, K. P., 1993: Barotropic simulation of large-scale mixing in the Antarctic polar vortex. *J. Atmos. Sci.*, **50**, 2901–2914.
- Bowman, K. P., 1995: Diffusive transport by breaking waves. *J. Atmos. Sci.*, **52**, 2417–2427.
- Bowman, K. P. and P. Chen, 1994: Mixing by barotropic instability in a nonlinear model. *J. Atmos. Sci.*, **51**, 3692–3705.
- Braun, S. A., M. T. Montgomery, and Z. Pu, 2006: High-resolution simulation of Hurricane Bonnie (1998). Part I: The organization of eyewall vertical motion. *J. Atmos. Sci.*, **63**, 19–42.
- Butchart, N. and E. E. Remsberg, 1986: Area of the stratospheric polar vortex as a diagnostic for tracer transport on an isentropic surface. *J. Atmos. Sci.*, **43**, 1319–1339.
- Charney, J. G. and N. A. Phillips, 1953: Numerical integration of the quasi-geostrophic equations for barotropic and simple baroclinic flows. *J. Meteor.*, **10**, 71–99.
- Chen, Y. and M. K. Yau, 2001: Spiral bands in a simulated hurricane. part 1: Vortex Rossby wave verification. *J. Atmos. Sci.*, **58**, 2128–2145.
- Chow, K. C. and K. L. Chan, 2004: Angular momentum transports by moving spiral waves. *J. Atmos. Sci.*, **60**, 2004–2009.
- Chow, K. C., K. L. Chan, and A. K. H. Lau, 2002: Generation of moving spiral bands in tropical cyclones. *J. Atmos. Sci.*, **60**, 2930–2950.

- Corbosiero, K. L., J. Molinari, A. R. Aiyyer, and M. L. Black, 2006: The structure and evolution of Hurricane Elena (1985). Part II: Convective asymmetries and evidence for vortex Rossby waves. *Mon. Wea. Rev.*, **134**, 3073–3091.
- Cram, T. A., J. Persing, M. T. Montgomery, and S. A. Braun, 2007: A Lagrangian trajectory view on transport and mixing processes between the eye, eyewall, and environment using a high-resolution simulation of Hurricane Bonnie (1998). *J. Atmos. Sci.*, **64**, 1835–1856.
- Davis, C. A. and L. F. Bosart, 2003: Baroclinically induced tropical cyclogenesis. *Mon. Wea. Rev.*, **131**, 2730–2747.
- Davis, C. A. and L. F. Bosart, 2004: The TT problem: Forecasting the tropical transition of cyclones. *Bull. Amer. Meteor. Soc.*, **85**, 1657–1662.
- Dritschel, D. D., 1998: On the persistence of non-axisymmetric vortices in inviscid two-dimensional flows. *J. Fluid Mech.*, **371**, 141–155.
- Dritschel, D. D. and D. W. Waugh, 1992: Quantification of the inelastic interaction of unequal vortices in two-dimensional vortex dynamics. *Phys. Fluids*, **4**, 1737–1744.
- Eastin, M. D., P. G. Black, and W. M. Gray, 2002: Flight-level thermodynamic instrument wetting errors in hurricanes. Part I: Observations. *Mon. Wea. Rev.*, **130**, 825–841.
- Emanuel, K., 1986: An air-sea interaction theory for tropical cyclones. Part I: Steady-state maintenance. *J. Atmos. Sci.*, **43**, 585–604.
- Emanuel, K., 1988: The maximum intensity of hurricanes. *J. Atmos. Sci.*, **45**, 1143–1155.
- Emanuel, K., J. D. Neelin, and C. S. Bretherton, 1994: On large-scale circulations in convecting atmospheres. *Quart. J. Roy. Meteor. Soc.*, **120**, 1111–1143.
- Ford, R., 1994a: Gravity wave radiation from vortex trains in rotating shallow water. *J. Fluid Mech.*, **281**, 81–118.
- Ford, R., 1994b: The instability of an axisymmetric vortex with monotonic potential vorticity in rotating shallow water. *J. Fluid Mech.*, **280**, 303–334.
- Ford, R., M. E. McIntyre, and W. A. Norton, 2000: Balance on the slow quasimanifold: Some explicit results. *J. Atmos. Sci.*, **57**, 1236–1254.
- Fritsch, J. M., J. D. Murphy, and J. S. Kain, 1994: Warm core vortex amplification over land. *J. Atmos. Sci.*, **51**, 1780–1807.
- Fulton, S. R., 2007: PSWM: A periodic shallow water model. *Available from Colorado State University – Schubert Research Group*, 20pp.
- Fulton, S. R. and W. H. Schubert, 1987a: Chebyshev spectral methods for limited-area models. part i: Model problem analysis. *Mon. Wea. Rev.*, **115**, 1940–1953.
- Fulton, S. R. and W. H. Schubert, 1987b: Chebyshev spectral methods for limited-area models. part ii: Shallow water model. *Mon. Wea. Rev.*, **115**, 1954–1965.
- Gentry, R. C., T. T. Fujita, and R. C. Sheets, 1970: Aircraft, spacecraft, satellite and radar observations of hurricane Gladys, 1968. *J. Appl. Meteor.*, **9**, 837–850.

- Gray, W. M., 1968: Global view of the origin of tropical disturbances and storms. *Mon. Wea. Rev.*, **96**, 669–700.
- Guinn, T. A. and W. H. Schubert, 1993: Hurricane spiral bands. *J. Atmos. Sci.*, **50**, 3380–3403.
- Hausman, S. A., K. V. Ooyama, and W. H. Schubert, 2006: Potential vorticity structure of simulated hurricanes. *J. Atmos. Sci.*, **63**, 87–108.
- Haynes, P. H. and E. F. Shuckburgh, 2000a: Effective diffusivity as a diagnostic of atmospheric transport, 1. stratosphere. *J. Geophys. Res.*, **105**, 22 777–22 794.
- Haynes, P. H. and E. F. Shuckburgh, 2000b: Effective diffusivity as a diagnostic of atmospheric transport, 2. troposphere and lower stratosphere. *J. Geophys. Res.*, **105**, 22 795–22 810.
- Hendricks, E. A. and M. T. Montgomery, 2006: Rapid scan views of convectively generated mesovortices in sheared tropical cyclone Gustav (2002). *Wea. Forecasting*, **21**, 1041–1050.
- Hendricks, E. A., M. T. Montgomery, and C. A. Davis, 2004: The role of “vortical” hot towers in the formation of tropical cyclone Diana (1984). *J. Atmos. Sci.*, **61**, 1209–1232.
- Hendricks, E. A. and W. H. Schubert, 2008: Diagnosing transport and mixing in two-dimensional hurricane-like vortices using a tracer-based coordinate. *Quart. J. Roy. Meteor. Soc.*, Submitted.
- Hendricks, E. A., W. H. Schubert, and S. R. Fulton, 2009a: An idealized modeling study of stratified potential vorticity mixing in hurricanes. *Quart. J. Roy. Meteor. Soc.*, in preparation.
- Hendricks, E. A., W. H. Schubert, B. D. McNoldy, and S. R. Fulton, 2009b: Shallow water simulation of a spontaneously radiating hurricane-like vortex. *Quart. J. Roy. Meteor. Soc.*, in preparation.
- Hendricks, E. A., W. H. Schubert, R. K. Taft, H. Wang, and J. P. Kossin, 2008: Lifecycles of hurricane-like potential vorticity rings. *J. Atmos. Sci.*, Submitted.
- Hoskins, B. J. and F. Bretherton, 1972: Energy dispersion in a barotropic atmosphere. *J. Atmos. Sci.*, **29**, 11–37.
- Hoskins, B. J., M. E. McIntyre, and A. W. Robertson, 1985: On the use and significance of isentropic potential vorticity maps. *Quart. J. Roy. Meteor. Soc.*, **111**, 877–946.
- Houze, R. A., S. Chen, B. F. Smull, W.-C. Lee, and M. M. Bell, 2007: Hurricane Intensity and Eyewall Replacement. *Science*, **315**, 1235–1239.
- Hsu, Y.-J. and A. Arakawa, 1990: Numerical modeling with and isentropic vertical coordinate. *Mon. Wea. Rev.*, **118**, 1933–1959.
- Jukes, M. and M. E. McIntyre, 1992: A high resolution, one-layer model of breaking planetary waves in the stratosphere. *Nature*, **328**, 590–596.
- Kalnay, E., et al., 1996: The NCEP/NCAR 40-year reanalysis project. *Bull. Amer. Meteor. Soc.*, **77**, 437–471.

- Kistler, R., et al., 2001: The ncep-ncar 50-year reanalysis: Monthly means CD-rom and documentation. *Bull. Amer. Meteor. Soc.*, **82**, 247–267.
- Knaff, J. A., J. P. Kossin, and M. DeMaria, 2003: Annular hurricanes. *Wea. Forecasting*, **18**, 204–223.
- Knaff, J. A. and R. Zehr, 2007: Reexamination of tropical cyclone wind–pressure relationships. *Wea. Forecasting*, **22**, 71–88.
- Koh, T. Y. and R. A. Plumb, 2000: Lobe dynamics applied to barotropic rossby-wave breaking. *Phys. Fluids*, **12**, 1518–1528.
- Konor, C. and A. Arakawa, 1997: Design of an atmospheric model based on a generalized vertical coordinate. *Mon. Wea. Rev.*, **125**, 1649–1673.
- Kossin, J. P. and M. D. Eastin, 2001: Two distinct regimes in the kinematic and thermodynamic structure of the hurricane eye and eyewall. *J. Atmos. Sci.*, **58**, 1079–1090.
- Kossin, J. P., B. D. McNoldy, and W. H. Schubert, 2002: Vortical swirls in hurricane eye clouds. *Mon. Wea. Rev.*, **130**, 3144–3149.
- Kossin, J. P. and W. H. Schubert, 2001: Mesovortices, polygonal flow patterns, and rapid pressure falls in hurricane-like vortices. *J. Atmos. Sci.*, **58**, 2196–2209.
- Kossin, J. P. and W. H. Schubert, 2004: Mesovortices in Hurricane Isabel. *Bull. Amer. Meteor. Soc.*, **85**, 151–153.
- Kossin, J. P., W. H. Schubert, and M. T. Montgomery, 2000: Unstable interactions between a hurricane’s primary eyewall and a secondary ring of enhanced vorticity. *J. Atmos. Sci.*, **57**, 3893–3917.
- Kossin, J. P., W. H. Schubert, C. M. Rozoff, and P. J. Mulero, 2006: Internal dynamic control on hurricane intensity change: The dual nature of potential vorticity mixing. *27th Conference on Hurricanes and Tropical Meteorology*, Monterey, CA, Amer. Meteor. Soc.
- Kuo, H. C., L.-Y. Lin, C.-P. Chang, and R. T. Williams, 2004: The formation of concentric vorticity structures in typhoons. *J. Atmos. Sci.*, **61**, 2722–2734.
- Kuo, H. C., W. H. Schubert, C. L. Tsai, and Y. F. Kuo, 2008: Vortex interactions and barotropic aspects of concentric eyewall formation. *Mon. Wea. Rev.*, submitted.
- Kurihara, Y. M., 1979: On the development of spiral bands in tropical cyclones. *J. Atmos. Sci.*, **33**, 940–958.
- Kurihara, Y. M. and M. A. Bender, 1980: Use of a movable nested-mesh model for tracking a small vortex. *Mon. Wea. Rev.*, **108**, 1792–1809.
- Lapeyre, G., 2002: Characterization of finite-time Lyapunov exponents and vectors in two-dimensional turbulence. *Chaos*, **12**, 688–698.
- Leith, C. E., 1980: Nonlinear normal mode initialization and quasigeostrophic theory. *J. Atmos. Sci.*, **37**, 958–968.

- Lewis, B. M. and H. F. Hawkins, 1982: Polygonal eye walls and rainbands in hurricanes. *Bull. Amer. Meteor. Soc.*, **63**, 1294–1300.
- Lighthill, M. J., 1952: On sound generated aerodynamically. i. general theory. *Proc. R. Soc. London*, 564–587.
- Lorenz, E. N., 1960: Energy and numerical weather prediction. *Tellus*, **12**, 17–26.
- Lorenz, E. N., 1986: On the existence of the slow manifold. *J. Atmos. Sci.*, **43**, 1547–1557.
- Lorenz, E. N. and V. Krishnamurthy, 1987: On the nonexistence of the slow manifold. *J. Atmos. Sci.*, **44**, 2940–2949.
- Mallen, K. J., M. T. Montgomery, and B. Wang, 2005: Reexamining the near-core radial structure fo the tropical cyclone primary circulation: Implications for vortex resiliency. *J. Atmos. Sci.*, **62**, 408–425.
- Marks, F. D., Houze, Robert A., Jr., and J. F. Gamache, 1992: Dual-aircraft investigation of the inner core of Hurricane Norbert. Part I: Kinematic structure. *J. Atmos. Sci.*, **49**, 919–942.
- McIntyre, M., 1989: On the antarctic ozone hole. *J. Atmos. Terr. Phys.*, **51**, 29–43.
- McIntyre, M. and T. N. Palmer, 1983: Breaking planetary waves in the stratosphere. *Nature*, **305**, 593–600.
- McIntyre, M. and T. N. Palmer, 1984: The surf zone in the stratosphere. *J. Atmos. Terr. Phys.*, **46**, 825–849.
- McIntyre, M. and T. N. Palmer, 1985: A note on the general concept of wave breaking for rossby and gravity waves. *Pure Appl. Geophys.*, **123**, 964–975.
- Melander, M. V., J. C. McWilliams, and M. J. Zabusky, 1987: Axisymmetrization and vorticity gradient intensification of an isolated two-dimensional vortex. *J. Fluid Mech.*, **178**, 137–157.
- Melander, M. V., M. J. Zabusky, and J. C. McWilliams, 1988: Symmetric vortex merger in two dimensions: Causes and conditions. *J. Fluid Mech.*, **195**, 303–340.
- Michalke, A. and A. Timme, 1967: On the inviscid instability of certain two-dimensional vortex-type flow. *J. Fluid Mech.*, **29**, 647–666.
- Möller, J. D. and R. K. Smith, 1994: The development of potential vorticity in a hurricane-like vortex. *Quart. J. Roy. Meteor. Soc.*, **120**, 1255–1265.
- Montgomery, M. T., M. M. Bell, S. D. Aberson, and M. L. Black, 2006a: Hurricane Isabel (2003). New insights into the physics of intense storms. Part I: Mean vortex structure and maximum intensity estimates. *Bull. Amer. Meteor. Soc.*, **87**, 1335–1347.
- Montgomery, M. T. and J. Enagonio, 1998: Tropical cyclogenesis via convectively forced vortex Rossby waves in a three-dimensional quasigeostrophic model. *J. Atmos. Sci.*, **55**, 3176–3207.

- Montgomery, M. T. and B. F. Farrell, 1993: Tropical cyclone formation. *J. Atmos. Sci.*, **50**, 285–310.
- Montgomery, M. T. and R. J. Kallenbach, 1997: A theory for vortex Rossby waves and its application to spiral bands and intensity changes in hurricanes. *Quart. J. Roy. Meteor. Soc.*, **123**, 435–465.
- Montgomery, M. T., M. E. Nicholls, T. A. Cram, and A. B. Saunders, 2006b: A vortical hot tower route to tropical cyclogenesis. *J. Atmos. Sci.*, 355–386.
- Montgomery, M. T. and L. J. Shapiro, 1995: Generalized Charney-Stern and Fjortoft theorem for rapidly rotating vortices. *J. Atmos. Sci.*, **52**, 1829–1833.
- Montgomery, M. T., V. A. Vladimirov, and P. V. Denissenko, 2002: An experimental study on hurricane mesovortices. *J. Fluid Mech.*, **471**, 1–32.
- Nakamura, N., 1995: Modified lagrangian-mean diagnostics of the stratospheric polar vortices. Part I: Formulation and analysis of GFDL SKYHI GCM. *J. Atmos. Sci.*, **52**, 2096–2108.
- Nakamura, N., 1996: Two-dimensional mixing, edge formation, and permeability diagnosed in area coordinates. *J. Atmos. Sci.*, **53**, 1524–1537.
- Ngan, K. and T. G. Shepherd, 1999a: A closer look at chaotic advection in the stratosphere. part 1: Geometric structure. *J. Atmos. Sci.*, **56**, 4134–4152.
- Ngan, K. and T. G. Shepherd, 1999b: A closer look at chaotic advection in the stratosphere. part 2: Statistical diagnostics. *J. Atmos. Sci.*, **56**, 4153–4166.
- Nolan, D. S. and B. F. Farrell, 1999: The intensification of two-dimensional swirling flows by stochastic asymmetric forcing. *J. Atmos. Sci.*, **56**, 3937–3962.
- Nolan, D. S. and M. T. Montgomery, 2000: The algebraic growth of wavenumber one disturbances in hurricane-like vortices. *J. Atmos. Sci.*, **57**, 3514–3538.
- Nolan, D. S. and M. T. Montgomery, 2002: Nonhydrostatic, three-dimensional perturbations to balanced, hurricane-like vortices. Part I: Linearized formulation, stability, and evolution. *J. Atmos. Sci.*, **59**, 2989–3020.
- Nolan, D. S., M. T. Montgomery, and L. D. Grasso, 2001: The wavenumber-one instability and trochoidal motion of hurricane-like vortices. *J. Atmos. Sci.*, **58**, 3243–3270.
- Oda, M., M. Nakanishi, and G. Naito, 2006: Interaction of an asymmetric double vortex and trochoidal motion of a cyclone with the concentric eyewall structure. *J. Atmos. Sci.*, **63**, 1069–1081.
- O’Sullivan, D. and T. J. Dunkerton, 1995: Generation of inertia-gravity waves in a simulated life cycle of baroclinic instability. *J. Atmos. Sci.*, **52**, 3695–3716.
- Ottino, J. M., 1989: The kinematics of mixing: Stretching, chaos, and transport. *Cambridge University Press*, 364pp.
- Persing, J. and M. T. Montgomery, 2003: Hurricane superintensity. *J. Atmos. Sci.*, **60**, 2349–2371.

- Pielke, R. A., 2002: Mesoscale meteorological modeling – second edition. *Academic Press*, 676pp.
- Pielke, R. A., et al., 1992: A comprehensive meteorological modeling system – RAMS. *Meteorol. Atmos. Phys.*, **49**, 69–91.
- Pierrhumbert, R. T. and H. Yang, 1993: Global chaotic mixing on isentropic surfaces. *J. Atmos. Sci.*, **50**, 2462–2480.
- Polvani, L. M. and R. A. Plumb, 1992: Rossby wave breaking, microbreaking, filamentation, and secondary vortex formation. *J. Atmos. Sci.*, **49**, 462–476.
- Prieto, R., B. D. McNoldy, S. R. Fulton, and W. H. Schubert, 2003: A classification of binary tropical cyclone-like vortex interactions. *Mon. Wea. Rev.*, **131**, 2656–2666.
- Reasor, P. D., M. T. Montgomery, and L. F. Bosart, 2005: Mesoscale observations of the genesis of Hurricane Dolly (1996). *J. Atmos. Sci.*, **62**, 3151–3171.
- Reasor, P. D., M. T. Montgomery, F. D. Marks, and J. F. Gamache, 2000: Low-wavenumber structure and evolution of the hurricane inner core observed by airborne dual-doppler radar. *Mon. Wea. Rev.*, **128**, 1653–1680.
- Ritchie, E. and G. J. Holland, 1993: On the interaction of tropical cyclone scale vortices. ii: Interacting vortex patches. *Quart. J. Roy. Meteor. Soc.*, **119**, 1363–1379.
- Rotunno, R. and K. A. Emanuel, 1987: An air-sea interaction theory for tropical cyclones. Part II: Evolutionary study using a nonhydrostatic axisymmetric numerical model. *J. Atmos. Sci.*, **44**, 542–561.
- Rozoff, C. M., J. P. Kossin, W. H. Schubert, and P. J. Mulero, 2008: Internal control of hurricane intensity: The dual nature of potential vorticity mixing. *J. Atmos. Sci.*, submitted.
- Rozoff, C. M., W. H. Schubert, B. D. McNoldy, and J. P. Kossin, 2006: Rapid filamentation zones in intense tropical cyclones. *J. Atmos. Sci.*, **63**, 325–340.
- Saujani, S. and T. G. Shepherd, 2002: Comments on ‘Balance and the slow quasimanifold: Some explicit results’. *J. Atmos. Sci.*, **59**, 2874–2877.
- Schechter, D. A. and M. T. Montgomery, 2006: Conditions that inhibit the spontaneous radiation of spiral inertia-gravity waves from an intense mesoscale cyclone. *J. Atmos. Sci.*, **63**, 435–456.
- Schubert, W. H., J. J. Hack, P. L. Silva Dias, and S. R. Fulton, 1980: Geostrophic adjustment in an axisymmetric vortex. *J. Atmos. Sci.*, **37**, 1464–1484.
- Schubert, W. H., M. T. Montgomery, R. K. Taft, T. A. Guinn, S. R. Fulton, J. P. Kossin, and J. P. Edwards, 1999: Polygonal eyewalls, asymmetric eye contraction, and potential vorticity mixing in hurricanes. *J. Atmos. Sci.*, **56**, 1197–1223.
- Schubert, W. H., C. M. Rozoff, J. L. Vigh, B. D. McNoldy, and J. P. Kossin, 2007: On the distribution of subsidence in the hurricane eye. *Quart. J. Roy. Meteor. Soc.*, **133**, 595–605.

- Scott, R. K., E. F. Shuckburgh, J. P. Cammas, and B. Legras, 2003: Stretching rates and equivalent length near the tropopause. *J. Geophys. Res.*, **108**, 4384, doi:10.1029/2002JD002988.
- Shapiro, L. J. and M. T. Montgomery, 1993: A three-dimensional balance theory for rapidly rotating vortices. *J. Atmos. Sci.*, **50**, 3322–3335.
- Shapiro, L. J. and H. E. Willoughby, 1982: The response of balanced hurricanes to local sources of heat and momentum. *J. Atmos. Sci.*, **39**, 378–394.
- Sheets, R. C., 1990: The National Hurricane Center – past, present, and future. *Wea. Forecasting*, **5**, 185–232.
- Shuckburgh, E. and P. Haynes, 2003: Diagnosing transport and mixing using a tracer-based coordinate system. *Phys. Fluids*, **15**, 3342–3357.
- Simmons, A. J. and D. M. Burridge, 1981: An energy and angular momentum conserving vertical finite-difference scheme and hybrid vertical coordinates. *Mon. Wea. Rev.*, **109**, 758–766.
- Sippel, J. A., J. W. Nielsen-Gammon, and S. E. Allen, 2006: The multiple-vortex nature of tropical cyclogenesis. *Mon. Wea. Rev.*, **134**, 1796–1814.
- Skamarock, W. C., J. B. Klemp, J. Dudhia, D. O. Gall, D. M. Barker, W. Wang, and J. G. Powers, 2005: A description of the Advanced Research WRF Version 2. Tech. rep., NCAR Tech. Note NCAR/TN-468+STR, 20 pp., Boulder, CO. [Available online at http://www.mmm.ucar.edu/wrf/users/docs/arw_v2.pdf].
- Smith, R. A. and M. N. Rosenbluth, 1990: Algebraic instability of hollow electron columns and cylindrical vortices. *Phys. Rev. Lett.*, **64**, 649–652.
- Stossmeister, G. J. and G. M. Barnes, 1992: The development of a second circulation center within Tropical Storm Isabel (1985). *Mon. Wea. Rev.*, **120**, 685–697.
- Sundqvist, H., 1975: Initialization for models using sigma as the vertical coordinate. *J. Appl. Meteor.*, **14**, 152–158.
- Temperton, C., 1983a: Fast mixed-radix real fourier transforms. *J. Comput. Phys.*, **52**, 340–350.
- Temperton, C., 1983b: A note on prime factor FFT algorithms. *J. Comput. Phys.*, **52**, 198–204.
- Temperton, C., 1983c: Self-sorting mixed-radix fast fourier transforms. *J. Comput. Phys.*, **52**, 1–23.
- Terwey, W. D. and M. T. Montgomery, 2002: Wavenumber-2 and wavenumber- m vortex rossby wave instabilities in a generalized three-region model. *J. Atmos. Sci.*, **59**, 2421–2427.
- Terwey, W. D. and M. T. Montgomery, 2008: Secondary eyewall formation in two idealized, full-physics modeled hurricanes. *J. Geophys. Res.*, in press.

- Thomas, S. J. and G. L. Browning, 2001: The accuracy and efficiency of semi-implicit time stepping for mesoscale storm dynamics. *J. Atmos. Sci.*, **58**, 3053–3063.
- Viudez, A., 2006: Spiral patterns of inertia-gravity waves in geophysical flows. *J. Fluid Mech.*, **562**, 73–82.
- Viudez, A. and D. G. Dritschel, 2006: Spontaneous generation of inertia-gravity packets by balanced geophysical flows. *J. Fluid Mech.*, **553**, 107–117.
- Vladimirov, V. A. and V. F. Tarasov, 1980: Formation of a system of vortex filaments in a rotating liquid. *Izv. Akad. Nauk. SSSR Mekh. Zhidk. Gaza*, **1**, 44–51.
- Wang, H., 2002: Rearrangement of annular rings of high vorticity. WHOI Summer Program in Geophysical Fluid Dynamics.
- Wang, Y. and C.-C. Wu, 2004: Current understanding of tropical cyclone structure and intensity changes – a review. *Meteorol. Atmos. Phys.*, **87**, 257–278.
- Waugh, D. W. and et al., 1994: Transport of material out of the stratospheric arctic vortex by rossby wave breaking. *J. Geophys. Res.*, **99**, 1071–1088.
- Willoughby, H. E., 1998: Tropical cyclone eye thermodynamics. *Mon. Wea. Rev.*, **126**, 3053–3067.
- Willoughby, H. E., J. A. Clos, and M. G. Shoreibah, 1982: Concentric eye walls, secondary wind maxima, and the evolution of the hurricane vortex. *J. Atmos. Sci.*, **39**, 395–411.
- Winters, K. B. and E. A. D’Asaro, 1996: Discalar flux and the rate of fluid mixing. *J. Fluid Mech.*, **317**, 179–193.
- Yau, M. K., Y. Liu, D.-L. Zhang, and Y. Chen, 2004: A multiscale numerical study of Hurricane Andrew (1992). Part VI: Small-scale inner-core structures and wind streaks. *Mon. Wea. Rev.*, **132**, 1410–1433.
- Zhang, F., 2004: Generation of mesoscale gravity waves in upper-tropospheric jet-front systems. *J. Atmos. Sci.*, **61**, 440–457.
- Zhu, H., R. K. Smith, and W. Ulrich, 2001: A minimal three-dimensional tropical cyclone model. *J. Atmos. Sci.*, **58**, 1924–1944.
- Zipser, E. J., 2003: Some views on “hot towers” after 50 years of tropical field programs and two years of TRMM data. *Cloud Systems, Hurricanes, and the Tropical Rainfall Measuring Mission (TRMM) – A Tribute to Dr. Joanne Simpson*, Amer. Meteor. Soc., No. 51 in Meteor. Monogr., 48–58.
- Zipser, E. J. and C. Gautier, 1978: Mesoscale events within a gate tropical depression. *Mon. Wea. Rev.*, **106**, 789–805.